

Sapphire Fiber Based Sensing Technologies for High Temperature Applications

Jiajun Wang

Dissertation submitted to the Faculty of
the Virginia Polytechnic Institute and State University
in partial fulfillment of the requirements for the degree of

Doctor of Philosophy
in
Electrical and Computer Engineering

Anbo Wang (Committee chair)
Gary Pickrell (Committee member)
Louis Guido (Committee member)
T.-C. Poon (Committee member)
Yong Xu (Committee member)

January 19th, 2011
Blacksburg, Virginia

Keywords: Sapphire fiber, sensing, high temperature, harsh environment, multiplexed, miniaturized, thin film, wafer

Sapphire Fiber Based Sensing Technologies for High Temperature Applications

Jiajun Wang

Abstract

Sapphire fiber has been studied intensively for harsh environment sensing in the past two decades due to its supreme mechanical, physical and optical properties. It is by far the most reported and likely the best optical fiber based sensing technology for sensing applications in temperature beyond 1000 °C.

Several sensing schemes have been proposed and studied to date including sapphire fiber extrinsic and intrinsic Fabry-Perot interferometers, fiber Bragg gratings and long period gratings inscribed in sapphire fibers. Lacking the cladding, sapphire fiber is highly multimoded which renders sapphire fiber based sensor fabrication much more difficult than those based on silica fibers. Among all the reported work on sapphire fiber sensing, the vast majority is for single point temperature measurement.

In this work, different sensing schemes are proposed to enhance the capability of the sapphire fiber based sensing technology. For the single point sensing, a miniaturized sapphire fiber temperature sensor for embedded sensing applications was proposed and studied. The sensors are no more than 75 μm in diameter and are ideal for non-invasive embedded sensing applications. Unlike existing sapphire fiber sensors, the thin film sensors are batch-fabrication oriented and thus have a potential to permit mass production with low cost. In addition to single point sensors, multiplexed sapphire fiber sensing systems are investigated for the first time. Two multiplexed sensing solutions, named frequency-multiplexing and spatial-multiplexing, are proposed and studied to achieve multiplexed sensing based on sapphire fibers.

Acknowledgement

First of all, I would like to express my greatest gratitude to my advisor, Dr. Wang, for offering me such a great opportunity to work at Center for Photonics Technology with such an amazing team on so many exciting projects. I am also indebted to his consistent inspiration and comprehensive teaching across my entire PhD study. The education not only helped me throughout the PhD research but will also benefit my entire life. I also have to thank my other committee members, Dr. Pickrell, Dr. Guido, Dr. Poon and Dr. Xu, for their valuable suggestions and discussions for my research and dissertation.

Special thanks are due to Dr. Zhu and Dr. Han, who helped establishing my foundations for the PhD work. I have to thank Dr. Lally in particular, a good friend as well as a great project manager, for his generous help and guidance for my research and everyday life. Tremendous appreciation is also for Bo Dong, who helped me jump into the role of research and shared his thoughtful ideas with me for the past years that we have been working together. Big thank you also goes to my friends and co-workers, Dr. Gong, Brian Scott, Cheng Ma, Dorothy Wang, Kathy Wang, Tyler Shillig, Georgi Ivanov and Michael Fraser for the wonderful time that we spend together.

I have to thank my wife Xiao, for being such a great supporter throughout my PhD study. Great thanks are for my parents, Guiping Wang and Caiping Li, for their unreserved love and encouragement for my study and oversea life. I also have to convey my gratitude to my uncle, Dr. Xiaoping Wang, for his valuable discussions in the research and generous help in my life. Without the wonderful understandings and encouragements from all the people around, I would not have the chance to be what I am today.

Last but not least, great thanks are due to my project sponsors, the NETL of the U.S. Department of Energy and the Pratt & Whitney, for their financial support for the challenging but exciting sapphire sensing projects that I have been working on.

Table of Contents

Abstract	ii
Acknowledgement	iii
Table of Contents	iv
List of Figures and Tables	vi
Chapter 1 Introduction	1
1.1 Scope	1
1.2 Miniaturized temperature sensor	2
1.3 High temperature distributed sensing	4
1.4 Summary	5
Chapter 2 Thin film miniaturized temperature sensor	6
2.1 Sensing principle	7
2.2 Optical interrogation system	8
2.3 Coating method and material selection	15
2.3.1 Coating method	15
2.3.2 Material selection	17
2.4 Experiment results	19
2.4.1 Thick-Ta ₂ O ₅ film sensor	19
2.4.2 Thin-Ta ₂ O ₅ film sensor	28
2.4.3 TiO ₂ film sensor	33
2.4.4 ZrO ₂ film sensor	42
2.4.5 Summary of the thin film sensors.....	55
Chapter 3 Multiplexed sensing system by frequency-multiplexing	57
3.1 Sensing principle	58
3.2 Frequency-multiplexing sensing system	60
3.2.1 Optical interrogation system.....	60
3.2.2 Sensor fabrication	62
3.2.3 Measurement after fabrication.....	64
3.3 Calibration and analysis	66

3.3.1	Calibration.....	66
3.3.2	Sensitivity.....	68
3.3.3	Consistency.....	68
3.3.4	Temperature resolution.....	70
Chapter 4	Multiplexed sensing system by spatial-multiplexing.....	71
4.1	Sensing principle.....	72
4.2	Experiments for feasibility study.....	80
4.2.1	Single mode fiber with two sensors.....	81
4.2.2	Sapphire fiber with a single sensor.....	85
4.3	Multiplexed sapphire sensing system.....	91
4.3.1	Characterization and selection of the tunable light source.....	92
4.3.2	Optical detection and data acquisition system.....	98
4.3.3	Experimental results.....	100
Chapter 5	Conclusion and future work.....	106
	Bibliography.....	109

List of Figures and Tables

Figure 2-1: Configuration of a thin film temperature sensor	7
Figure 2-2: Optical inspection system for the thin film temperature sensors	8
Figure 2-3: Optical spectrum of the HL-2000 as measured by the OSA.....	9
Figure 2-4: Measured spectra without light source at different temperatures	11
Figure 2-5: Setup for thin film sensor testing and calibration	14
Figure 2-6: Picture of the PVD-250 for the thin film coating.....	16
Figure 2-7: Metal holder for film deposition on the fiber and wafer samples.....	17
Figure 2-8: Accumulated thermal expansion for some high temperature materials.....	18
Figure 2-9: Fiber and wafer samples ready for the thick-Ta ₂ O ₅ film deposition.....	20
Figure 2-10: Reflection spectrum of the thick-Ta ₂ O ₅ film on a sapphire wafer	21
Figure 2-11: Microscopic image of the thick-Ta ₂ O ₅ film on a sapphire wafer	21
Figure 2-12: Color of the thick-Ta ₂ O ₅ thin film	22
Figure 2-13: XPS result of the thick-Ta ₂ O ₅ film wafer samples	23
Figure 2-14: OPD changes after the first annealing at 400 °C.....	24
Figure 2-15: Spectra of the thick-Ta ₂ O ₅ film sensor at different temperatures	25
Figure 2-16: Calibration curve of the thick-Ta ₂ O ₅ thin film sensor	26
Figure 2-17: Fluctuation of wavelength shifts for the thick-Ta ₂ O ₅ film sensor	27
Figure 2-18: Microscopic image of the sapphire fiber with the thin-Ta ₂ O ₅ film.....	29
Figure 2-19: Spectrum of the thin-Ta ₂ O ₅ film sensor after deposition.....	30
Figure 2-20: Spectra of the thin-Ta ₂ O ₅ sensor measured at different temperatures	31
Figure 2-21: Calibration curve of the thin-Ta ₂ O ₅ film sensor	31
Figure 2-22: Fluctuation of resolved peak wavelengths at 1100 °C	32
Figure 2-23: Samples for the TiO ₂ thin film deposition	33
Figure 2-24: TiO ₂ film deposited on a sapphire wafer	34
Figure 2-25: TiO ₂ film deposited on the tip of a sapphire fiber.....	35
Figure 2-26: Spectrum of the TiO ₂ film sensor after deposition	35
Figure 2-27: Microscopic images of the TiO ₂ film annealed at different temperatures ...	36
Figure 2-28: XPS result of the TiO ₂ film after deposition.....	37

Figure 2-29: Fringes of the TiO ₂ film sensor at 1200 °C	38
Figure 2-30: Blackbody radiation vs. fringes from the TiO ₂ film sensor at 1200 °C	39
Figure 2-31: Reflection spectra shift as temperature changes	39
Figure 2-32: Calibration curve of the TiO ₂ film sensor	40
Figure 2-33: Resolution of the TiO ₂ film sensor	41
Figure 2-34: Long-term stability test of the TiO ₂ film sensor	42
Figure 2-35: Samples ready for the ZrO ₂ film deposition	43
Figure 2-36: Microscopic image of a sapphire fiber with the ZrO ₂ film coated.....	44
Figure 2-37: Spectrum of the ZrO ₂ film sensor measured after deposition.....	44
Figure 2-38: Microscopic images of the ZrO ₂ film annealed at different temperatures ...	45
Figure 2-39: Pictures of the ZrO ₂ film on the sapphire wafer sample after annealing	45
Figure 2-40: Fringes of the ZrO ₂ wafer sample after 1500 °C annealing	46
Figure 2-41: XRD result for the ZrO ₂ thin film on sapphire wafer samples.....	47
Figure 2-42: Surface contour of the as-deposition ZrO ₂ thin film sample	48
Figure 2-43: 3D map of the as-deposition ZrO ₂ thin film sample	48
Figure 2-44: Surface contour of the annealed ZrO ₂ thin film sample.....	49
Figure 2-45: 3D map of the annealed ZrO ₂ thin film sample	50
Figure 2-46: Averaged spectrum at each calibration temperature	51
Figure 2-47: The transmission spectrum induced background	52
Figure 2-48: Transmission spectrum compensated sensor spectra	52
Figure 2-49: Central peak wavelength vs. temperature for the ZrO ₂ thin film sensor.....	53
Figure 2-50: Calibration curve for the ZrO ₂ thin film sensor	54
Figure 2-51: Fluctuation of the central peak wavelengths measured at 1000 °C.....	55
Figure 3-1: Configuration of a single point air-gap based sapphire temperature sensor ..	58
Figure 3-2: Reflection spectra of air-gap sensors with different OPDs.....	59
Figure 3-3: Optical interrogation system for the multiplexed sensing system	61
Figure 3-4: Metal frame for temporary sensor bonding.....	62
Figure 3-5: GUI of the computer program to aid sensor fabrication	63
Figure 3-6: CO ₂ laser for permanent sensor bonding	64
Figure 3-7: Picture of the three-sensor sapphire fiber sensing link	64
Figure 3-8: Reflection spectra of the three-sensor link.....	65

Figure 3-9: FFT result of the reflection spectra of the three-sensor link	65
Figure 3-10: Calibration curves for the air-gap sensors.....	68
Figure 3-11: Normalized calibration curves for all the sensors	69
Figure 3-12: Fluctuation of the OPD output of sensor 2 at different temperatures	70
Figure 4-1: Diagram of the OFDR sensing system.....	72
Figure 4-2: Photodetector readings during a wavelength scan	76
Figure 4-3: FFT result of the photodetector data	77
Figure 4-4: FFT result shown in spatial domain.....	78
Figure 4-5: Recovered spectrum for one of the sensors	79
Figure 4-6: Recovered spectra for all three sensors.....	80
Figure 4-7: System schema for the two-sensor SMF experiment.....	81
Figure 4-8: A reflection spectrum measured by the CTS	82
Figure 4-9: FFT of the reflection spectrum measured by the CTS.....	83
Figure 4-10: Recovered spectrum for sensor 1	83
Figure 4-11: Recovered spectrum for sensor 2	84
Figure 4-12: System diagram for the OFDR one sapphire sensor experiment	85
Figure 4-13: Waveform detected by the photodetector	86
Figure 4-14: FFT of the photodetector data.....	87
Figure 4-15: Recovered spectrum compared to the original data.....	88
Figure 4-16: 100 consecutive recovered spectra in 5 minutes.....	89
Figure 4-17: Central wavelength position changes during spectra recovery.....	90
Figure 4-18: Recovered spectra shift as temperature varies	90
Figure 4-19: Non-linear wavelength tuning curve.....	92
Figure 4-20: FFT of the photodetector data with a non-linear wavelength tuning.....	93
Figure 4-21: Recovered spectrum with non-linear wavelength tuning.....	94
Figure 4-22: HCN gas cell for calibration of the wavelength tuning	94
Figure 4-23: Calibration of wavelength tuning for CTS.....	95
Figure 4-24: Calibration of wavelength tuning for Velocity 6300	95
Figure 4-25: Calibration of wavelength tuning for TUNICS-BT	96
Figure 4-26: Intensity fluctuation of tunable lasers during wavelength tuning.....	96
Figure 4-27: Intensity fluctuation of the CTS during a wavelength tuning.....	97

Figure 4-28: Picture of the New Focus 2117 balanced detector	99
Figure 4-29: Variable optical attenuator for balanced detection	99
Figure 4-30: System diagram of the modified OFDR system	100
Figure 4-31: Structure of the sapphire wafer in-line sensor	101
Figure 4-32: Picture of the sapphire wafer in-line sensor	101
Figure 4-33: Structure of the sapphire wafer end-sensor	101
Figure 4-34: Spectra of the three sapphire wafer sensors by the white light system	102
Figure 4-35: Picture of the fiber link with three identical wafer sensors	102
Figure 4-36: Photodetector data from the new OFDR system	103
Figure 4-37: FFT result of the photodetector data	104
Figure 4-38: Recovered spectra at different temperatures	104
Table 2-1: Comparison of different spectrometers	10
Table 2-2: List of properties of potential thin film materials	18
Table 2-3: Parameters used in the thick-Ta ₂ O ₅ film deposition	20
Table 2-4: Atomic concentration for the thick-Ta ₂ O ₅ film on a sapphire wafer	22
Table 2-5: Parameters used in the thin-Ta ₂ O ₅ film deposition	29
Table 2-6: Parameters used for the TiO ₂ film deposition	34
Table 2-7: Atomic concentration of the TiO ₂ film on a sapphire wafer	37
Table 2-8: Parameters used for the ZrO ₂ film deposition	43
Table 4-1: Comparison of different tunable light sources	97
Table 4-2: Key parameters for the Model 2117 balanced detector	99

Chapter 1 Introduction

Recently optical fiber sensors have been studied intensively for a variety of applications. Numerous designs have been proposed to measure a series of parameters, such as temperature [1-14], strain [10, 15-25], pressure [26-44], gases [45-51], electromagnetic fields [52, 53], and chemicals [54-56]. Due to advantages such as high sensitivity and resolution, distributed sensing capability and immunity to electromagnetic interference, optical fiber sensors are preferred over traditional sensing technologies in critical sensing applications. Also due to the aforementioned advantages, optical fiber sensors are well suitable for harsh environmental sensing which involves extreme physical conditions such as high temperature, high pressure, corrosion, toxicity, and presence of strong electromagnetic interference. These harsh environments often make electronic sensors difficult to apply.

1.1 Scope

Since commercial telecommunication grade optical fibers are mainly made of silica, the majority of reported optical fiber sensors are based on silica fibers, either single-mode or multi-mode fiber. Silica fiber sensors may work from ambient temperature up to 1000 °C but can not function beyond 1000 °C stably because of the thermal diffusion of the germanium dopant [57]. For sensing in environment beyond 1000 °C, alternative materials other than silica have to be used to avoid this problem. Wang *et al* proposed sapphire fiber based sensors in the 1990s [57-59]. Tong *et al* demonstrated the operation of a temperature sensor up to 2300 °C using a zirconia single-crystal fiber [4]. Kennedy *et al* used a Yb-doped single crystal YAG fiber to operate at a maximal temperature of 1600 °C [60]. Among these non-silica materials for high temperature measurement, single-crystal sapphire fiber-based optical sensors have received a great deal of attention in the past decade for the sensing applications in harsh environments. Due to sapphire's superior properties such as high melting point (>2000 °C), resistance to chemical corrosion, high hardness, and a wide spectral range of light

transmittance [61], these sensors can potentially perform without significant degradation at temperatures up to 2000 °C. Various sensor schemes, including wafer- [62] and air gap-based [63] Fabry-Perot Interferometers (FPIs), and sapphire fiber Bragg gratings [6], have been demonstrated.

Since sapphire fiber is highly multi-moded [61], sensor fabrications are much more difficult than those by silica single mode fiber. By far, the research in sapphire fiber sensing is mainly reported on single-point temperature measurement but is rarely reported for other applications. Sensors for distributed temperature sensing have not been reported. Report on successful development of sapphire fiber sensors for other parameters such as strain and pressure has been rather limited. This work is to focus on expanding the capability of sapphire sensing technology, and exploring additional sapphire fiber based sensors for more sensing applications.

1.2 Miniaturized temperature sensor

Sapphire fiber temperature sensing has attracted a great deal of attention because of its great potential in applications in coal gasifiers [64], and jet engines where traditional sensors can not fully serve the purpose. Several sapphire fiber based sensing methods have been demonstrated. Wang *et al* studied the sapphire fiber intrinsic Fabry-Perot sensor by splicing a sapphire fiber to the end of a silica single mode fiber [57]. Wang *et al* applied sapphire fiber polarimetric sensor for temperature measurement up to 1500 °C [59]. Saggese *et al* used a hollow sapphire waveguide for remote radiometric temperature sensing up to 1650 °C [2]. Xiao *et al* studied sapphire air gap sensors for both temperature and strain measurement [63]. Zhu *et al* used a sapphire wafer as the sensing element to go with a sapphire fiber for high temperature measurement [62, 65]. This wafer sensor has good fringe visibility but requires a mechanical bonding of the sapphire fiber and the sapphire wafer, which presents a great challenge to sensor miniaturization. Grobnic *et al* proposed a sapphire fiber temperature sensor with a Bragg grating inscribed in fiber by femto-second laser [6]. Due to the multi-moded nature of the sapphire fiber, performance of the Bragg grating highly relies on the mode-excitation

condition that is not easy to control in real applications. On the other hand, miniaturized sensors for harsh environment sensing are highly desired, especially for non-invasive sensing in a limited space such as in jet engines.

Signal demodulation and detection scheme also saw significant development as the sapphire sensor fabrication evolved. In the early days, lasers were used to interrogate the sapphire sensor and photodetectors were used to monitor the intensity change, which is induced by temperature change around the sapphire sensing elements [58]. The intensity changes periodically according to the temperature variation thus only the temperature change can be deduced. In order to get absolute temperature readings, the system must be calibrated prior to each use and then a continuous tracking in the temperature change must be performed to keep the absolute temperature reading correct. However, if the system suffers power failure, the absolute temperature reading is no longer valid after re-gaining power. Thus the intensity-based measurement is often categorized as a relative measurement. To solve this problem, white-light interferometry was proposed as an absolute measurement method. It typically applies a broad-band light source to interrogate a sensor and a spectrometer to obtain the reflection spectrum. This method is using a band of wavelengths, rather than a single wavelength, to inspect the sensor and an absolute reading can be generated per spectrum. Different wavelengths can generate destructive or constructive interference and the intensity measured on the spectrometer presents a periodic pattern whose frequency is generally temperature dependent. To accurately calculate the frequency is the key to achieve high sensor performance. Some algorithms [66, 67] have been studied for different sensor configurations.

In this dissertation, a new sensing scheme by thin film coating on the sapphire fiber tip is studied to form an intrinsic FPI. Optically speaking, the two reflection surfaces of the thin film are perfectly parallel to each other; that leads to a very high fringe contrast. This type of sensor also has advantages such as miniaturization, batch processing capability and potential low cost. The thin film is directly coated on the tip of a sapphire fiber; the size of the entire sensor is essentially that of the sapphire fiber,

which is no more than 75 μm based on present commercial availability. Also due to advantages of the thin film coating, it is possible to fabricate multiple sensors identically in a deposition run. Batch fabrication would eventually lead to a very low fabrication cost per sensor and have great potential for industrial mass production.

1.3 High temperature distributed sensing

Although sapphire fiber sensors have been studied for about two decades, sapphire fiber based distributed temperature sensing has not been reported so far. In some applications more than a single point of sensing is highly desired. For example, in jet engines, temperature distribution over a limited spatial span is important for engine characterization and optimization.

In this dissertation, methods to achieve more than a single point of sensing in high temperature environments are being studied. Based on the multiplexing principle, the methods are named as frequency-multiplexing and spatial-multiplexing. In the frequency-multiplexing system, three air-gap based sapphire fiber sensors with different cavity lengths are cascaded in a single fiber link for high temperature sensing. Each sensor is made by two pieces of sapphire fibers and a zirconia tube holding the fibers inside with a tight tolerance. Reflections from the ends of the two sapphire fibers interfere and generate fringes on the spectrometer when a broadband light source is used to illuminate the sensor. The three sensors are multiplexed in a single sensing link and de-multiplexed with different Optical Path Difference (OPD) values. Since each sensor has a fringe of a certain frequency on the spectrometer, this method is named as *frequency-multiplexing*. The second multiplexing/demultiplexing system allows each sensor having identical OPD values. This multiplexing method applies Optical Frequency Domain Reflectometry (OFDR) into the sapphire fiber sensing to interrogate the sapphire sensing link for both spatial-domain and frequency-domain responses. By recovering the frequency-domain response of each sensor through signal processing techniques, temperature change is sensed. In this method, each sensor may have identical OPD as long as they are positioned differently in relative to a reference point. Since this method uses the

information of the sensor location to demultiplex them, *spatial-multiplexing* is assigned to name it. For both methods, feasibility is demonstrated through temperature sensing. However, the methods can also be applied to sense other parameters.

1.4 Summary

As a summary, this work is to study sapphire fiber based sensing technologies for high temperature harsh environment applications. Ultra-miniaturized thin film temperature sensors and multiplexed sensing schemes are to be discussed in the following chapters. In Chapter 2, a thin film based ultra-miniaturized sapphire temperature sensor is proposed. Different materials are studied for the thin film coating and temperature sensing has been demonstrated experimentally up to 1200 °C, with a potential to go up to 1500 °C. In Chapter 3, high temperature multiplexed sensing using the frequency-multiplexing method is discussed. Three sapphire fiber sensors with different OPD values are built in a single sensing link and then calibrated up to 1000 °C. In Chapter 4, the spatial-multiplexing is studied for multiplexed high temperature sensing in which sensors are identical in OPD. Three sapphire wafer sensors with almost identical OPD values are built into a single sapphire sensing link. The third sensor is interrogated by the OFDR method and spectra shift by temperature change is detected.

Chapter 2 Thin film miniaturized temperature sensor

In the past decades, several types of optical high temperature sensors have been proposed. Fabry-Perot [62, 63, 65] is a very typical sensor structure and it has a sensor cavity as well as a mechanical body, such as a zirconia tube, to assemble the sensor. With the presence of the mechanical body, the sensor unit is typically bulky. Bragg grating inscribed in the sapphire fiber is also studied and reported [6]. Although this type of sensor can be small in size but requires careful mode excitation into the highly multi-moded sapphire fiber [68]; it is quite difficult to be used in real applications. The demand for miniaturized sensors is seen from industrial applications, especially for embedded sensing purposes. For example, the sensors for jet engines have to be embedded into a coupon material and overall size is limited to sub-millimeter.

A thin film based sapphire miniaturized sensor is proposed to solve the challenges for high temperature sensing where overall sensor size is a good concern. A thin film is deposited on the tip of a sapphire fiber and it generates an intrinsic Fabry-Perot cavity for temperature measurement. This kind of sensor is no bigger in size than the sapphire fiber itself. Currently, the commercially available sapphire fiber has a nominal diameter of 75 μm . The thin film sapphire fiber sensor is expected to be of the same size. Also fabrication of such a sensor is batch processing oriented and has good potential to be commercially applied with low cost per sensor fabrication. Furthermore, sensors coming out of one deposition run shall possess identical performance, a feature that is desired for mass production.

2.1 Sensing principle

Configuration of a thin film based sensor is shown in Figure 2-1. The thin-film, whose thickness is typically in the order of ~500 nm, is coated on the tip of a polished sapphire fiber to form an intrinsic Fabry-Perot cavity.

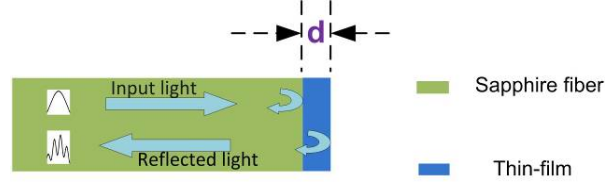


Figure 2-1: Configuration of a thin film temperature sensor

As surrounding temperature changes, the OPD of the thin film cavity would change accordingly as described by Equation 2-1.

$$\frac{OPD(T)}{OPD(T_0)} = \frac{2n(T)d(T)}{2n(T_0)d(T_0)} \approx 1 + (\alpha_n + \alpha_d)(T - T_0) \quad \text{Equation 2-1}$$

where α_n and α_d are the 1st-order thermal coefficients for the refractive index and the physical thickness, respectively. As temperature increases, the OPD of the thin film goes up accordingly. An optical interrogation system and a signal processing algorithm, which are to be discussed in later sections, are implemented to measure the reflection spectrum and to resolve the change in the sensor's OPD. From the results the temperature around the thin film is sensed. As can be found from Equation 2-1, the sensitivity of the film sensor is decided by the material property of the thin film and is independent of the sensor's initial OPD.

If a broad-band light source is used to interrogate the thin film sensor, the reflected spectrum has interferometric fringes whose frequency is decided by the OPD of the thin film sensor, as is seen from Equation 2-2,

$$I_r(\lambda) = I_1(\lambda) + I_2(\lambda) + \sqrt{I_1(\lambda)I_2(\lambda)} \cos\left(\frac{2\pi OPD(T)}{\lambda} + \varphi_0\right) \quad \text{Equation 2-2}$$

Where I_1 and I_2 are reflected light from both ends of the thin film.

2.2 Optical interrogation system

Since the film thickness is typically in the order of hundreds of nano-meters, a broad-band optical white-light is used to interrogate the thin film, as is seen from the optical system diagram in Figure 2-2.

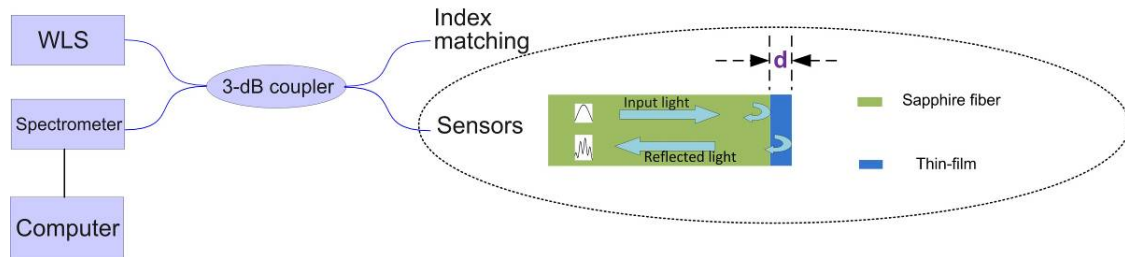


Figure 2-2: Optical inspection system for the thin film temperature sensors

The light from a white light source (WLS) is used to illuminate the sensor through a 3-dB fiber coupler. The reflected lights from both ends of the thin film interfere and generate fringes on the spectrometer, which is connected on the other arm of the 3-dB coupler. The frequency of the interferometric fringes is solely determined by the OPD of the thin film sensor. Once the reflection spectrum is measured and sampled into the computer, certain data processing algorithm can be used to detect the OPD (or OPD change) of the thin film and thus temperature sensing is implemented. Other than in the hot zone, silica fiber is used to transmit light from the sapphire fiber to the silica fiber to minimize the system cost. Sapphire to silica fusion splicing is performed on the non-film end of sapphire fiber, using the method discussed in Ref. [65].

The white light source (WLS) used in experiment is a Halogen-Tungsten bulb (HL-2000, Ocean Optics). The spectrum from the HL-2000, as measured by an optical spectrum analyzer (OSA) (Ando AQ6315E), can be found in Figure 2-3. Such a light source has a broad bandwidth coverage that is highly desired for the thin film interrogation, but the low intensity coupled into optical fiber is a considerable disadvantage because the intensity of the blackbody radiation at higher temperature can be as strong as, or even stronger than the reflection from sensors. The undesired blackbody radiation may overwhelm the reflection from the sensor and reduce the accuracy of the thin film sensor

greatly. To accommodate this problem, detectors have to have a high dynamic range and additional calibration measure has to be performed to remove the blackbody radiation background.

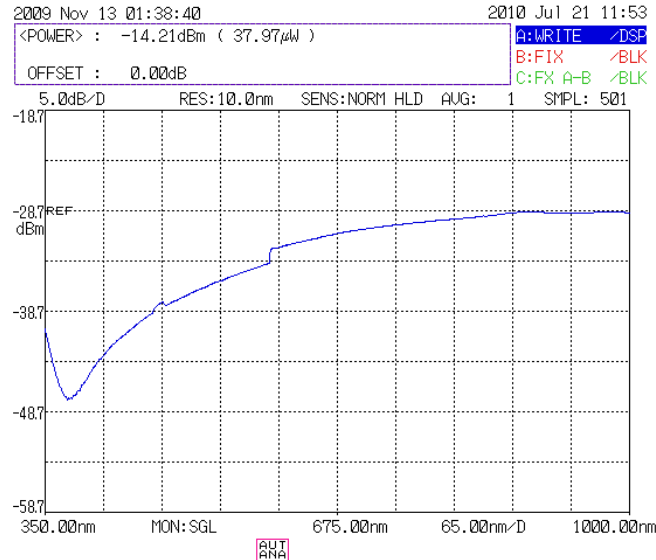


Figure 2-3: Optical spectrum of the HL-2000 as measured by the OSA

Three kinds of spectrometers (Ocean Optics, USB2000 and USB4000) with different operating wavelength ranges were used for the thin film sensor interrogations. Type I (USB2000) spectrometer has a detector array of 2048 pixels covering a wavelength range from 720 nm to 980 nm, yielding an averaged wavelength separation per pixel of 0.127 nm; Type II (USB2000) spectrometer has the same number of pixels in detector array but covers a wider wavelength range from 320 nm to 1000 nm with an averaged wavelength separation per pixel of 0.332 nm; Type III (USB4000) spectrometer covers a wavelength range from 347 nm to 1040 nm by 3648 pixels. That offers an averaged wavelength separation of 0.190 nm. Type III spectrometer also has a higher dynamic range than the Type I and the Type II spectrometers. The Type I spectrometer was initially used for thicker thin film sensor interrogations. The Type II and the Type III spectrometer have lower wavelength resolution but allow interrogation for sensors with smaller film thickness, and were used for sensors with thinner film later on. Table 2-1 summarizes the key parameters for the spectrometers.

Table 2-1: Comparison of different spectrometers

	Type I	Type II	Type III
Wavelength Range (nm)	720-980	320-1000	347-1040
Number of pixels	2048	2048	3648
Averaged Wavelength Separation (nm)	0.127	0.332	0.190
Dynamic Range	4096	4096	65536

The light source has a spectrum profile denoted as $I_{WLS}(\lambda)$ while the integration time set in the spectrometer is indicated by N . The measured spectrum $I(\lambda)$ for a given sensor can be expressed as Equation 2-3.

$$I(\lambda) = I_{Dark}(N, \lambda) + I_{BBR}(T, \lambda, N) + S \cdot N \cdot \{ I_{WLS}(\lambda) [R_{BR} + \beta(\lambda) [R_{TF,AC} \cos(\frac{2\pi OPD(T)}{\lambda} + \varphi_0) + R_{TF,DC}]] \}$$

Equation 2-3

$I_{Dark}(N, \lambda)$ is the measured dark spectrum when no light is launched into the spectrometer. It is mostly induced by the dark current in the CCD array inside the spectrometer. The dark spectrum is also integration time dependent. $I_{BBR}(T, \lambda, N)$ is the spectrum induced by the blackbody radiation which depends on temperature, wavelength as well as the integration time set in the spectrometer. Blackbody radiation induced spectrum is an important part in the total spectrum at high temperatures because the HL-2000 has a low power density. As shown in Figure 2-4, the spectrometer-received blackbody radiation through the thin film on the tip of the sapphire fiber increases dramatically when temperature goes higher. Thus, given a fixed dynamical range from the spectrometer, the blackbody radiation invites additional challenges for the thin film sensor interrogation at temperature beyond 1000 °C.

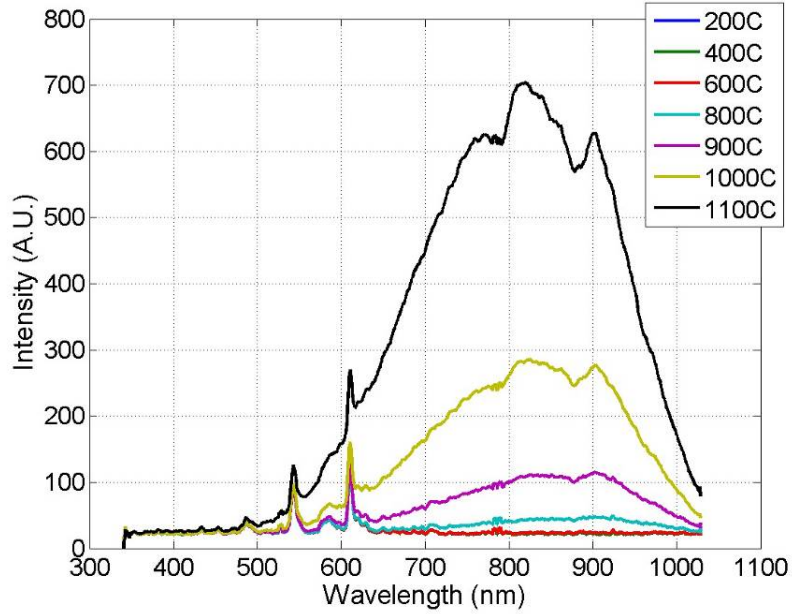


Figure 2-4: Measured spectra without light source at different temperatures

Provided with the blackbody radiation noise, extra attention has to be paid for sensing at temperatures more than 1000 °C to obtain an accurate interpretation of the thin film spectra. The Type I and Type II spectrometers have a dynamic range of 4096 only; we have to use the shorter wavelength region in order to avoid saturation caused by the blackbody radiation at high temperatures.

Three components that are proportional to the spectrum of the light source are the reflections from the thin film (both $R_{TF,AC}$ and $R_{TF,DC}$), and the optical background reflection R_{BR} from the fiber link other than the thin film such as the silica-sapphire splicing point. S in Equation 2-3 is the responsivity of the spectrometer, which is assumed to be a constant. When a fiber link is properly spliced, optical background reflection R_{BR} is much smaller than those from the thin film ($R_{TF,AC}$ and $R_{TF,DC}$). Thus R_{BR} is neglected for simplicity without introducing much error to the temperature measurement. $\beta(\lambda)$ is the transmission spectrum of the white light in the sapphire fiber based optical system. There are mainly two factors that determine the $\beta(\lambda)$. The first one is the modal transmission loss in the sapphire fiber. Since the light from the broad-band halogen light source is carried by many modes, higher modes have greater loss than the fundamental modes.

Shorter wavelength typically has larger modal volume than longer wavelength does [69], thus the modal loss in the sapphire fiber is wavelength dependent even if the sapphire fiber has a flat transmission window. The second factor is the optical absorption by the thin film. Some of the thin film materials we will discuss may have highly wavelength dependent absorption. Examples of this problem will be provided later and a method will be proposed to compensate this wavelength dependent transmission spectrum $\beta(\lambda)$.

To find out $OPD(T)$ of the thin film sensor, one can take two measurements under the same integration time N . The first measurement is carried out when the light source is on whose measured spectrum is shown in Equation 2-3 while the second one has the light source off. The second measured spectrum is expressed in Equation 2-4.

$$\tilde{I}(\lambda) = I_{Dark}(N, \lambda) + I_{BBR}(T, \lambda, N) \quad \text{Equation 2-4}$$

The difference between Equation 2-3 and Equation 2-4, as is expressed by Equation 2-5, has the $OPD(T)$ that we are interested in.

$$I(\lambda) - \tilde{I}(\lambda) \approx S \cdot N \cdot I_{WLS}(\lambda) \beta(\lambda) [R_{TF,AC} \cos(\frac{2\pi OPD(T)}{\lambda} + \varphi_0) + R_{TF,DC}] \quad \text{Equation 2-5}$$

Given the profile of the white light source $I_{WLS}(\lambda)$ is pre-measured and the transmission spectrum $\beta(\lambda)$ is learned by curve fitting, Equation 2-5 can be normalized to a sinusoidal curve. The peak position λ_m of the m^{th} peak is determined by Equation 2-6.

$$\lambda_m(T) = \frac{2n(T)d(T)}{m - \frac{\varphi_0}{2\pi}}, \quad OPD \equiv 2nd \quad \text{Equation 2-6}$$

When temperature changes on the thin film, λ_m shall shift accordingly, as is decided by Equation 2-7.

$$\begin{aligned}
\frac{\Delta\lambda}{\lambda} &\equiv \frac{\lambda_m(T') - \lambda_m(T)}{\lambda_m(T)} = \frac{2n(T')d(T') - 2n(T)d(T)}{2n(T)d(T)} \\
&\approx (1 + \alpha_d\Delta T)(1 + \alpha_n\Delta T) - 1 \\
&= (\alpha_d + \alpha_n)\Delta T + \alpha_d\alpha_n\Delta T^2
\end{aligned}
\tag{Equation 2-7}$$

The signal demodulation method to track the spectrum change of the thin film sensor is called *peak-tracking* method. Once a spectrum is measured, a parabolic curve fitting is carried out near a peak or a valley to determine the central wavelength of the peak or the valley. Continuously doing the peak-tracking, one can calculate the wavelength shift $\Delta\lambda$ from the initial value. The *relative wavelength shift* ($\Delta\lambda/\lambda$) is then used to represent the sensor. Once a sensor is calibrated, by measuring spectrum and calculating the relative wavelength shift, the temperature can be further deducted. Furthermore, since the relative wavelength shift ($\Delta\lambda/\lambda$) is not dependent on the wavelength of the peak, if multiple peaks and valleys are available, the above process can be simply repeated for all peaks and valleys and then an averaged result is used to obtain a more accurate calibration curve.

The above calibration method was gradually finalized as we were learning from the calibration data. During the early stage of this work, some other calibration methods were used. Details of the calibration method will be explained in later sections when each individual sensor is discussed.

Figure 2-5 shows a picture of the entire system used for sensor testing and calibration.



Figure 2-5: Setup for thin film sensor testing and calibration

A sapphire tube (I.D. 2.5 cm) provides a package for the sapphire thin film sensors. The sapphire tube enables convection thus the temperature is higher out of the furnace than the case without the sapphire tube, as can be seen by the bright region around the orifice of the furnace. The convection raises the temperature on the external fiber and raises the temperature around the silica-sapphire splicing point. For stable operation, the length of the sapphire fiber needs to be long enough in order that the temperature around the splicing point is below the rated operating temperature of the silica fiber, otherwise the performance of the thin film sensor can not be detected correctly. The other side of the trade-off is that the low power density light from the halogen light source does not propagate long in the sapphire fiber, due mainly to the modal loss aforementioned. In our experiments, the length of the sapphire fiber is approximately 15 cm unless otherwise specified.

2.3 Coating method and material selection

2.3.1 Coating method

Thin film optical coatings can be achieved by a number of deposition methods, such as chemical vapor deposition (CVD), plasma-enhanced chemical vapor deposition (PECVD), physical vapor deposition (PVD), sputtering, and atomic layer deposition (ALD). Each method has its own advantages for certain applications and/or readiness for certain materials. Among these methods, PVD was chosen for the rest of present study mainly because of the following reasons:

- Capability of depositing many high temperature materials
- Relative low cost on the source materials
- Availability in the Clean Room at Virginia Tech

In the beginning of this research, there was no particular material that we knew will work well. The idea was to test the performance of multiple materials and to find the one that works to the highest temperature. PVD was selected as the coating technique based on such consideration, since we can deposit many high temperature materials with relatively low cost.

The Clean Room at Virginia Tech has a PVD-250 from K. J. Lesker, a state of the art tool for PVD-based film coating. Figure 2-6 gives a picture of the PVD-250. The vacuum chamber of the PVD-250 has a D-shape and is 30'' in height and 24'' in depth. Since sapphire fibers are relatively stiff and fragile, excessive bending or coiling can easily break them. The spacious chamber in the PVD-250 avoids this problem and makes the deposition easy and convenient.



Figure 2-6: Picture of the PVD-250 for the thin film coating

Samples are mounted on a metal platen at the top of the chamber, while the thin film source material and its crucible liner are located at the bottom. E-beam is focused onto the material and generates vapor that eventually condenses on the sapphire targets. The platen can spin during coating to obtain high film uniformity. Also it is possible to heat the platen up to 1000 °C if desired, a feature that boosts film quality for certain materials. The built-in e-beam gun has a voltage supply of 5-6 kV and is capable of melting most high temperature materials. Thickness of the deposited thin film is estimated by the built-in crystal monitor, which has a resolution of 1 Å. The PVD-250 also features four material pockets for alternate film coating, in case stacking of different thin film layers is needed. Another helpful feature is the external gas controller, through which oxygen can be injected into the vacuum chamber during deposition to maintain proper stoichiometry when depositing metal oxide thin film materials.

An aluminum holder is machined in house to mount sapphire fibers to the platen inside the chamber for fiber tip coatings, as seen from Figure 2-7. For each coating process, several pieces of sapphire wafers (C-Plane, same as the crystal orientation on the end face of the sapphire fiber) were co-deposited for characterizations of the thin film. After each

deposition, the sapphire wafers were annealed and tested together with the sapphire fiber sensors to characterize the film quality and performance.

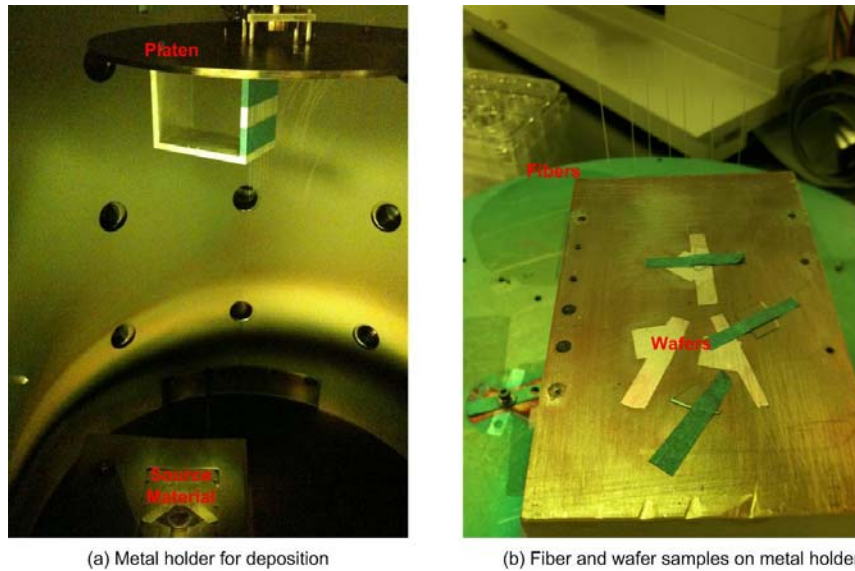


Figure 2-7: Metal holder for film deposition on the fiber and wafer samples

2.3.2 Material selection

An ideal material for the thin-film is desired to meet all of the following criteria:

- Material has higher melting point than maximal required working temperature;
- Refractive index of material is different from that of sapphire in the wavelength range of interest;
- Material has relative low optical absorption in the wavelength range of interest;
- Material is physically and chemically stable by itself and co-existence with sapphire within entire operating temperature range;
- Material has similar coefficient of thermal expansion (CTE) to the sapphire's within temperature range of interest;
- Material has a single phase that is stable over the entire operating temperature range;
- Material can be readily deposited.

Generally speaking, the first five criteria must be met while the last two are highly preferred, although not required. Lesker has a thin film coating table available on their

website [70]. It provides a comprehensive summary of thin film coating materials and their properties as deposited by PVD. For the present work, only the materials that can work at temperature beyond 1000 °C and can be deposited using PVD is studied. Table 2-2 lists the major non-toxic materials that have reasonably close CTE to the sapphire's.

Table 2-2: List of properties of potential thin film materials

Name	Chemical Formula	Melting Point (°C)	PVD readiness	Refractive index@850nm
Aluminum Oxide	Al ₂ O ₃	2072	Excellent	~1.72
Tantalum Pentoxide	Ta ₂ O ₅	1872	Good	~2.60
Titanium Dioxide	TiO ₂	1830	Fair	~2.61
Zirconium Dioxide	ZrO ₂	2700	Good	~2.20
Chromium Oxide	Cr ₂ O ₃	2266	Good	~2.55
Yttrium Oxide	Y ₂ O ₃	1990	Good	~1.79
Hafnium Oxide	HfO ₂	2758	Fair	~1.95

Figure 2-8 shows the accumulated thermal expansion curves of the above materials, according to data from Ref. [71].

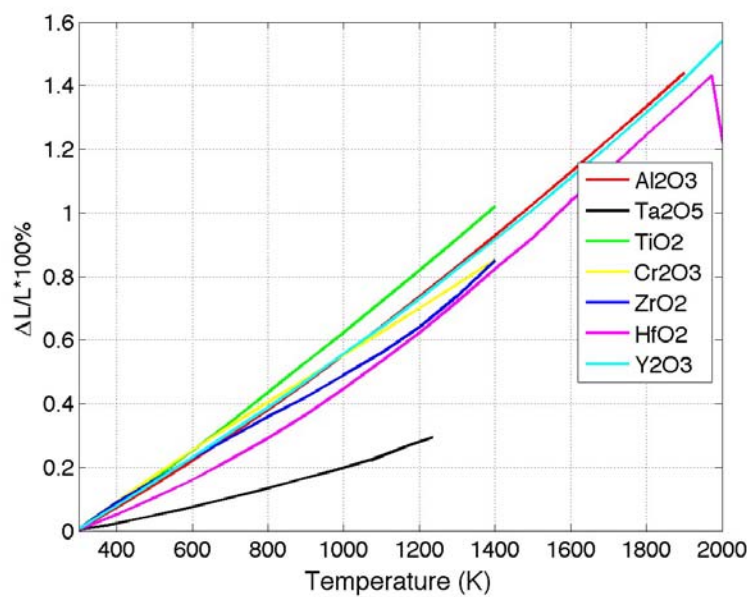


Figure 2-8: Accumulated thermal expansion for some high temperature materials

From Figure 2-8, it is found that TiO_2 , Cr_2O_3 , ZrO_2 , HfO_2 and Y_2O_3 have very close CTE to the sapphire's, only Ta_2O_5 has relatively lower thermal expansion rate. Besides thermal expansion, we also looked at the phase diagram for the thin film materials when co-existing with Al_2O_3 (Sapphire). If within the operating temperature range of our interest, the two materials (the thin film material and Al_2O_3) have additional phases, the new phases need to be considered separately to see if it affects the sensor performance. We firstly tried Ta_2O_5 as the thin film material since Ta_2O_5 is very easy to deposit and then chose TiO_2 because it has closer CTE match to the sapphire's. However TiO_2 and Al_2O_3 would form some a new phase called aluminum titanate (Al_2TiO_5) at temperature beyond $1300\text{ }^\circ\text{C}$ [72]. The new phase Al_2TiO_5 has a thermal expansion coefficient that is quite different from the sapphire's [71]. Thus, it is expected that the TiO_2 thin film sensor will suffer great performance degradation at a temperature above $1300\text{ }^\circ\text{C}$. After the learning of the phase problem from TiO_2 , we studied ZrO_2 as the thin film material since it not only has close CTE to the sapphire's but also maintains separate phase from Al_2O_3 regardless of the temperature [72]. For this reason, the ZrO_2 thin film sensors are expected to work up to higher temperature than TiO_2 ones shall do. In the following section, experimental results will be presented and discussed in details.

2.4 Experiment results

2.4.1 Thick- Ta_2O_5 film sensor

The first thin film sensor studied was coated by a thick- Ta_2O_5 film. The PVD-250 was used in the Clean Room to evaporate the material and to deposit on the tip of the sapphire fiber. Ta_2O_5 tablet (99.99% in purity, Lesker EVMTAO4063B) was filled in a graphite crucible liner (Lesker EVCFABEB-23) for the e-beam evaporation. Before depositing, the sapphire fibers were polished down to $0.5\text{ }\mu\text{m}$ to obtain a good surface smoothness.

2.4.1.1 Deposition of the Ta_2O_5 thin film

Before deposition, sapphire fiber tips and sapphire wafers were cleaned in the Clean Room by an ultrasonic cleaner and then rinsed in alcohol, acetone and deionized water

for three times, to remove possible surface contamination. As shown in Figure 2-9, several pieces of sapphire fibers, silica fibers and sapphire wafers were placed in the PVD-250 for the Ta₂O₅ film coating. The deposition yielded a thin film with a physical thickness around 1.5 μm; key parameters used in the deposition are listed in Table 2-3.



Figure 2-9: Fiber and wafer samples ready for the thick-Ta₂O₅ film deposition

After the deposition, the sapphire fiber sensors were then annealed for more than three temperature cycles from 400 °C up to 1000 °C. The film sensors showed good fringes after annealing.

Table 2-3: Parameters used in the thick-Ta₂O₅ film deposition

Parameter	Value
Deposition rate	6.5 Å/s
Film thickness	~1.5 μm
Partial pressure of O ₂	5×10 ⁻⁵ torr
Substrate temperature	50 °C

2.4.1.2 After-deposition characterization

The Type-I spectrometer was used to interrogate the film on a sapphire wafer right after the deposition. A reflection spectrum of the film is shown in Figure 2-10. Because the

film has a high parallelism, the interferometric signal in Figure 2-10 has a very high fringe visibility seen as a high modulation depth in the measured spectrum.

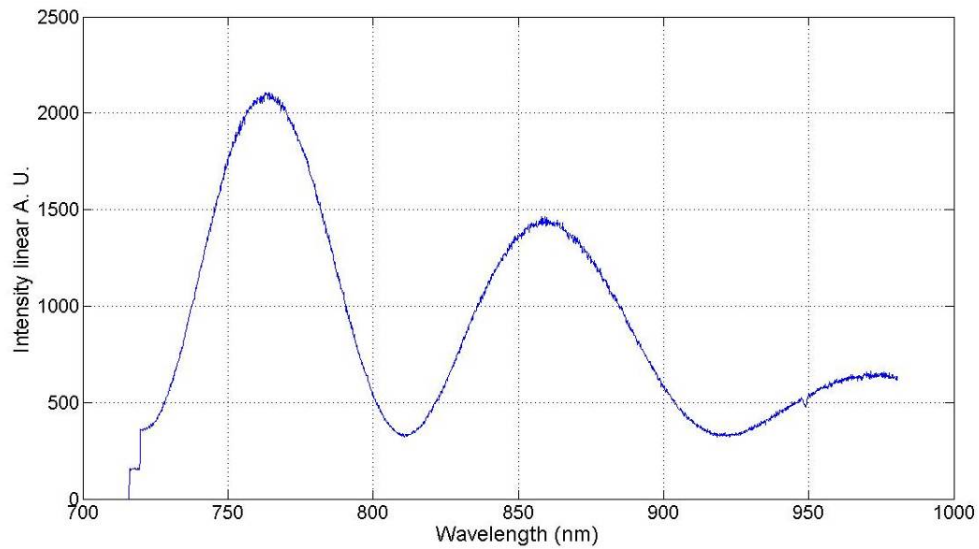


Figure 2-10: Reflection spectrum of the thick-Ta₂O₅ film on a sapphire wafer

Thin film deposited on the sapphire wafer also had a very smooth surface after deposition, as shown in Figure 2-11.

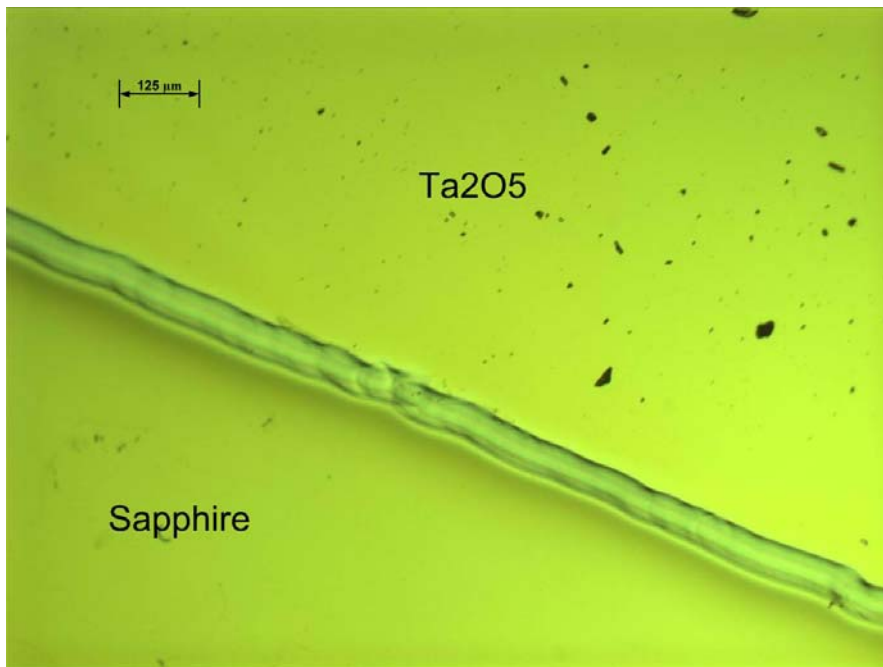


Figure 2-11: Microscopic image of the thick-Ta₂O₅ film on a sapphire wafer

The deposited thin film appeared to be brown in color, but the color faded once the film was annealed at 400 °C. The change in color may be

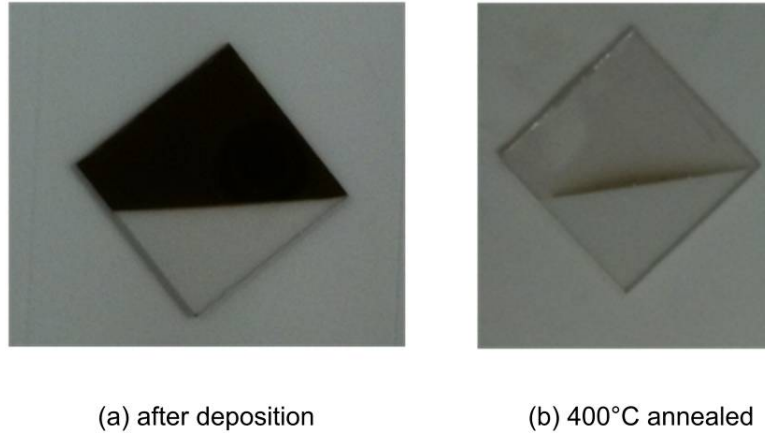
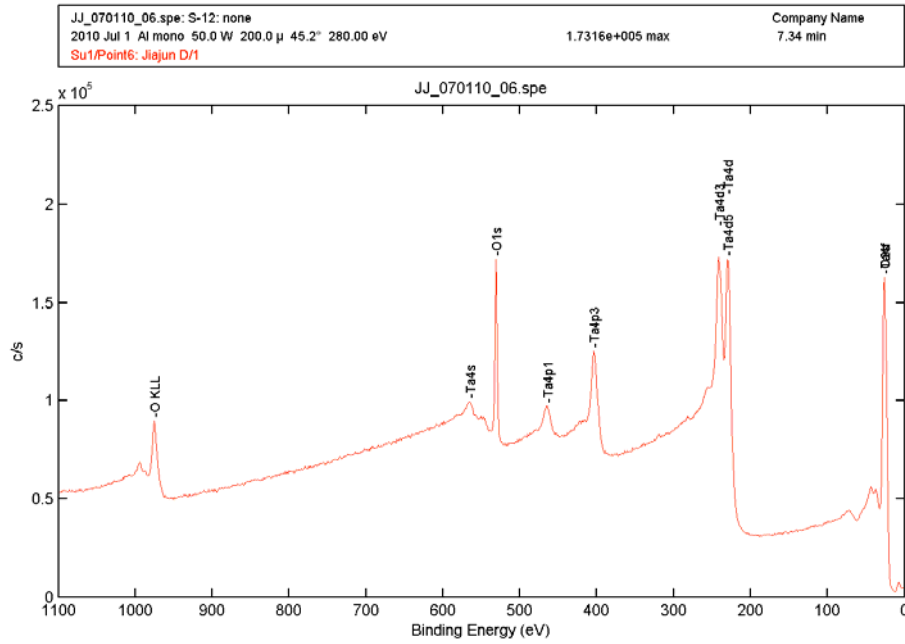


Figure 2-12: Color of the thick-Ta₂O₅ thin film

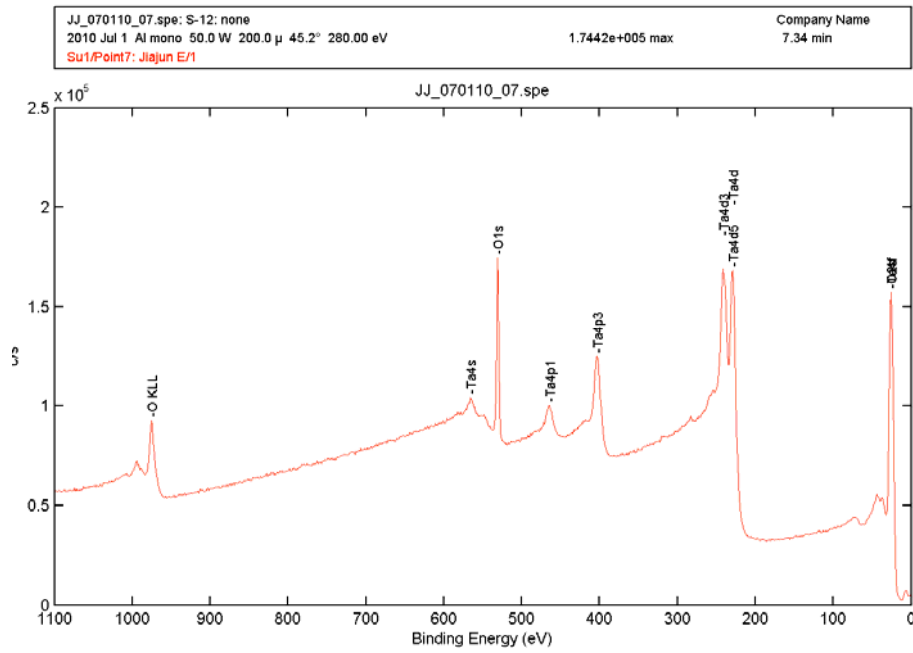
X-ray photoelectron spectroscopy (XPS) was used to characterize the film composition to determine if the thin film had correct stoichiometry. The spectroscopic results give the material composition at the very top of the film (typically about 10 nm). Thus the rough stoichiometry and possible contaminations are found from the XPS results. The XPS results for the sapphire wafers with the Ta₂O₅ film are shown in Figure 2-13. From the results, we have a concentration list in Table 2-4. It is found from the results that no apparent contamination was found from both samples. Also the oxygen-tantalum did not change after annealing.

Table 2-4: Atomic concentration for the thick-Ta₂O₅ film on a sapphire wafer

	O1s	Ta4f
After deposition	64.95%	35.05%
1000 °C annealed	65.29%	34.71%



(a) Film after deposition



(b) Film annealed at 1000 °C

Figure 2-13: XPS result of the thick-Ta₂O₅ film wafer samples

Another interesting aspect is that the OPD of the deposited film would change after the first annealing at 400 °C. The reason is suspected to be the changing in molecular

formation in the film. Film as deposited from PVD is supposed to be amorphous, but would be become more compact after the first annealing. Therefore the physical thickness and the refractive index both change after the first annealing. Figure 2-14 provides an example of such change as seen from measured spectra.

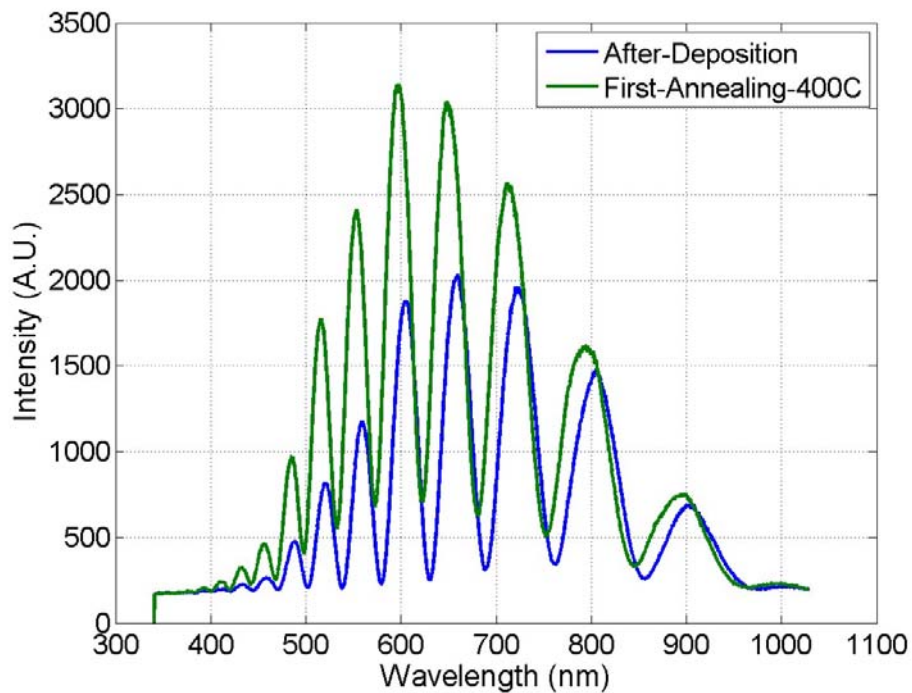


Figure 2-14: OPD changes after the first annealing at 400 °C

2.4.1.3 Testing and calibration

Post-deposition annealing was carried out at 400 °C, 600 °C, 800 °C and 1000 °C, each for at least 2 hours to stabilize the thin film. Before the sensor was calibrated, three more temperature cycles from ambient temperature to 1000 °C were carried out to enhance the repeatability of the thin film sensors. Figure 2-15 shows sampled spectra of the sensor measured at different temperatures.

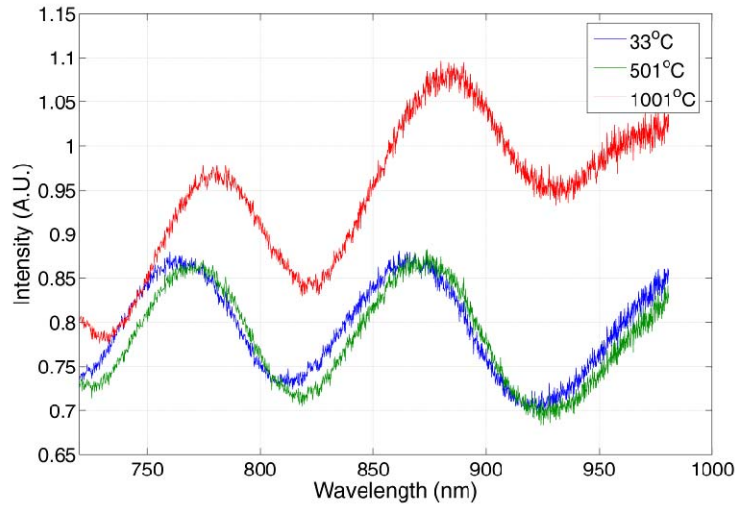


Figure 2-15: Spectra of the thick-Ta₂O₅ film sensor at different temperatures

From Figure 2-15, we can see that the sensor had clear fringes that are shifting as temperature varies. Also it is noticed that at high temperature (1001 °C) the blackbody radiation introduces a slope in the measured spectrum (Red in Figure 2-15).

The thin film sensor was then calibrated using a furnace (Thermolyne 48000), which was heated from 200 °C to 1000 °C at 3 °C/min and then cooled at the same rate. Spectra were averaged 50 times to be a spectrum for signal processing, to reduce the noise from the light source before the peak-tracking method was applied to locate the peaks and valleys. The peak-tracking method found the relative wavelength shift for each of the two peaks and two valleys in Figure 2-15 throughout the heating and cooling process; and the reference temperature measurements were taken using a k-type thermocouple. These four values of $\Delta\lambda/\lambda$ were averaged to obtain an accurate measurement of the wavelength shift versus temperature (Figure 2-16). A third-order polynomial curve was fitted to the measured data to obtain a full-scale sensor calibration curve. A very small level of hysteresis, defined as different readings from the heating and the cooling process, is seen from the graph.

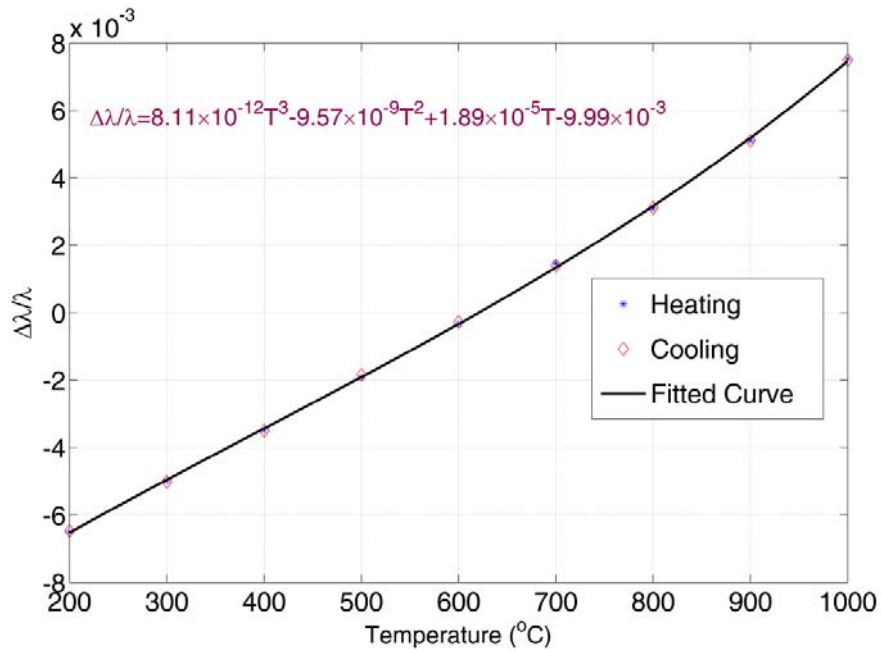


Figure 2-16: Calibration curve of the thick-Ta₂O₅ thin film sensor

Given the data showing in Figure 2-16, the sensitivity of the sensor is calculated to be,

$$S = \frac{\Delta\lambda}{\lambda \cdot \Delta T} = \frac{13.98 \times 10^{-3}}{800\text{K}} = 1.75 \times 10^{-5} / ^\circ\text{C} \quad \text{Equation 2-8}$$

The resolution of the peak-tracking measurement was quantified by monitoring the thin-film sensor at a constant temperature of 600 °C. A total of 700 samples were acquired during a 2-hour non-stop test in which the located peak wavelengths had a two-sigma variation of only 0.02 nm, as seen from Figure 2-17.

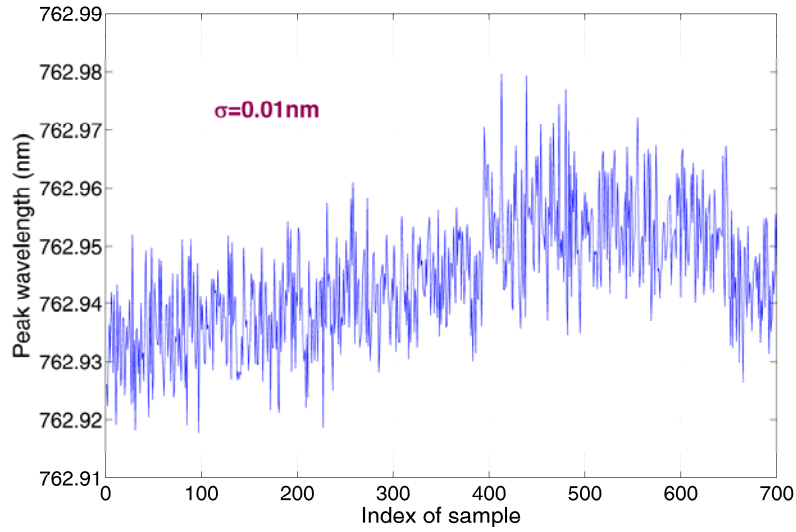


Figure 2-17: Fluctuation of wavelength shifts for the thick-Ta₂O₅ film sensor

Given the sensitivity calculated from Equation 2-8, the temperature resolution is further calculated as in Equation 2-9.

$$R_T = \frac{2\sigma}{\lambda_0 \cdot S} = \frac{2 \times 0.01}{762.95 \times 1.75 \times 10^{-5}} \text{ } ^\circ\text{C} = 1.5^\circ\text{C} \quad \text{Equation 2-9}$$

Thus, the sensor had a 2σ resolution of 1.5°C . On the other hand, hysteresis of the sensor is defined by the maximal discrepancy of peak wavelength between the heating and the cooling process at a same temperature, which was found to be $\pm 4^\circ\text{C}$ from calibration curve shown in Figure 2-16. An important aspect has to be pointed out here is that sensor was calibrated with the blackbody radiation treated as part of the sensor signal because the measured blackbody radiation intensity was relatively low at most of the calibration temperatures. No extra measurements were taken to eliminate the intensity from the blackbody radiation. For the wavelength range that covers the peaks and valleys, the blackbody radiation at 900°C and 1000°C has an increasing slope in intensity as wavelength becomes larger. If the blackbody radiation is taken as part of the sensor's spectrum, the peak tracking method would identify the peak at a wavelength longer than the true values. Such effect results in slightly increased sensitivity that what is shown in Equation 2-8.

2.4.2 Thin-Ta₂O₅ film sensor

After having demonstrated the thick-Ta₂O₅ film sensor, the work focus was to extend the working temperature range of such thin film sensors. One way to achieve so is to reduce the film thickness to reduce degradation of film quality by micro-cracking at high temperatures.

Since the Type II spectrometer has a wavelength range from 320 nm to 1000 nm, the minimal OPD required to see a whole fringe period can be calculated to be,

$$OPD = \frac{\lambda_1 \lambda_2}{\Delta \lambda} = \frac{0.32 \times 1.0}{0.7} \mu m = 457 nm \quad \text{Equation 2-10}$$

This number is much smaller than what the thick-Ta₂O₅ film sensor had. In other words, it is viable to reduce the film thickness of the film sensor to attempt sensors with higher working temperature. On the other hand, as the film thickness reduces, the measured reflection spectrum will have much broader peaks and valleys. It may introduce greater error in the central wavelength determination. Also it may no longer possible to use the averaged relative wavelength shifting from multiple peaks and valleys to suppress error. Given these, thinner film will have poorer temperature resolution and accuracy. A trade-off between temperature performance and sensor resolution needs to be taken when deciding the film thickness.

2.4.2.1 Deposition of the Ta₂O₅ thin film

The thin-Ta₂O₅ film sensors were fabricated using the same material and crucible as the ones used for the thick-Ta₂O₅ deposition described in previous section. Key parameters are listed in Table 2-5, which are same as the ones in Table 2-3 except for the film thickness.

Table 2-5: Parameters used in the thin-Ta₂O₅ film deposition

Parameter	Value
Deposition rate	6.5 Å/s
Film thickness	~0.7 μm
Partial pressure of O ₂	9×10 ⁻⁵ torr
Substrate temperature	40 °C

2.4.2.2 After-deposition characterization

The deposition procedure was the same as described in the previous section. The sapphire fiber end surface was inspected under microscope after deposition, whose results are seen in Figure 2-18.



Figure 2-18: Microscopic image of the sapphire fiber with the thin-Ta₂O₅ film

After deposition, the spectrum of the sensor was measured and is presented in Figure 2-19. The OPD of sensor was estimated to be 2.7 μm, based on the peak wavelengths in the spectrum. The spectrum shown in Figure 2-19 was obtained by normalizing the measured sensor spectrum to the spectrum of the light source. (Sometime we call this *normalized spectrum* even it is not truly normalized in intensity.)

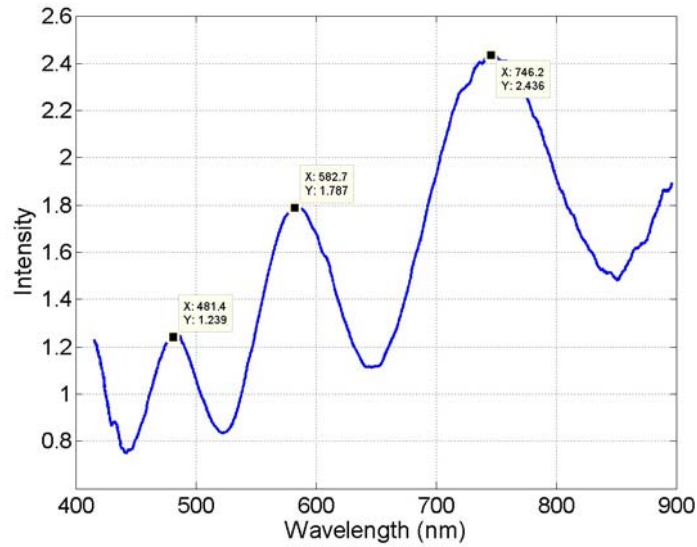


Figure 2-19: Spectrum of the thin-Ta₂O₅ film sensor after deposition

Figure 2-19 is an example that shows the transmission spectrum $\beta(\lambda)$ in the sapphire fiber sensor system as described in Equation 2-5. The “normalized” spectrum shows lower intensity at shorter wavelength and higher intensity at longer wavelength. The results shown in this section did not have the $\beta(\lambda)$ compensated.

2.4.2.3 Testing and calibration

The thin-Ta₂O₅ film sensor was annealed from 400 °C to 1200 °C, with a temperature increment of 200 °C. After fully annealing, three more temperature cycles from ambient temperature to 1200 °C were carried out to enhance the film repeatability before calibration was attempt on the sensor. Figure 2-20 shows spectra of the sensor measured at different temperatures.

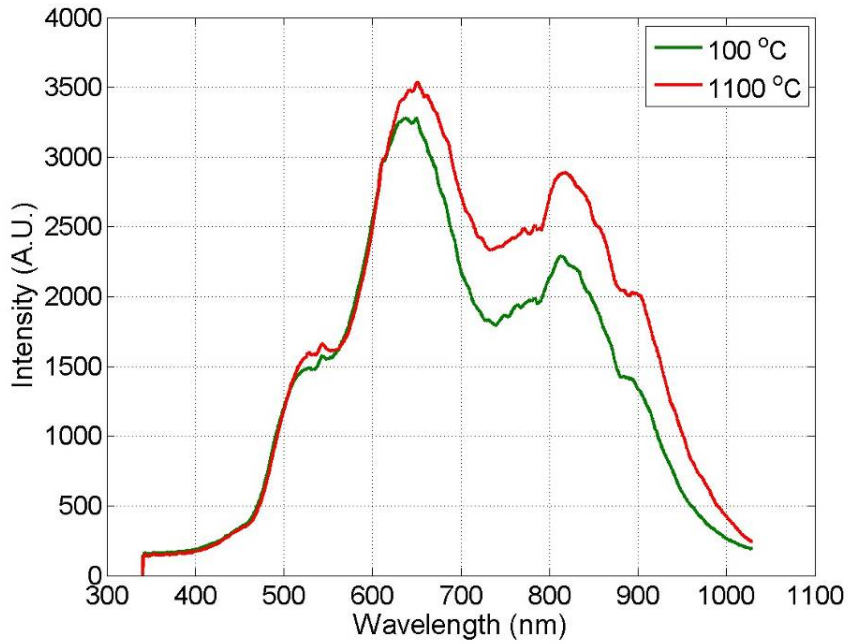


Figure 2-20: Spectra of the thin-Ta₂O₅ sensor measured at different temperatures

During calibration, the central wavelength of the first peak was monitored when the temperature of the furnace was controlled from 100 °C to 1100 °C. Figure 2-21 provides the wavelengths of the fitted peak at all calibration temperatures.

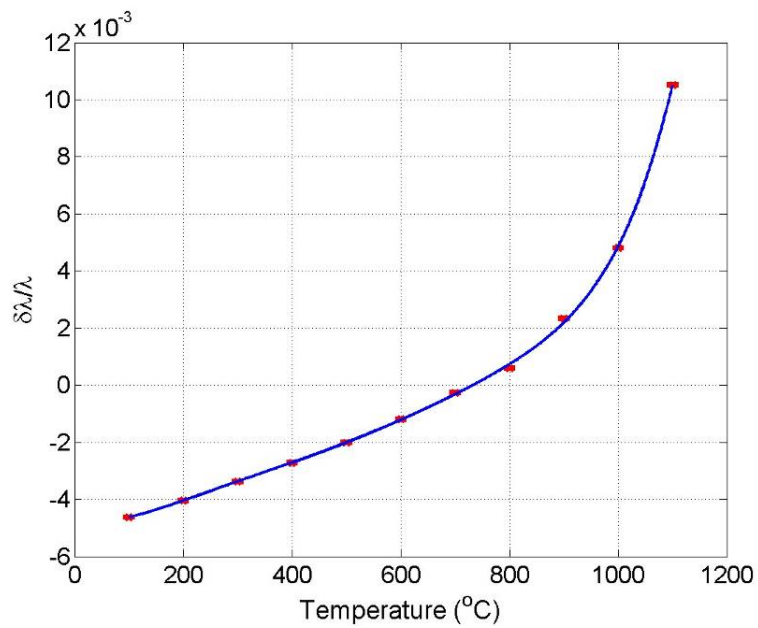


Figure 2-21: Calibration curve of the thin-Ta₂O₅ film sensor

The curve shown in Figure 2-21 has a constant slope at low temperature range (less than 800 °C) but a much larger slope at high temperature range (800 °C to 1100 °C). This is caused by the blackbody radiation. The intensity of the blackbody radiation increases dramatically at higher temperature and the peak wavelength of the blackbody radiation is located at the long wavelength region of the spectrometers. The effect of the blackbody radiation is to introduce an increasing background in the total measured spectrum. The peak wavelength of the interferometric fringes is shifted toward longer wavelength while the valley wavelength is shifted toward shorter wavelength. Thus the peak-tracking method identifies peak wavelengths to be larger than the true values. Thus, the peak wavelengths in Figure 2-21 increase sharply at higher temperatures. At the time the data were taken, there were no measures to eliminate the wavelength shifting by the blackbody radiation. The “sensitivity” of the sensor shown in Figure 2-21 is calculated to be,

$$S = \frac{\Delta\lambda}{\lambda \cdot \Delta T} = \frac{15.1 \times 10^{-3}}{1000\text{EC}} = 1.51 \times 10^{-5} / ^\circ\text{C} \quad \text{Equation 2-11}$$

The sensor’s resolution is also defined by the maximal central wavelength fluctuation at all calibration temperatures. In this case, that was found to be at the temperature of 1100 °C. The results are seen from Figure 2-22.

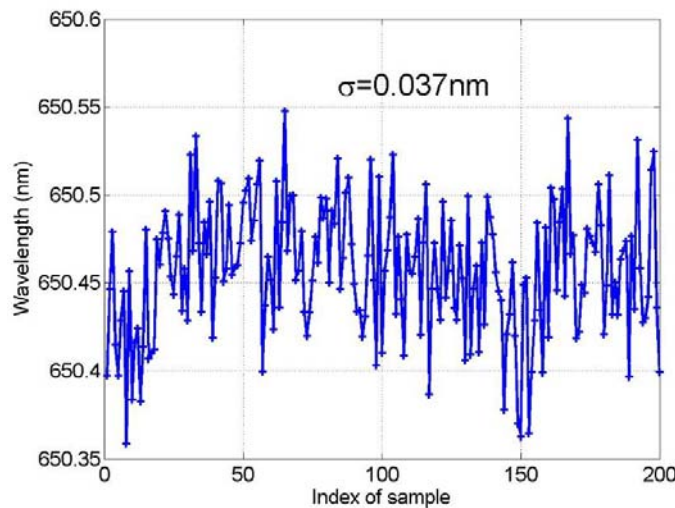


Figure 2-22: Fluctuation of resolved peak wavelengths at 1100 °C

Given the sensitivity calculated from Equation 2-13, the temperature resolution is in-turn calculated to be 7.5 °C.

$$R_T = \frac{2\sigma}{\lambda_0 \cdot S} = \frac{2 \times 0.037}{650.46 \times 1.51 \times 10^{-5}} \text{ } ^\circ\text{C} = 7.5^\circ\text{C} \quad \text{Equation 2-12}$$

The temperature resolution of the thin- Ta₂O₅ film sensor is much larger than that of the thick-Ta₂O₅ film sensor. The reduced temperature resolution is mainly caused by the lower wavelength resolution of the Type II spectrometer.

2.4.3 TiO₂ film sensor

As can be seen from Figure 2-8, TiO₂ has a much closer CTE matching to the sapphire's than Ta₂O₅ does. After Ta₂O₅ was studied as the thin film material, TiO₂ was investigated in order to fabricate sensors that can survive at higher temperatures. 99.9% TiO₂ (Lesker, EVMTIO2314B) was filled in a graphite liner (Lesker EVCFABEB-23) for e-beam evaporation.

2.4.3.1 Deposition of the TiO₂ film

Multiple sapphire fiber and wafer samples were mounted on the metal holder for the TiO₂ film deposition, as shown in Figure 2-23.



Figure 2-23: Samples for the TiO₂ thin film deposition

Compared with Ta₂O₅, TiO₂ is very volatile and is hard to evaporate. Although the TiO₂ film was deposited at a rate of about 4 Å/s, the E-beam has to be carefully controlled to avoid sparking in both crucible pre-conditioning and actual deposition. The manual deposition mode of the PVD-250 was used because of the random sparking that reduces the film quality. Table 2-6 lists some of the key parameters used in the TiO₂ film deposition.

Table 2-6: Parameters used for the TiO₂ film deposition

Parameter	Value
Deposition rate	4.0 Å/s
Film thickness	~700 nm
Partial pressure of O ₂	6×10 ⁻⁵ torr
Substrate temperature	40 °C

2.4.3.2 After deposition characterization

The TiO₂ film deposition followed a similar cleaning procedure as the one used in the Ta₂O₅ film deposition. After deposition, the TiO₂ film deposited on the sapphire wafer appears to be transparent, as can be seen from Figure 2-24.

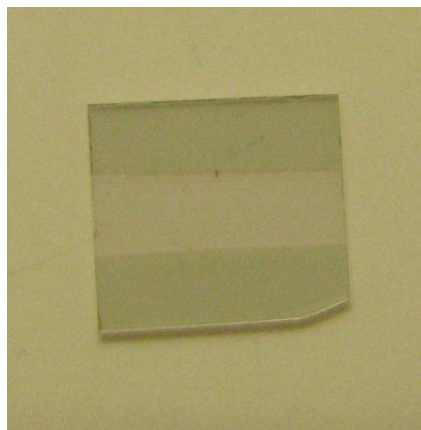


Figure 2-24: TiO₂ film deposited on a sapphire wafer

The sapphire fiber coated with the TiO₂ thin film also had a very smooth surface, as seen from Figure 2-25.

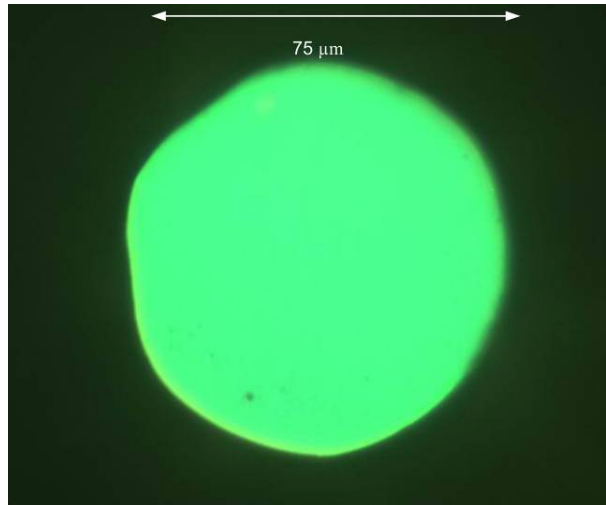


Figure 2-25: TiO₂ film deposited on the tip of a sapphire fiber

The sapphire fiber sensor had very good fringe visibility after deposition, as shown in Figure 2-26.

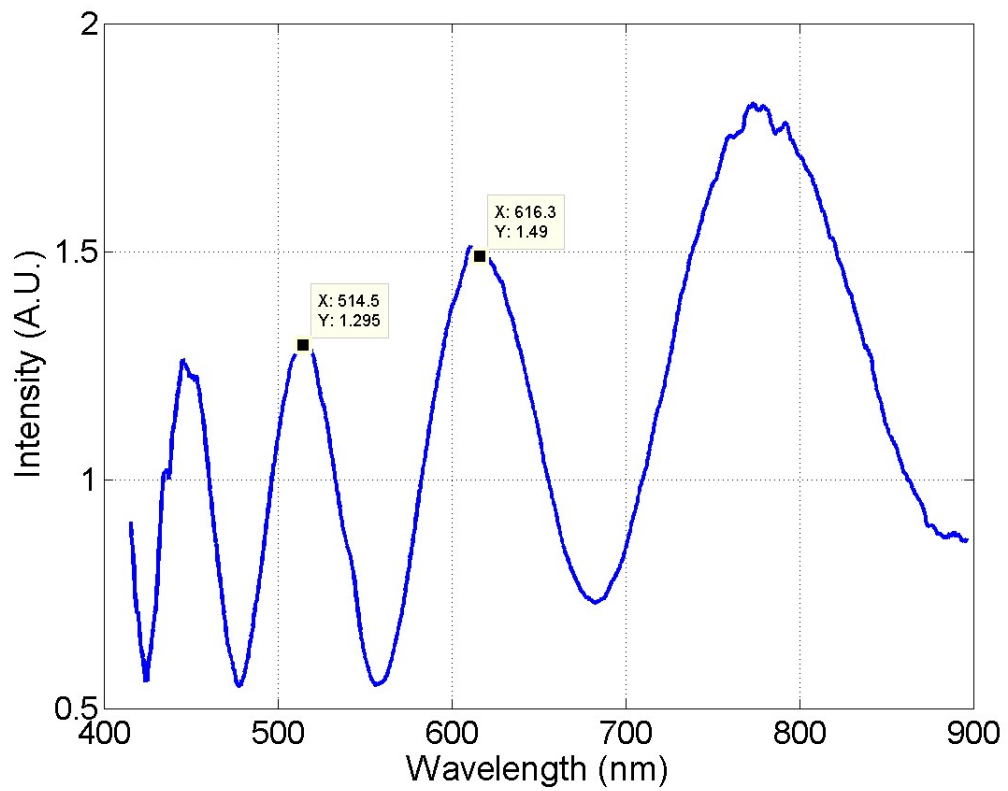


Figure 2-26: Spectrum of the TiO₂ film sensor after deposition

The OPD of the TiO₂ thin film can be roughly estimated based on the peak wavelengths shown in the above spectrum.

$$OPD = \frac{\lambda_1 \lambda_2}{\Delta\lambda} = \frac{0.5145 \times 0.6163}{0.1018} \mu m = 3.1 \mu m \quad \text{Equation 2-13}$$

The calculated OPD (3.1 μm) agrees with the measured film thickness in Table 2-6. The post-annealing started at 400 °C and then increased to 1200 °C at an increment of 200 °C, for at least 2 hours at each temperature. Figure 2-27 shows the microscopic surface picture of the TiO₂ film on a sapphire wafer after annealing at different temperatures.

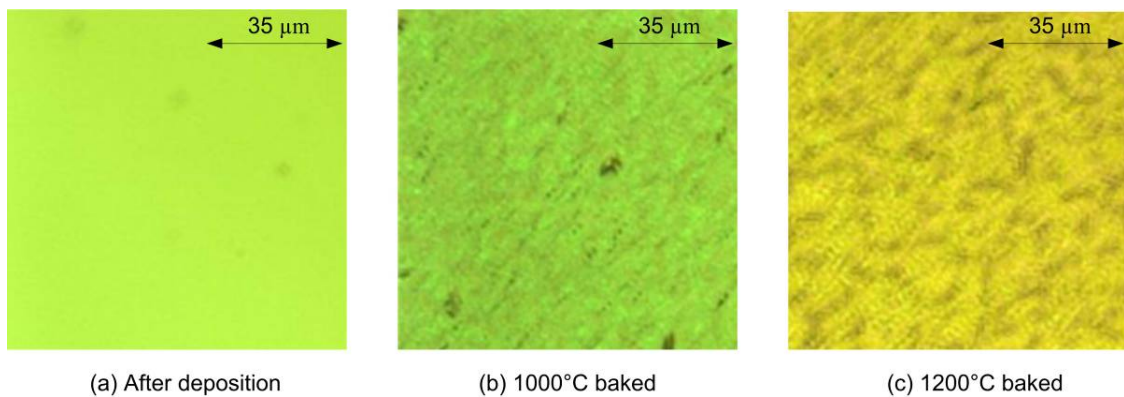


Figure 2-27: Microscopic images of the TiO₂ film annealed at different temperatures

From Figure 2-27 we can see that the film had a very smooth surface after deposition. As the annealing temperature increased, the film started to re-organize and the surface started to show a lot of micro cracking especially after annealed at 1200 °C.

XPS was also used to study the TiO₂ film composition, whose results are seen in Figure 2-28.

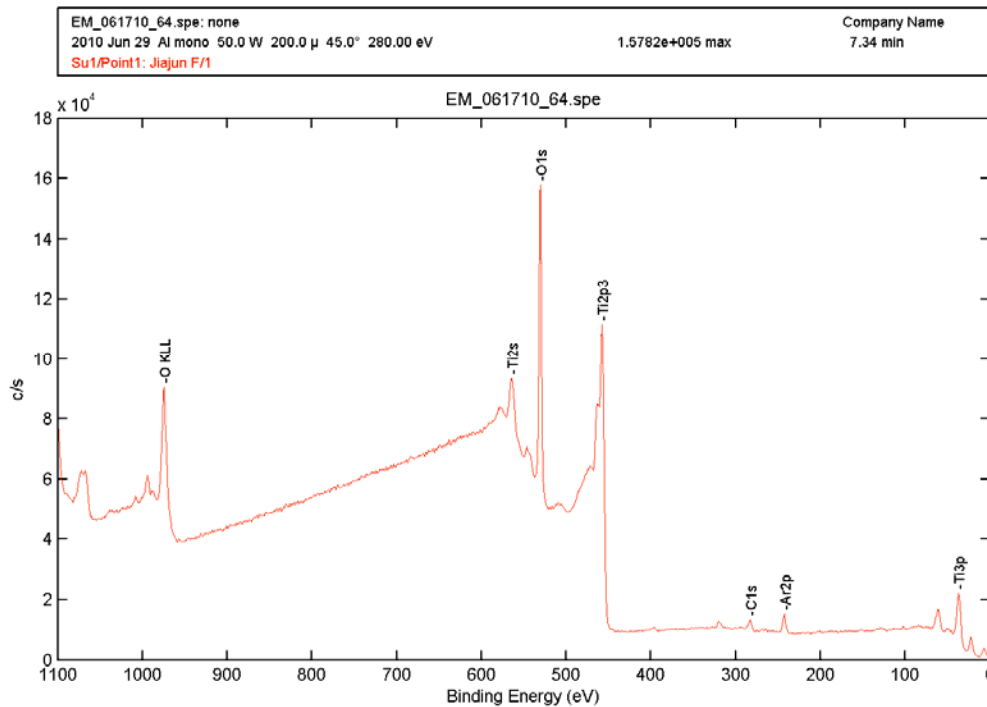


Figure 2-28: XPS result of the TiO₂ film after deposition

The total concentration is listed in the Table 2-7.

Table 2-7: Atomic concentration of the TiO₂ film on a sapphire wafer

	O1s	Ti2p	C1s
After deposition	61.31%	32.75%	5.94%

The film was mainly consisted of titanium and oxygen with approximately correct stoichiometry. However, certain percentage of carbon was also detected because of the tape used to fix the sample when performing XPS. As a conclusion, the XPS results did not show any significant contamination on the TiO₂ thin film sample and the stoichiometry seemed to be correct.

2.4.3.3 Testing and calibration

After annealing the film sensor at different temperatures, three more cycles from room temperature to 1200 °C were performed to enhance the repeatability of the TiO₂ film

sensor. Figure 2-29 shows the fringes of the sensor measured at 1200 °C. Clear fringes are seen on top of the background of the light source. The following spectrum had the blackbody radiation subtracted from the total spectrum, as described in Equation 2-5.

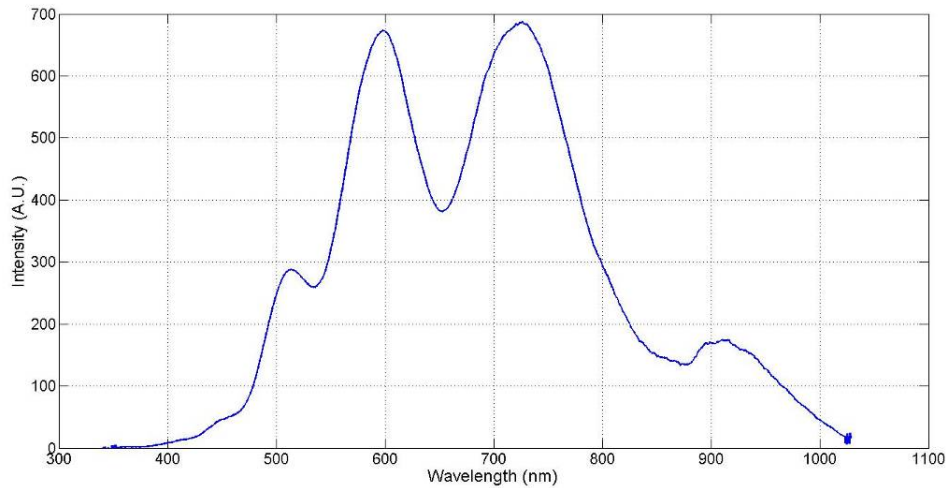


Figure 2-29: Fringes of the TiO₂ film sensor at 1200 °C

When testing the sensor at higher temperatures, we found the blackbody radiation induced intensity on the spectrometer can be several times more than the reflection from the film sensor, as was discussed in previous sections. Figure 2-30 gives a quantitative result of this problem. The measured intensity of the blackbody radiation (Green line) is around 5 times that of the reflections from the film sensor (Blue line).

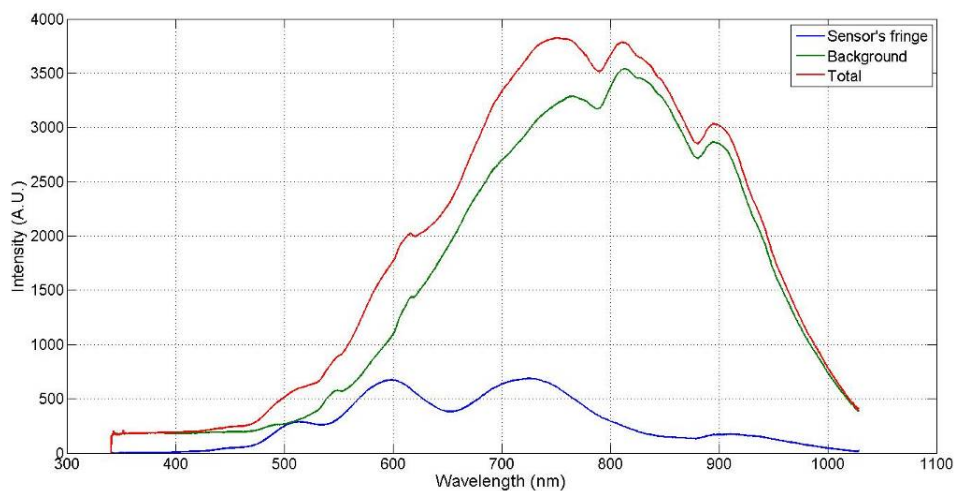


Figure 2-30: Blackbody radiation vs. fringes from the TiO₂ film sensor at 1200 °C

Applying the same calibration method from 300 °C to 1100 °C, using the Type III spectrometer, we recorded spectra of the sensor at different temperatures and plot them in Figure 2-31. It is found that the spectrum clearly shifts toward longer wavelength as temperature increases.

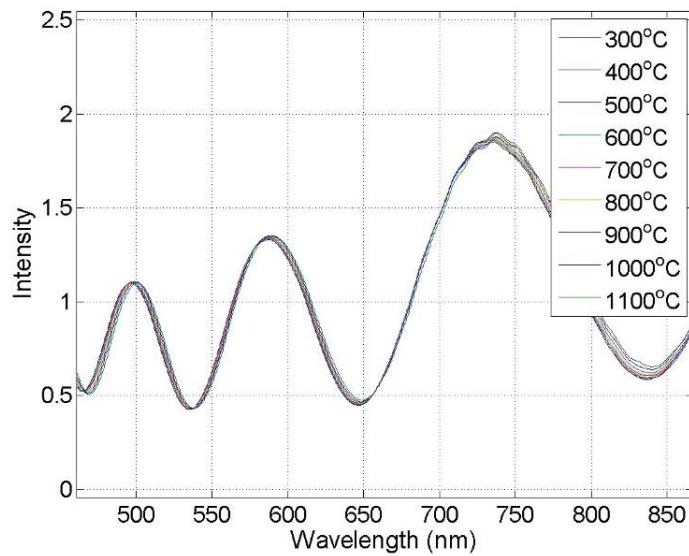


Figure 2-31: Reflection spectra shift as temperature changes

By analyzing the spectra recorded at different temperatures, the sensor's calibration curve with error bar is plotted in Figure 2-32. In this calibration, the blackbody radiation was compensated using the method discussed in sections 2.2, for the first time. However the transmission spectrum was not compensated when processing data for this calibration.

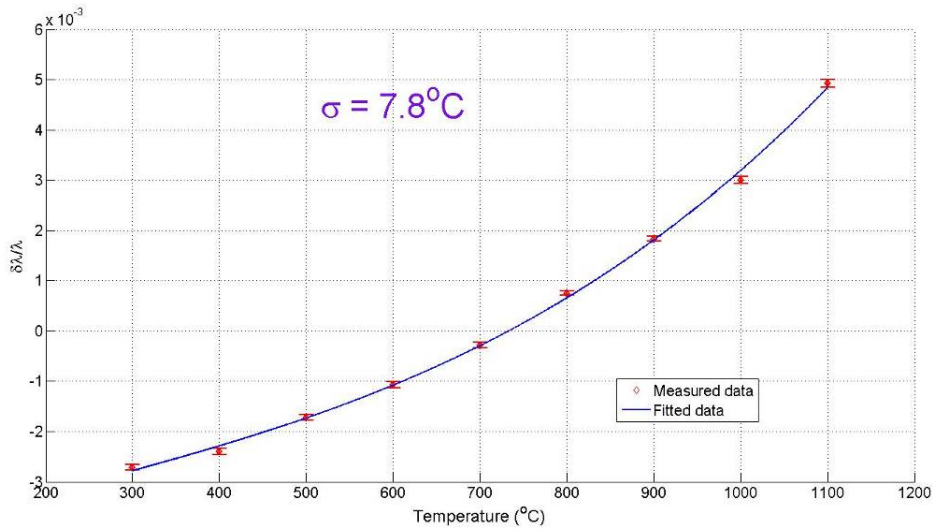


Figure 2-32: Calibration curve of the TiO₂ film sensor

From Figure 2-32 we can calculate the sensitivity of the TiO₂ film sensor.

$$S = \frac{\Delta\lambda}{\lambda \cdot \Delta T} = \frac{7.64 \times 10^{-3}}{800^\circ\text{C}} = 9.55 \times 10^{-6} / ^\circ\text{C} \quad \text{Equation 2-14}$$

To study the resolution of the TiO₂ thin film sensor, the sensor was tested at constant temperatures and the readings from the peak-tracking method were analyzed. The largest fluctuation in the sensor's readings at stable temperatures is found to be at 1100 °C. 100 samples were acquired and the results are plotted in Figure 2-33.

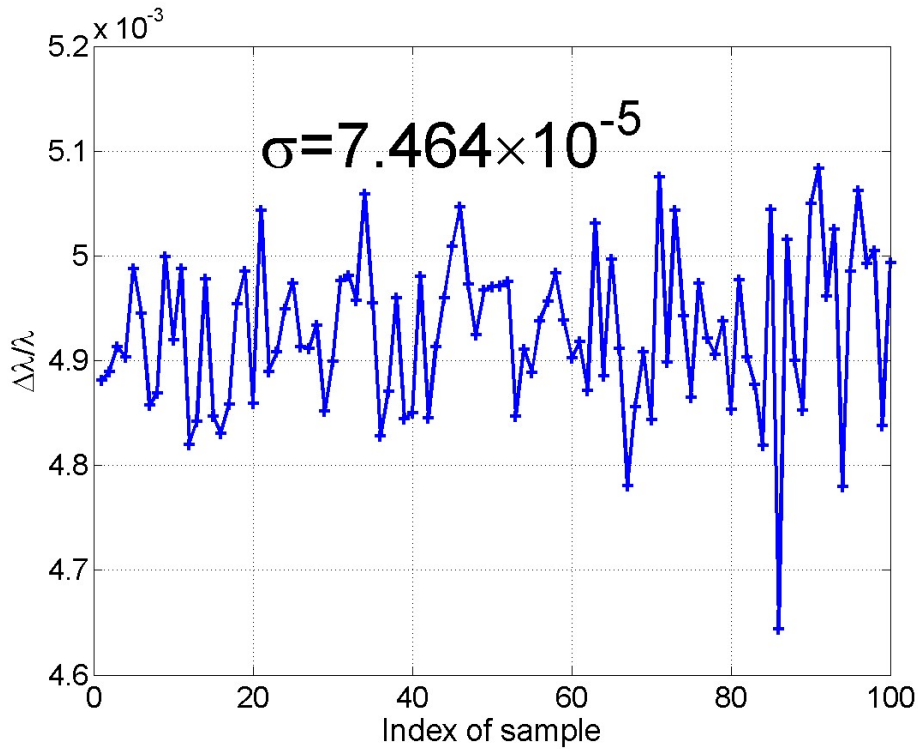


Figure 2-33: Resolution of the TiO₂ film sensor

Given the standard deviation of the relative wavelength shift shown in Figure 2-33, the corresponding temperature resolution is calculated in Equation 2-15.

$$R_T = \frac{2\sigma}{S} = \frac{2 \times 7.464 \times 10^{-5}}{9.55 \times 10^{-6}} \text{ } ^\circ\text{C} = 15.6^\circ\text{C} \quad \text{Equation 2-15}$$

In order to test the long-term stability of the film sensor, the TiO₂ sensor was kept at 1000 °C for 48 hours consecutively. Spectra were recorded after 24 hours and 48 hours. No apparent change was found from the spectra in Figure 2-34. It is believed that the film sensor shall be stable once it has been annealed at a temperature higher than the maximal desired working temperature.

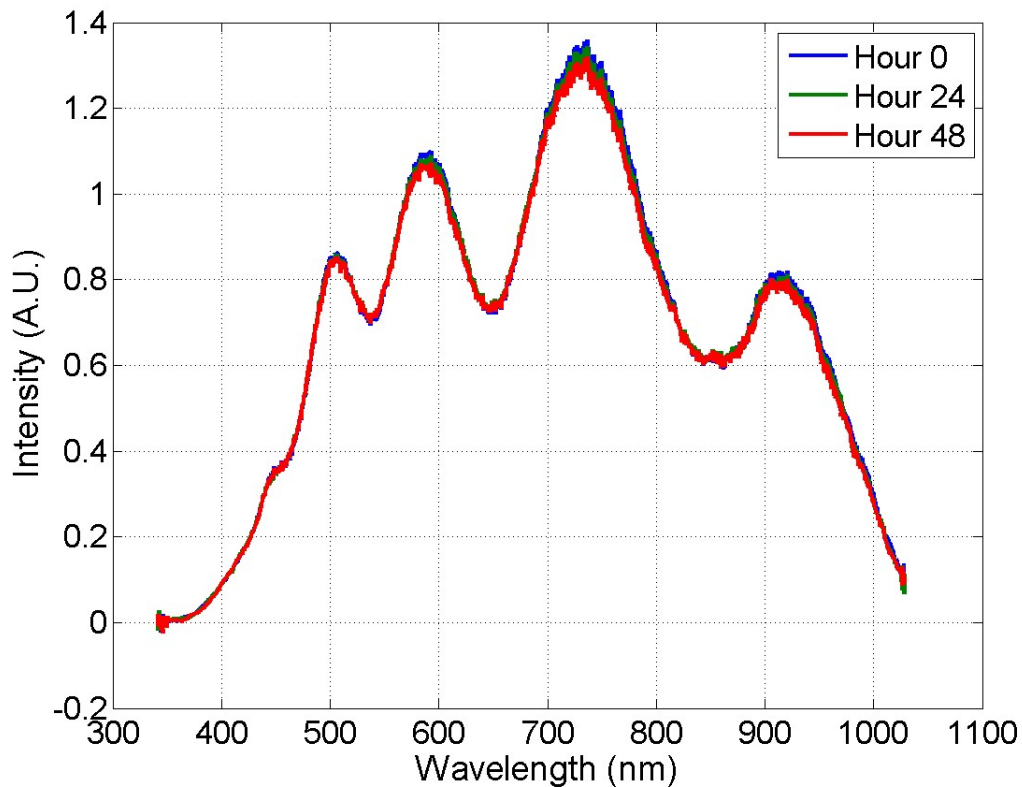


Figure 2-34: Long-term stability test of the TiO₂ film sensor

2.4.4 ZrO₂ film sensor

After the study of the TiO₂ thin film sensor, it was realized that the film material is preferred not to have extra phases when co-existing with sapphire within the entire working temperature range, in addition to having close CTE match to the sapphire's. ZrO₂ was found to be one of such materials and an easy one to deposit. 99.99% ZrO₂ (International Advanced Materials) was filled into the graphite crucible (International Advanced Materials) for the e-beam evaporation in the PVD-250. Unlike TiO₂, ZrO₂ can be readily evaporated and deposition rate can be as high as 20 Å/s, a number measured by the crystal monitor in the PVD-250.

2.4.4.1 Deposition of the ZrO₂ film

Figure 2-35 shows a picture of the metal holder with multiple sapphire fiber samples inside the ceramic tubes. Also attached to the metal holder were sapphire wafer samples

and multi-mode silica fiber samples for film characterization. Table 2-8 lists the key parameters used in the ZrO₂ thin film deposition.

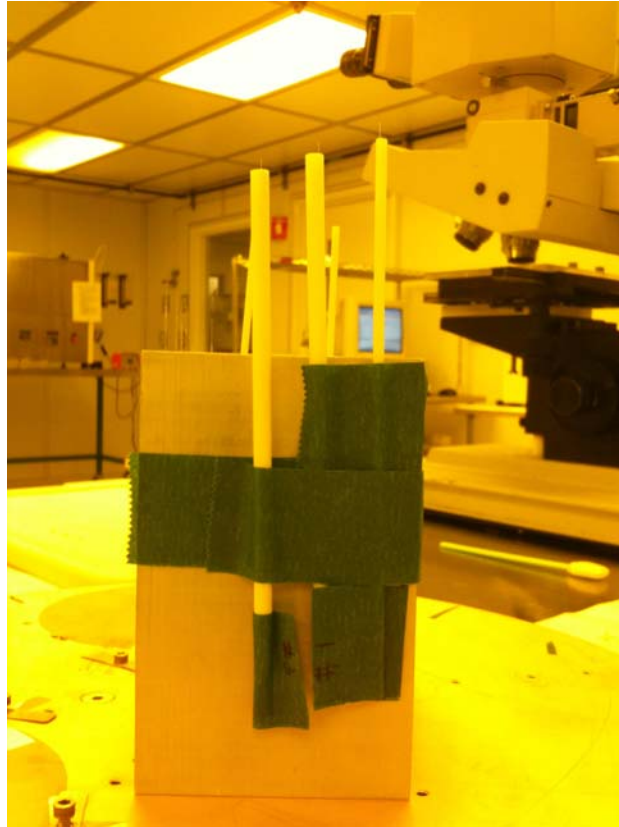


Figure 2-35: Samples ready for the ZrO₂ film deposition

Table 2-8: Parameters used for the ZrO₂ film deposition

Parameter	Value
Deposition rate	8.0 Å/s
Film thickness	~650 nm
Partial pressure of O ₂	N/A
Substrate temperature	43 °C

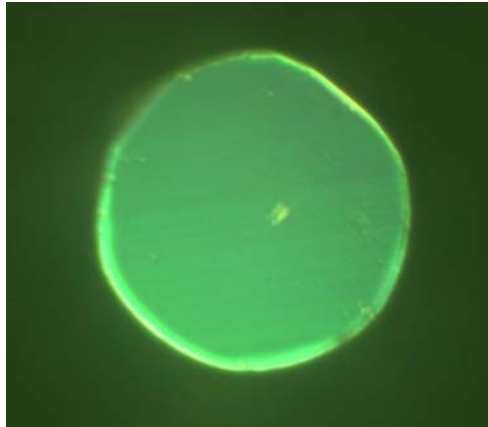


Figure 2-36: Microscopic image of a sapphire fiber with the ZrO₂ film coated

Figure 2-36 shows a microscopic image of a sapphire fiber (~75 μm in diameter) with the ZrO₂ film coated on the tip. A spectrum measured after deposition is shown in Figure 2-37. The normalized spectrum also shows a significant background slope, which is a result of the transmission spectrum $\beta(\lambda)$ as discussed previously.

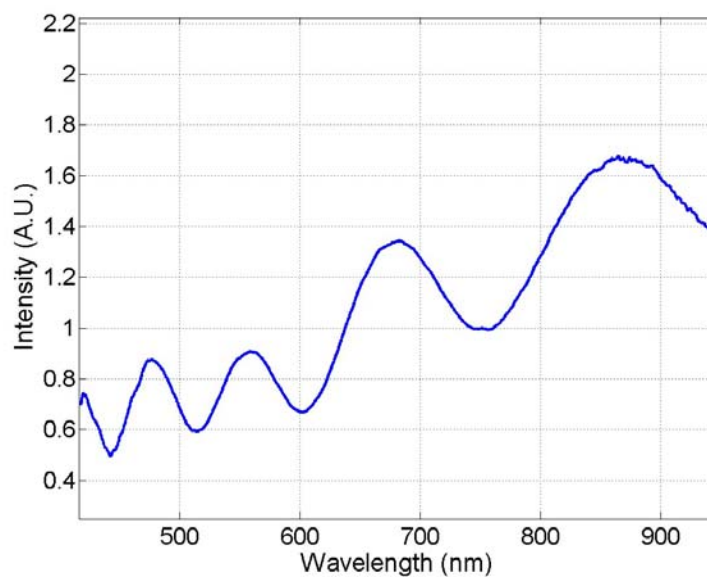


Figure 2-37: Spectrum of the ZrO₂ film sensor measured after deposition

2.4.4.2 After deposition characterization

The sapphire wafer samples were annealed and tested after deposition. The annealing was taken at 400 °C, 800 °C, 1200 °C, 1300 °C, 1400 °C and 1500 °C for more than 2 hours at

each temperature. After each annealing process, the samples were cooled down to ambient temperature and then inspected by the microscope and the optical interrogation system before it was annealed at the next temperature. Figure 2-38 gives microscopic pictures of the wafer sample after it was annealed at different temperatures. The ZrO_2 thin film had a very smooth surface after deposition. The annealing up to $1200\text{ }^\circ\text{C}$ did not change the surface roughness much due to the close match of the CTE between zirconia and sapphire. After annealed at $1500\text{ }^\circ\text{C}$, the surface roughness became worse but was still good enough to offer decent interferometric fringes as will be illustrated in following figures.

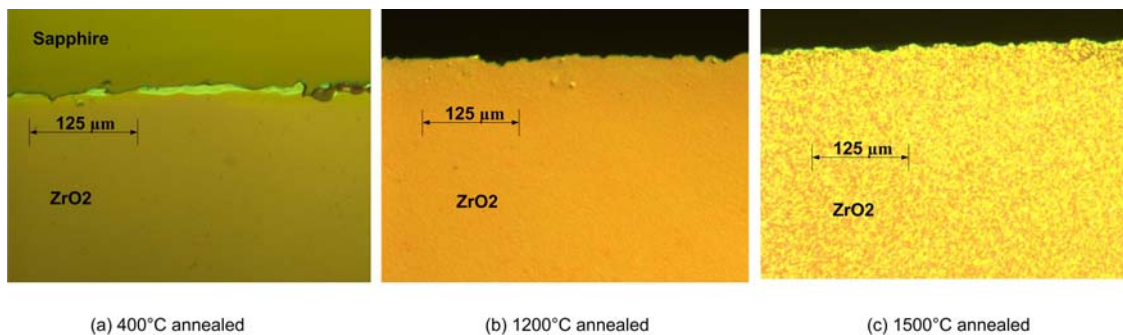


Figure 2-38: Microscopic images of the ZrO_2 film annealed at different temperatures

The film deposited on the sapphire wafer appeared to be quite transparent after it was annealed at $400\text{ }^\circ\text{C}$. But once the sample was annealed at $1500\text{ }^\circ\text{C}$, it turned a little opaque and showed somewhat pink in color, as is seen from Figure 2-39. Figure 2-40 gives “normalized” fringes of the wafer sample measured at ambient temperature after the $1500\text{ }^\circ\text{C}$ annealing.

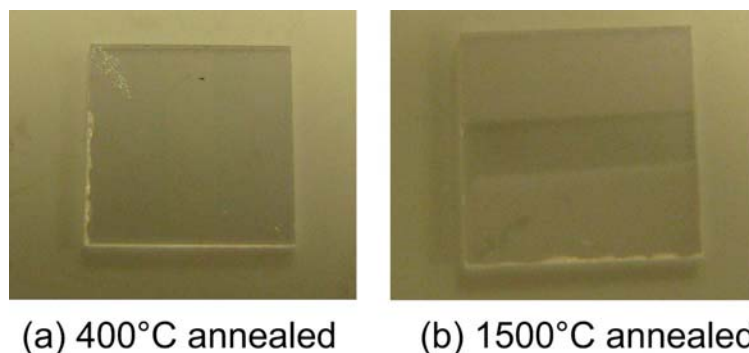


Figure 2-39: Pictures of the ZrO_2 film on the sapphire wafer sample after annealing

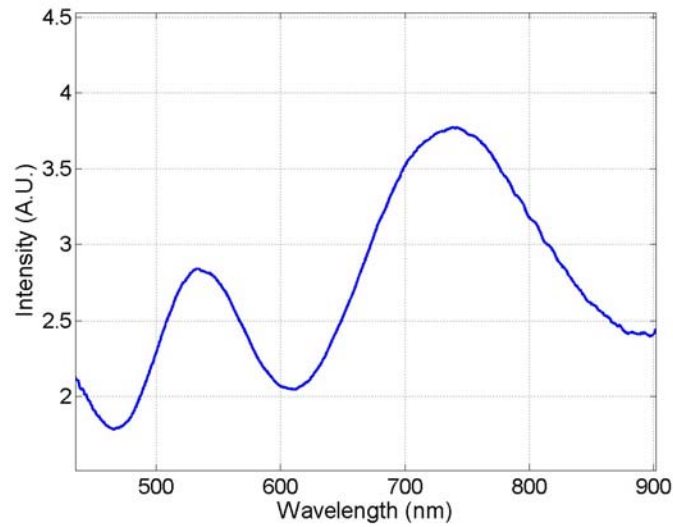


Figure 2-40: Fringes of the ZrO₂ wafer sample after 1500 °C annealing

Figure 2-40 clearly shows the ZrO₂ wafer sample after the 1500 °C annealing had very nice fringes. From this we can reasonably conjecture that the ZrO₂ thin film can potentially work up to 1500 °C, which is a good improvement to the Ta₂O₅ and the TiO₂ film sensors discussed previously, in terms of the maximal working temperature.

In order to further analyze the material property of the deposited ZrO₂ thin film on the sapphire targets, X-ray Diffraction (XRD) was used to measure the crystal orientation of the ZrO₂ thin film. PW1107/PW1140 X'Pert Pro Multipurpose X-ray diffractometer (Philips, Netherlands) was used as the XRD tool to characterize the crystal orientation of the ZrO₂ thin film. Two samples from a same deposition run were tested by the X-ray diffractometer. The first sample was as-deposition while the second one had been annealed from 400 °C up to 1500 °C. XRD results are shown in the following plot.

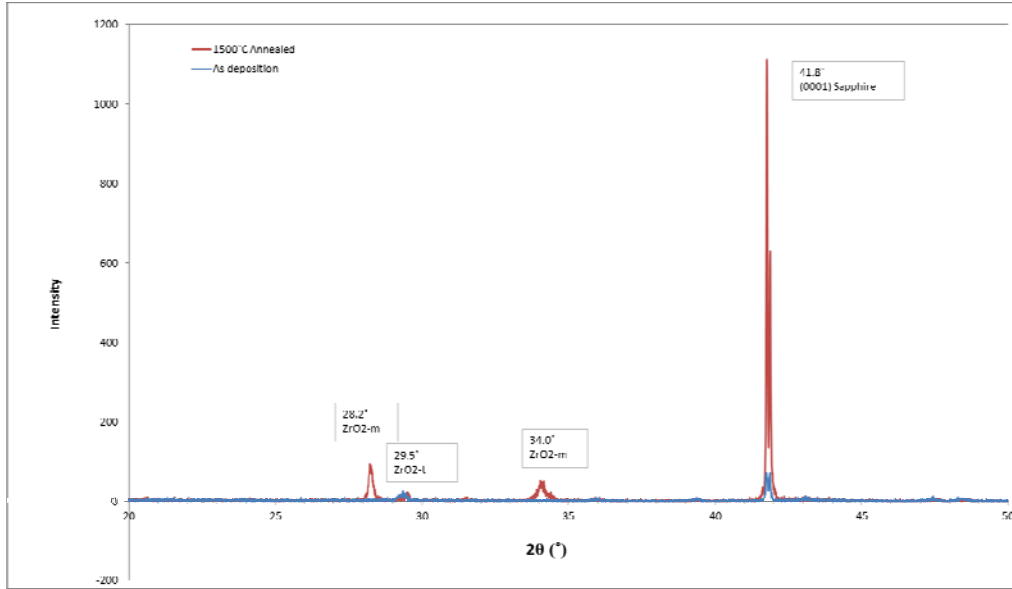


Figure 2-41: XRD result for the ZrO₂ thin film on sapphire wafer samples

It is seen from Figure 2-41 that for both samples there is a peak located at 41.8 °C. It corresponds to the sapphire wafer. The X-ray has a penetration depth of more than 1 μm thus the sapphire wafer is exposed to the X-ray inspection as well since the film thickness is less than 1 μm. The as-deposition sample was not found to possess any other major crystal orientation. That agrees with the common sense that the thin film deposited by PVD is generally amorphous. However, once annealed, the film started to crystallize. After annealed at 1500 °C, two major peaks were found with 2θ diffraction angles of 28.2° and 29.5 °, both referring to the monoclinic crystal structure.

The surface roughness of the ZrO₂ on the sapphire wafer samples was characterized using an Atomic Force Microscope (AFM, Veeco Nanoscope Dimension 3100). The two samples used in the aforementioned XRD experiments were then used for the AFM test. The surface contour of as-deposition sample is shown in Figure 2-42.

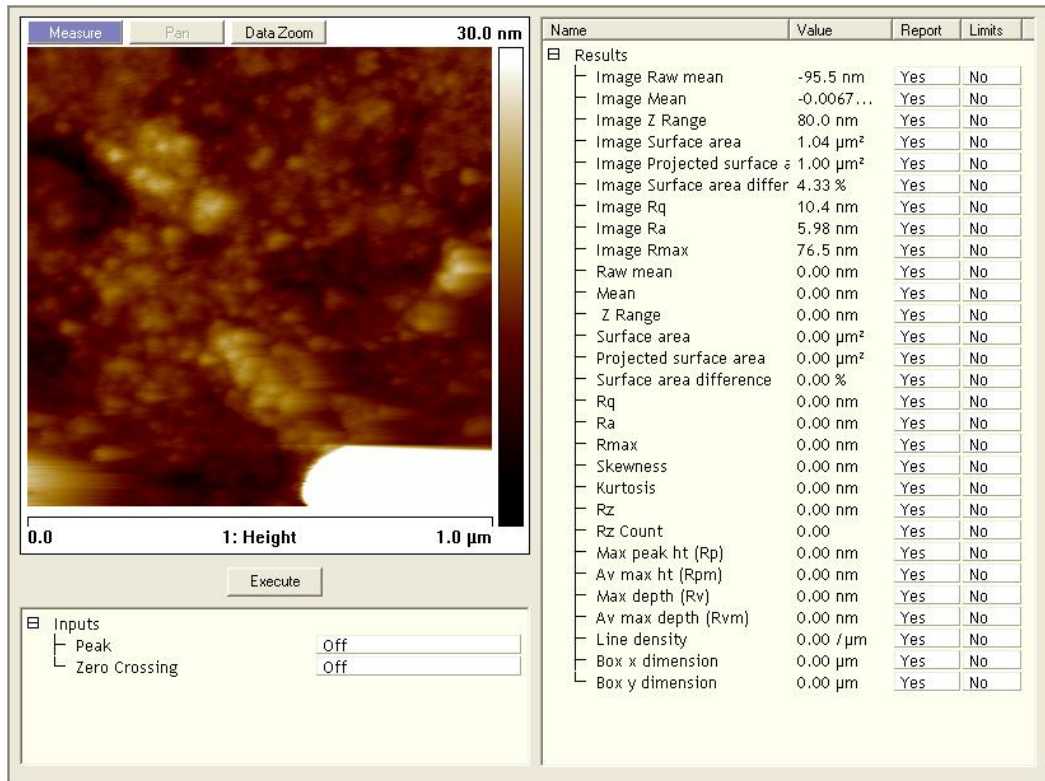


Figure 2-42: Surface contour of the as-deposition ZrO_2 thin film sample

A three dimensional map of the sample is shown in Figure 2-43.

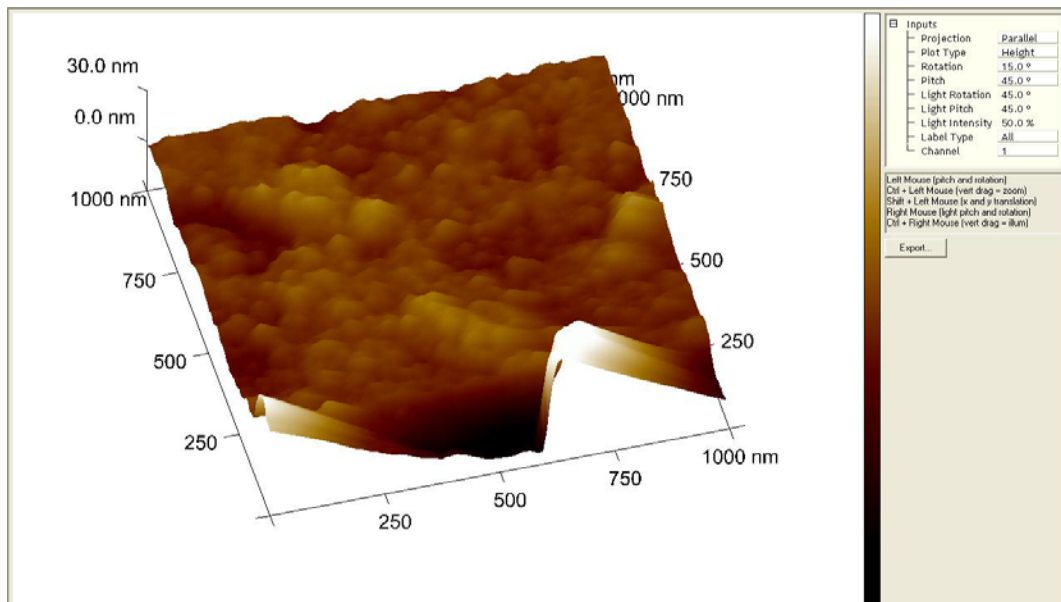


Figure 2-43: 3D map of the as-deposition ZrO_2 thin film sample

From the above plots we can tell that the as-deposition film is relatively smooth. The surface roughness calculated by the AFM software is 5.98 nm, as found in Figure 2-42. The corresponding plots for the 1500 °C annealed sample are shown in Figure 2-44 and Figure 2-45.

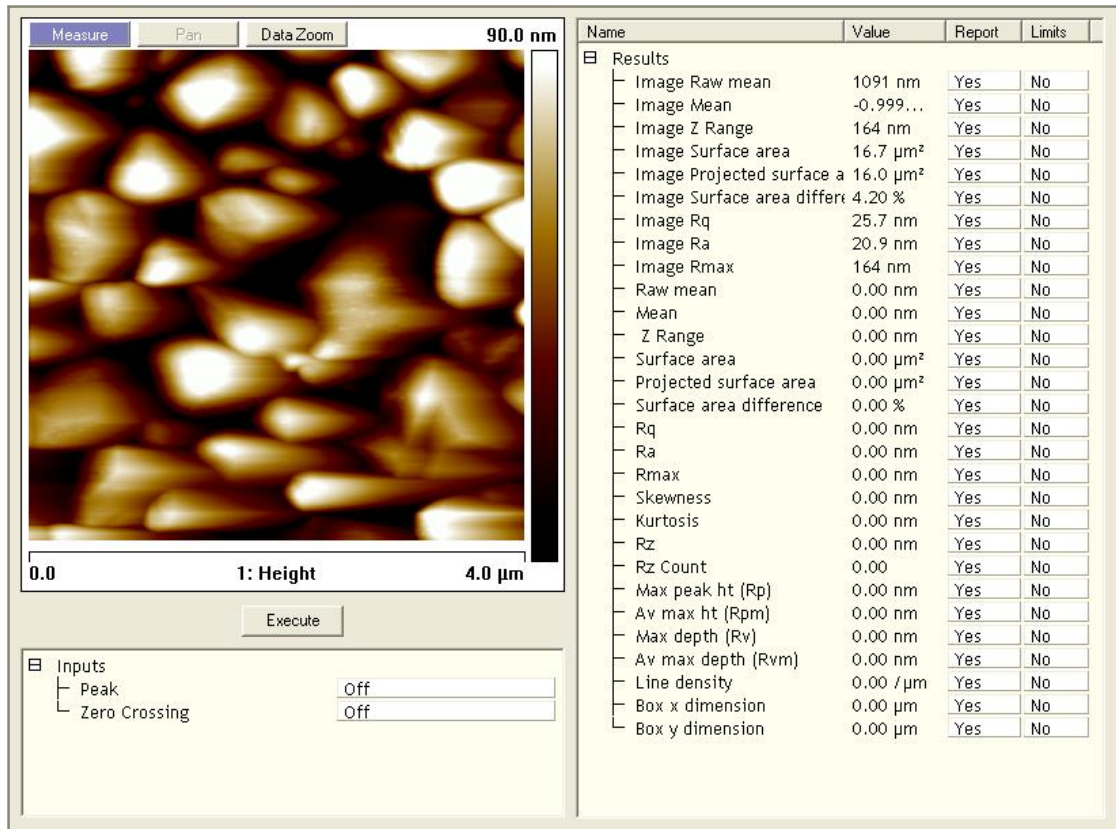


Figure 2-44: Surface contour of the annealed ZrO₂ thin film sample

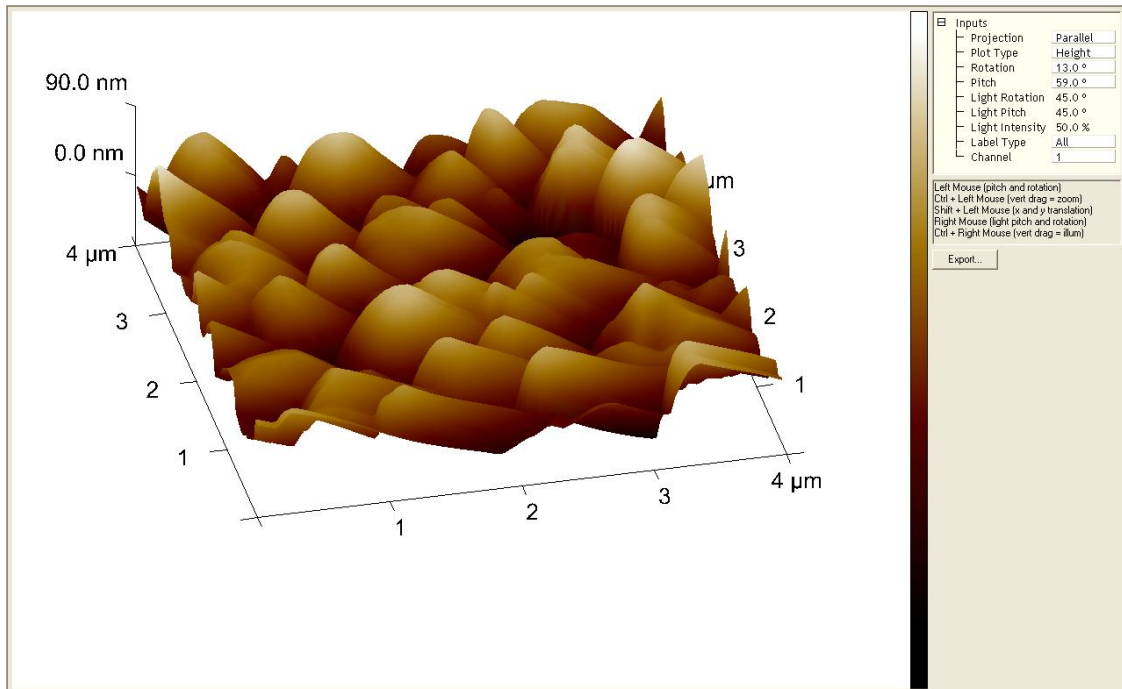


Figure 2-45: 3D map of the annealed ZrO₂ thin film sample

As can be seen from the plots, the surface roughness of the 1500 °C annealed sample is much worse than that of the as-deposition sample. The surface roughness for the 1500 °C annealed sample is calculated to be 20.9 nm. Since the optical light used to interrogate the film has a wavelength 20-40 times larger than the calculated surface roughness, we were still able to obtain clear fringes from the sample.

Based on the above results, it is concluded that the ZrO₂ thin film on the sapphire (C-Plane) maintains decent surface roughness even after annealed at 1500 °C. ZrO₂ thus is believed to be a good candidate material to fabricate thin film sensors that can work up to 1500 °C.

2.4.4.3 Testing and calibration

The ZrO₂ thin film fiber sensors were first annealed up to 1200 °C before calibrations were attempted from 100°C to 1000°C (both using the Thermolyne 48000 with a maximal temperature of 1200 °C). Spectra were recorded by the Type II spectrometer during the heating process and results are plotted in Figure 2-46.

From Figure 2-46, it is seen clearly that as the temperature increases, the spectrum shifts toward longer wavelength.

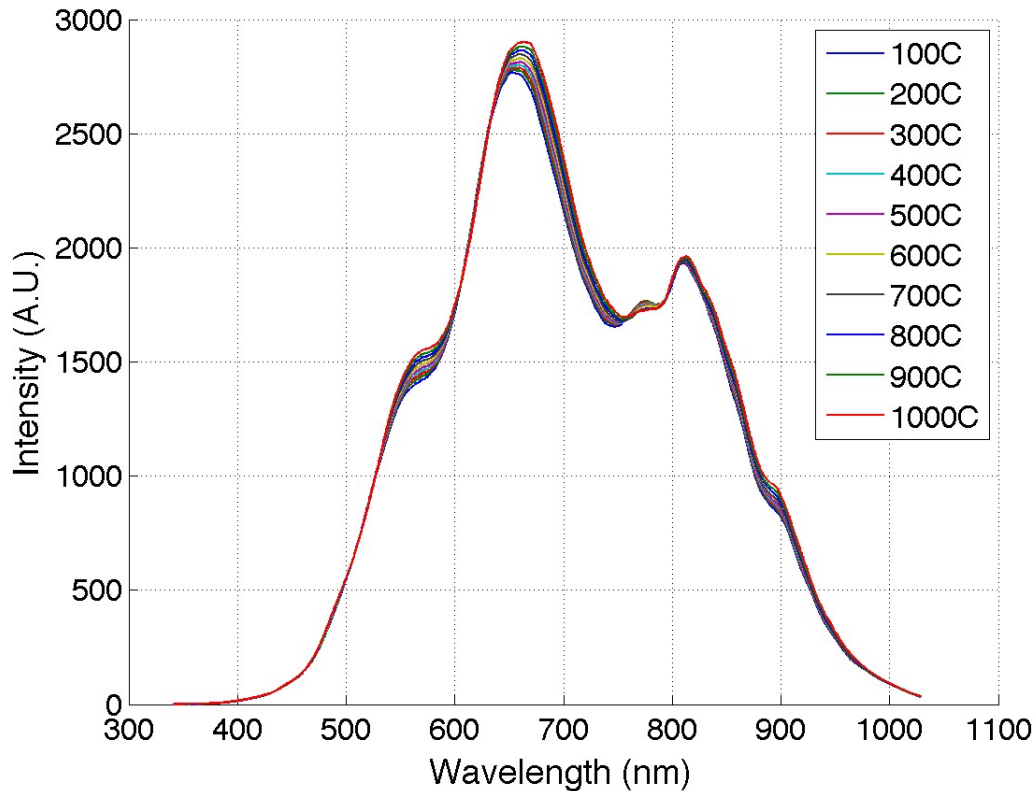


Figure 2-46: Averaged spectrum at each calibration temperature

In order to apply the curve-fitting algorithm, the measured spectra were first normalized using the background of the halogen light source measured prior to the calibrations. The normalized spectrum still suffers from the transmission spectrum $\beta(\lambda)$ as discussed in Equation 2-5. Figure 2-47 shows an avenue to mitigate this using curve fitting to find an approximation of the $\beta(\lambda)$. The blue line is a normalized spectrum whose intensity has a significant slope. In the presence of such a slope, it is difficult for the peak tracking method to find the central wavelengths reliably from the unsymmetrical peaks/valleys, thus additional inaccuracy is introduced to the sensor calibration. A green line in Figure 2-47 is a linearly fitted curve to represent $\beta(\lambda)$, using the peak intensities of the three peaks it intersects. Given the fitted $\beta(\lambda)$, the transmission spectrum can be almost

compensated. The compensated spectrum has much more symmetric peaks and valleys, as can be found in Figure 2-48.

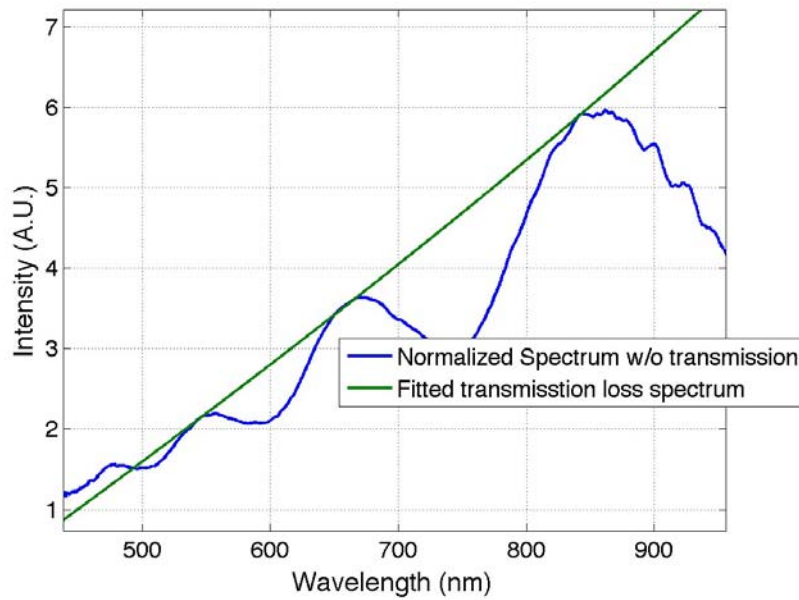


Figure 2-47: The transmission spectrum induced background

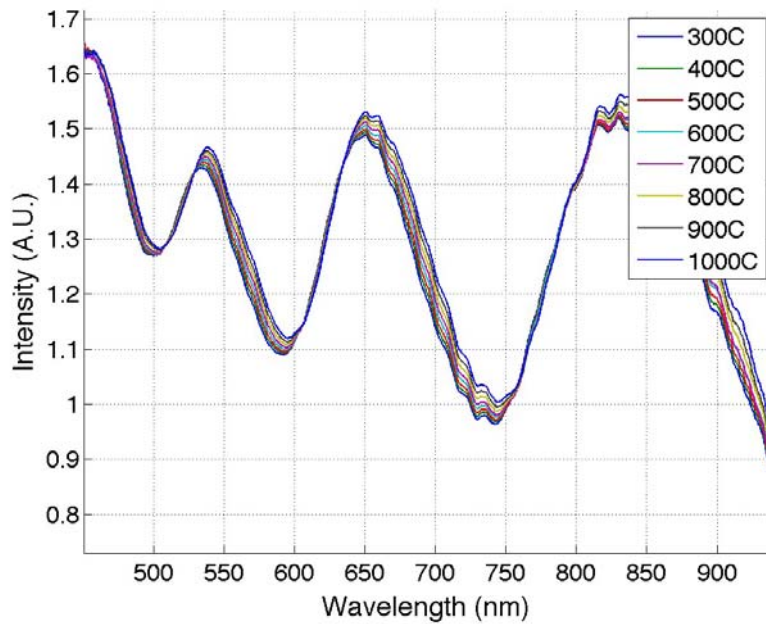


Figure 2-48: Transmission spectrum compensated sensor spectra

By far, we have obtained a compensated spectrum, which is close to the sensor's spectrum for calibration. Applying the peak-tracking method to the peak located around 650 nm, we can have the central peak wavelengths at different temperatures, as illustrated in Figure 2-49.

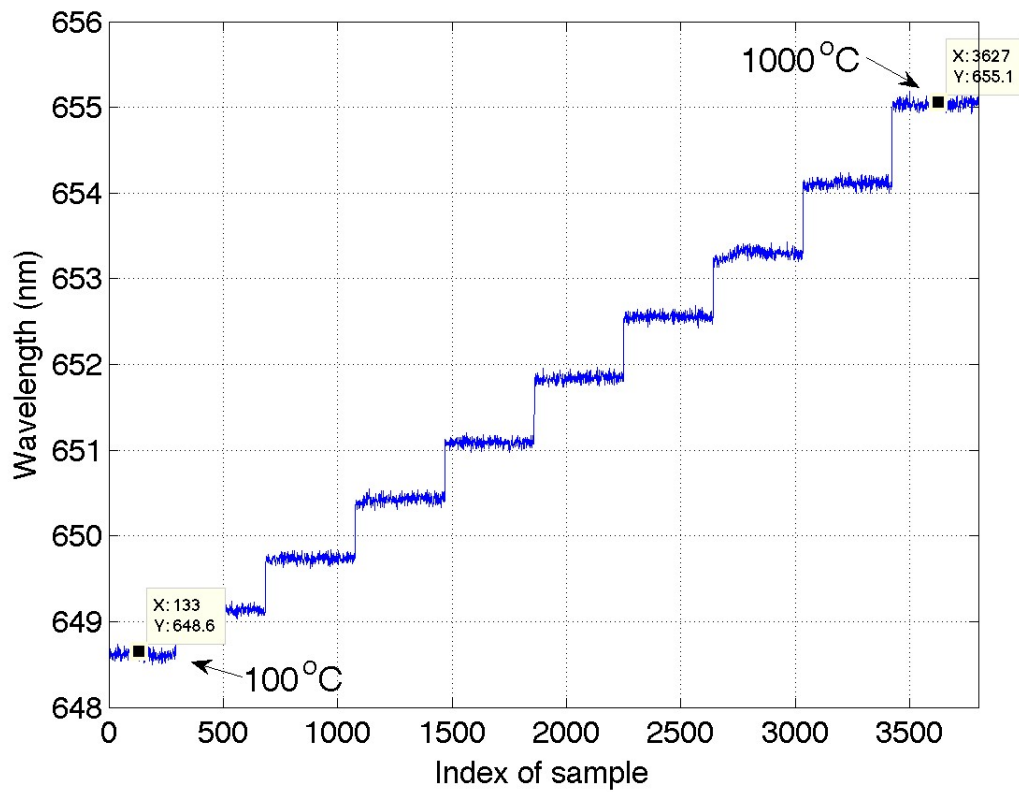


Figure 2-49: Central peak wavelength vs. temperature for the ZrO₂ thin film sensor

Based on the above results, the following calibration curve is obtained.

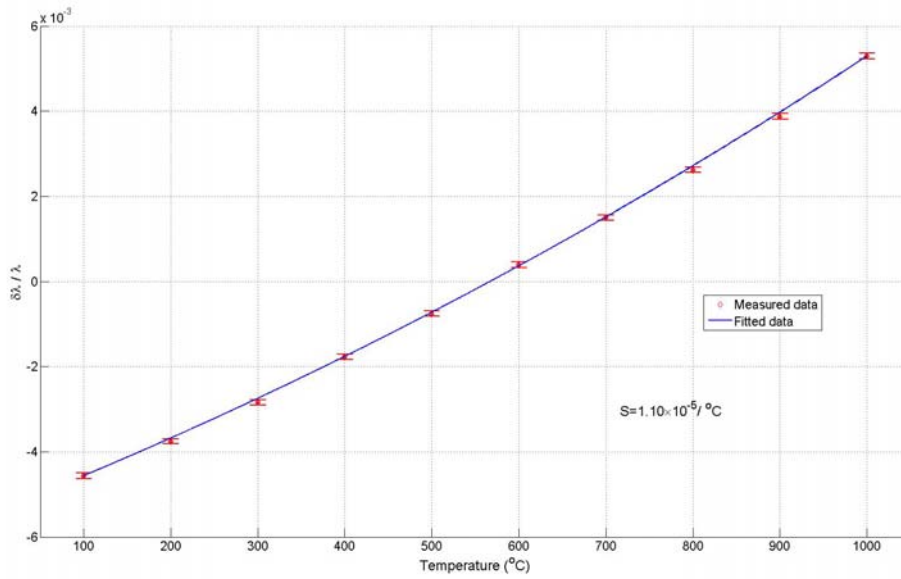


Figure 2-50: Calibration curve for the ZrO₂ thin film sensor

The sensitivity of the normalized wavelength shift for the ZrO₂ thin film fiber sensor is found to be about $1.10 \times 10^{-5} / ^\circ\text{C}$. The temperature resolution for the fiber sensor is defined by the largest standard deviation of the central peak wavelengths at any stable temperature over the sensitivity shown in Figure 2-50. The largest standard deviation of central peak wavelengths was measured at 1000 °C, whose fluctuation is shown in Figure 2-51.

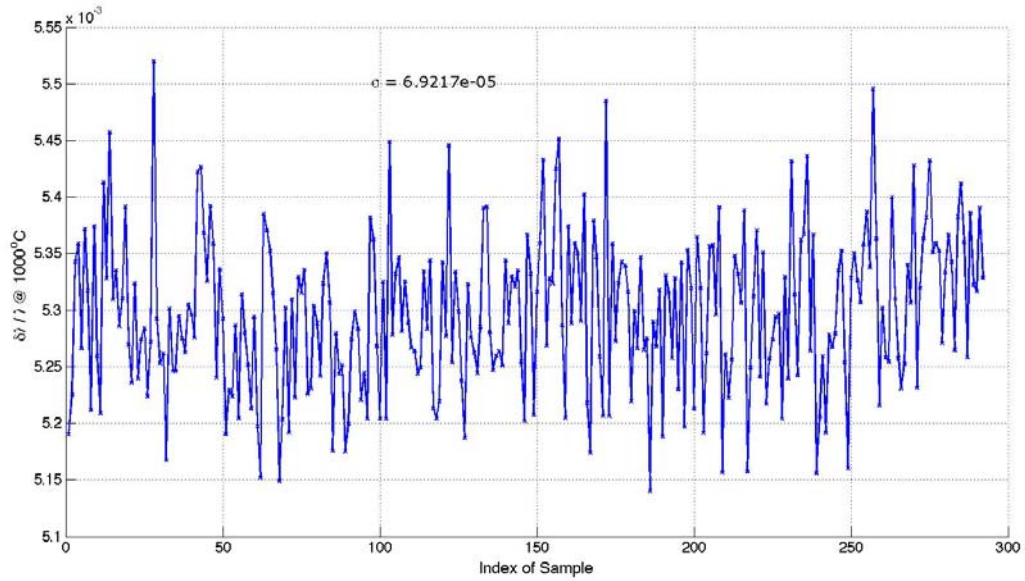


Figure 2-51: Fluctuation of the central peak wavelengths measured at 1000 °C

The standard deviation of the central peak wavelengths is calculated to be 6.92×10^{-5} , which corresponds to 6.3 °C according to the aforementioned sensitivity.

$$R_T = \frac{2\sigma}{S} = \frac{2 \times 6.92 \times 10^{-5}}{1.10 \times 10^{-6}} \text{ } ^\circ\text{C} = 12.6^\circ\text{C} \quad \text{Equation 2-16}$$

The above temperature resolution (2σ) shall be acceptable for most high temperature applications. This can be further improved by using a spectrometer with higher wavelength resolution or a light source with a higher fiber-coupled power density.

2.4.5 Summary of the thin film sensors

As a summary, miniaturized temperature sensors by a thin film coating on the top of the sapphire fiber have been demonstrated experimentally. PVD was used to study Ta_2O_5 , TiO_2 and ZrO_2 as the thin film material during the course of this work. Ta_2O_5 was studied first due to the ease of deposition; TiO_2 was studied thereafter to attempt sensors with higher working temperature range because TiO_2 has close CTE match to the sapphire's. However TiO_2 has a certain phase with sapphire named aluminum titanate beyond 1300 °C. The aluminum titanate has far different CTE to the sapphire's, thus TiO_2

is not suitable to fabricate thin film sensor to function at a temperature higher than 1300 °C. ZrO₂ was studied last since it not only has close CTE to the sapphire's, but also has complete separate phase with sapphire at temperature up to 1800 °C.

In experiment, each film material was coated on the tip of the sapphire fibers and tested using a furnace up to a temperature well beyond 1000 °C. Same film materials were also deposited on the sapphire wafers for thin film characterizations. Among these thin film sensors, ZrO₂ thin film based sapphire temperature sensors have been demonstrated to work up to 1200 °C in lab. Also given the results we have obtained from the sapphire wafer samples, we believe the ZrO₂ thin film based sapphire temperature sensors have a potential to work up to 1500 °C. Provided with the current technology on the spectrometer and the broad-band light source, the thin film sensors have a 2σ temperature resolution of 12.6 °C, which shall meet the requirement from most high temperature sensing applications.

Chapter 3 Multiplexed sensing system by frequency-multiplexing

To achieve multiplexed sensing, each sensor must carry certain characteristic that distinguishes it from the rest. One intuitive way to realize multiplexed sensing is to make sensors with different OPDs. Air-gap sensor is one of the methods to do so conveniently because of the in-line structure and ease to control OPD of each sensor. Air-gap sensors are widely seen in single-mode fiber sensors [73, 74] and have significant advantages of low cost, ease of fabrication and supreme flexibility in tuning of sensitivity and dynamic range. However, since the sapphire fiber is highly multi-moded, sapphire fiber based air-gap sensors with good fringe visibilities are typically very difficult to obtain, as pointed out by theoretical analyses by Wagner [75] and Han [76]. Previously in our lab, Xiao has attempted the sapphire air-gap sensor by carefully aligning two sapphire fibers on a ceramic plate [63], however the fringes are subject to external mechanical perturbations and stable performance is hard to maintain. In this work a new air-gap sensor structure and an improved fabrication technique to construct the sapphire air-gap sensors were studied and implemented. The sapphire air-gap sensors were fabricated by using two simultaneously polished sapphire fibers and a zirconia tube with tight tolerance for alignment. With the improvement in sensor structure, it was demonstrated that sapphire air-gap sensors with good fringe visibility could be readily obtained. Even more, with three cascaded sensors in a single sapphire fiber link, multi-point sapphire fiber sensing is reported for the first time. Since each sensor has interferometric fringes with different frequencies, this type of multiplexing method is called *frequency-multiplexing*.

In this Chapter, sensing principle of a single point air-gap sensor is discussed in section 3.1. A multiplexed sensing system consisted of three such air-gap sensors is described next in section 3.2. Finally, section 3.3 gives the detailed experimental results from the three-sensor multiplexed sensing system.

3.1 Sensing principle

Configuration of a single point sapphire air-gap temperature sensor is shown in Figure 3-1.

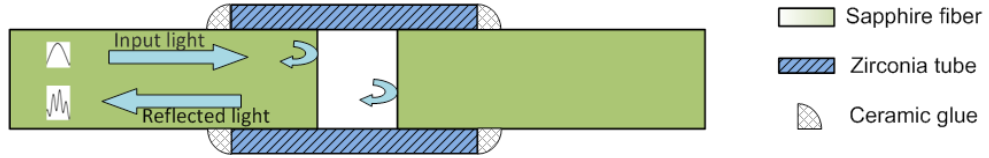


Figure 3-1: Configuration of a single point air-gap based sapphire temperature sensor

Two sapphire fibers (O.D. 75 μm) are first polished at the same time to obtain best surface parallelism, and then precisely aligned in a zirconia tube (I.D. 78 μm) to form an air-gap Fabry-Perot cavity that produces interferometric fringes in the reflection spectrum, as indicated by Equation 3-1.

$$I(\lambda) = I_1(\lambda) + I_2(\lambda) + \sqrt{I_1(\lambda)I_2(\lambda)} \cos\left(\frac{2\pi OPD}{\lambda} + \varphi_0\right) \quad \text{Equation 3-1}$$

$I_1(\lambda)$ is the reflection from the end of the first sapphire fiber while $I_2(\lambda)$ is that from the end of the second sapphire fiber. OPD of the sensor is determined by the physical separation of the two sapphire fibers and φ_0 is a phase delay owing to the propagation of the Gaussian-shaped light in the air-gap region. During polishing, an alumina tube whose I. D. is about 239 μm was used to hold four sapphire fibers at a same time and the maximum angle deviation is estimated to be 0.1° [77].

When a white light source is used to interrogate the sensor, reflected light would see periodic fringes in the reflection spectrum, as shown in Figure 3-2. The period of the fringes is solely decided by the OPD of the sensor, and is temperature dependent.

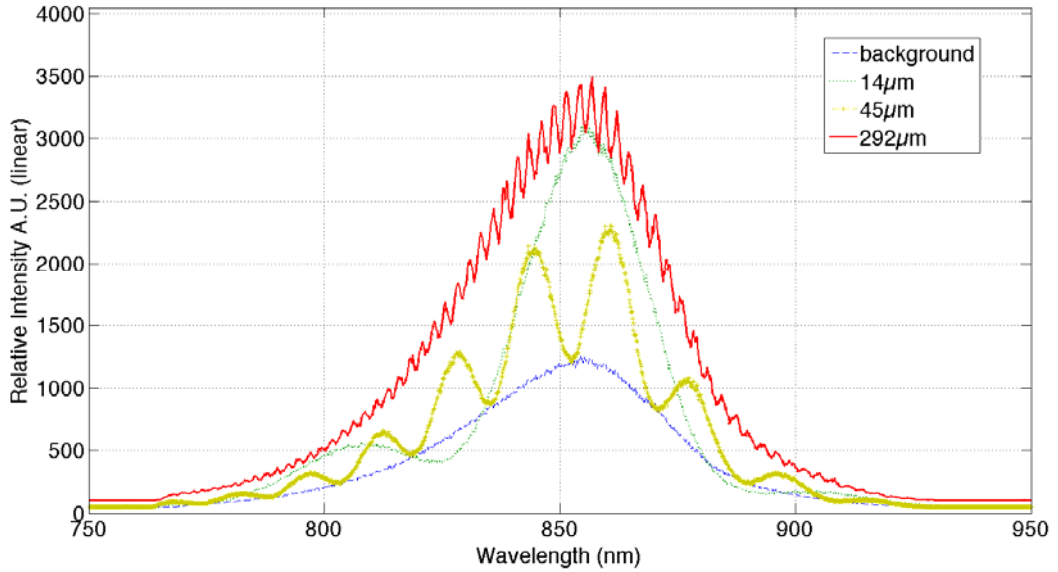


Figure 3-2: Reflection spectra of air-gap sensors with different OPDs

As seen in Figure 3-2, the larger the OPD is, the more peaks and valleys a spectrum has in the same wavelength range. Therefore analyzing the frequency of the fringes is the key to back out the temperature dependent OPD from the measured reflection spectrum. Previously in the thin film sensors, we used the peak-tracking method to find the change in spectrum due to temperature variations. In that case, the typical OPD is in the order of 2 μm . In this case of air-gap sensors, the OPD is generally much larger ($\sim 100 \mu\text{m}$) and the peak-tracking method has a poor resolution for such large OPD value. A separate signal demodulation algorithm will be used for the air-gap sensors.

Once a sensor with good fringe visibility had been aligned, high temperature ceramic glue (Cotronics HP903) was applied to bond the sapphire fibers to the zirconia tube permanently. As temperature changes, OPD of the sensor would change, as is determined by the differential thermal expansion in Equation 3-2.

$$\Delta OPD = OPD(T) - OPD(T_0) = 2 \int_{T_0}^T L_{eff} \{C_z(t) - C_s(t)\} dt \quad \text{Equation 3-2}$$

where $OPD(T)$ is the OPD at an arbitrary temperature T and $OPD(T_0)$ is that at a known temperature T_0 ; C_z and C_s are the thermal expansion coefficients of the zirconia tube and the sapphire fiber, respectively; and L_{eff} is the effective length of the air-gap sensor between the two bonding points where the ceramic glue is applied.

After fabrication, calibration was carried out by measuring the OPD of the sensor at different temperatures. Afterwards, when the sensor is used at an unknown temperature, OPD is calculated from the measured interferometric signal using the signal demodulation algorithm described in Ref. [66] and then temperature can be calculated from the calibration curve.

3.2 Frequency-multiplexing sensing system

3.2.1 Optical interrogation system

The optical system for the multiplexed high temperature sensing is shown in Figure 3-3. Multiple sapphire air-gap sensors are arranged in series along a single sapphire fiber link while the lead-in sapphire fiber is further spliced to a multi-mode silica fiber [65]. Optical light from a superluminescent light emitting diodes (SLED) (Honeywell) passes through the 50:50 multi-mode fiber coupler (Gould Optics) and is reflected by each of the sensors down the sapphire fiber link. The reflected light passes the coupler again and reaches the spectrometer (Ocean Optics USB2000) for spectral measurement. Index-matching oil is applied to the idle arm of the multi-mode fiber coupler to eliminate undesired reflection.

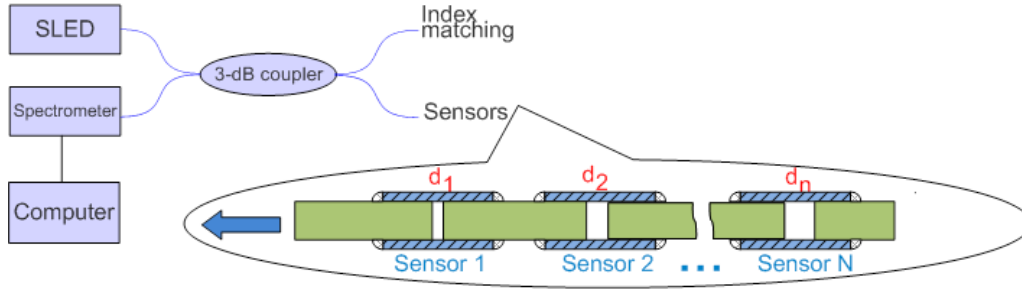


Figure 3-3: Optical interrogation system for the multiplexed sensing system

Since each sensor has a reflected spectrum as described by Equation 3-1, total spectrum reflected from the sensors can be expressed as

$$I_{total}(\lambda) = I_0(\lambda) + \sum_{j=1}^N \left\{ I_{j,1}(\lambda) + I_{j,2}(\lambda) + \sqrt{I_{j,1}(\lambda)I_{j,2}(\lambda)} \cos\left(\frac{2\pi OPD_j}{\lambda} + \phi_j\right) \right\}$$

Equation 3-3

$I_0(\lambda)$ is summation of all the background reflections along the sensing link, such as the one from the silica-sapphire fiber splicing point. Total reflection spectrum, $I_{total}(\lambda)$, has a low-frequency background from the light source as well as high frequency interferometric fringes decided by each sensor's OPD. In the frequency-multiplexing system, each sensor must have unique OPD in order to be distinguished. Once a reflection spectrum is measured, Fourier transform of the spectrum is performed. Since sensors have their unique frequencies, they will show up at different frequencies in the Fourier transform result. Band-pass filters are used to select each individual sensor and then white-light demodulation algorithm is applied to calculate the OPD for the chosen sensor. At last, the calculated OPD is used to deduct the temperature around the sensor using calibration data obtained in prior.

In experiment, the SLED has a central wavelength of 850 nm and a full-width-half-maximum (FWHM) of 50 nm. The spectrometer used here is the Type I spectrometer in Table 2-1. To demonstrate the multiplexing sensing system, we have three air-gap based

sensors fabricated along a single sapphire fiber link and then spliced to the 3-dB fiber coupler shown in Figure 3-3.

3.2.2 Sensor fabrication

The sensing link was fabricated based on a temporary-then-permanent bonding strategy. Since the air-gap sensors have to be significantly different in OPD, one bad sensor can ruin a whole sensing link. To reduce the risk in sensor fabrication, we first used a metal frame to align each individual sensor to the desired OPD before that particular sensor was temporarily bonded by wax, as shown in Figure 3-4.

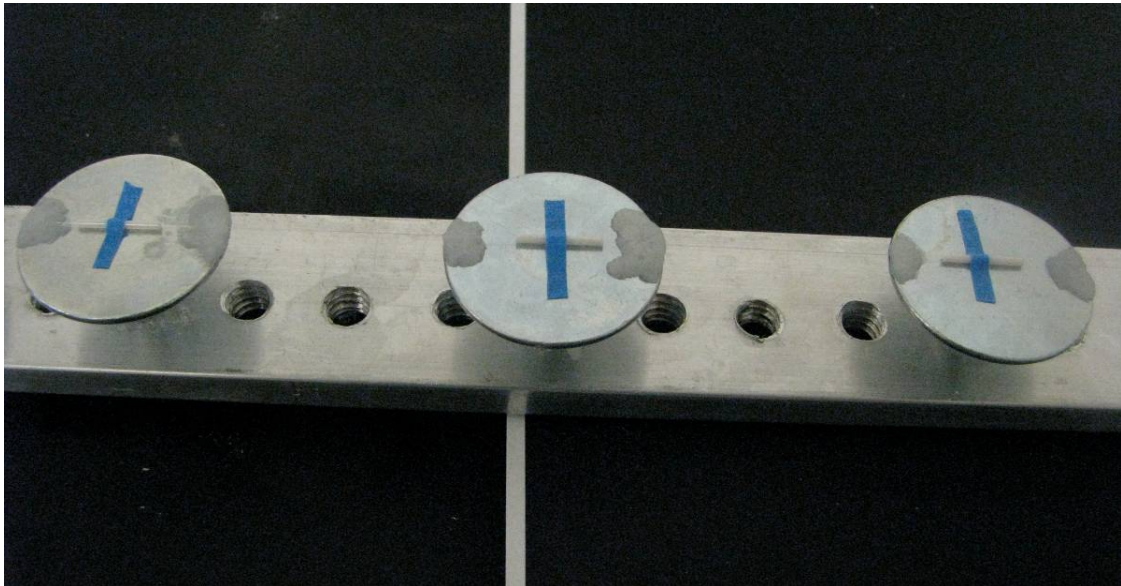


Figure 3-4: Metal frame for temporary sensor bonding

During the entire fabrication process, an automated computer program was used to monitor and calculate each sensor's OPD value in real time. The GUI of the program is offered in Figure 3-5. It is also seen from the figure that a sensing link with three sensors have been aligned at the time the picture was taken. The upper plot in the GUI shows the total measured reflection spectrum from all the three sensors and the lower plot shows FFT of the measured spectrum. Three peaks in the lower plot stand for three sensors with different OPD values.

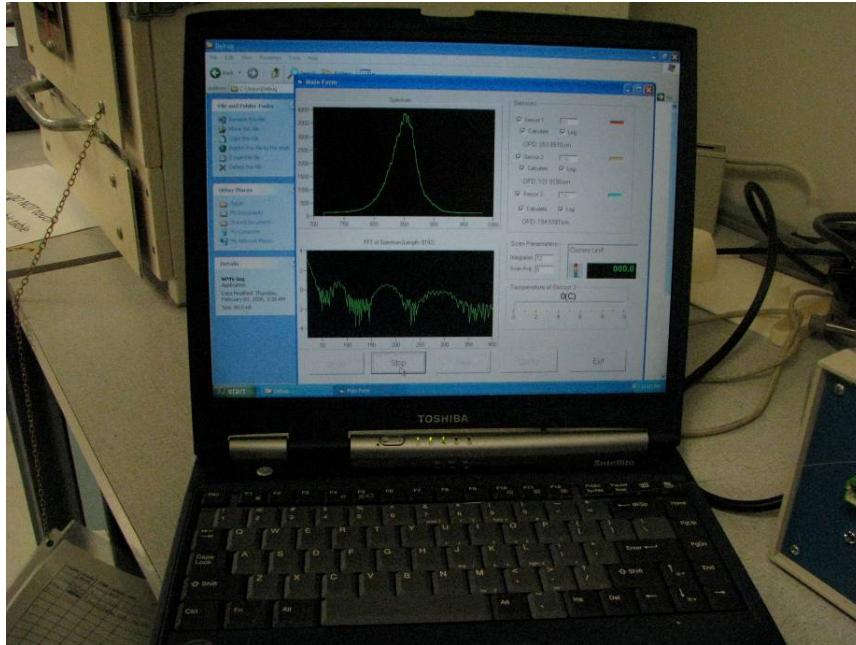


Figure 3-5: GUI of the computer program to aid sensor fabrication

If any sensor is not correctly fabricated, the wax can be cleaned and the process can go back to any prior step. After all desired sensors had been fabricated and temporarily bonded, the metal frame was taken to a CO₂ laser for permanent bonding. High temperature ceramic glue was applied on the bonding points illustrated in Figure 3-1. The CO₂ laser, as seen from Figure 3-6, was used cure the ceramic glue instantaneously to get a permanent bonded sensor. The CO₂ laser is used here because it is an excellent local heating source. The well-focused local heat from the laser beam can cure the ceramic glue without touching any low temperature bonding wax nearby. In experiment, the power from the CO₂ laser was controlled around 0.5 Watt and the diameter of the CO₂ laser was about 0.3 mm in diameter.

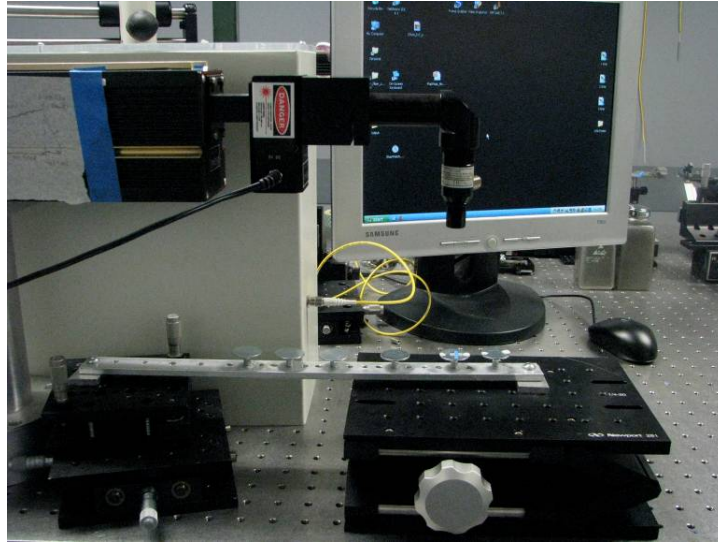


Figure 3-6: CO₂ laser for permanent sensor bonding

After having bonded all the sensors, the wax was cleaned off, leaving only a permanent bonded sensing link as presented in Figure 3-7.

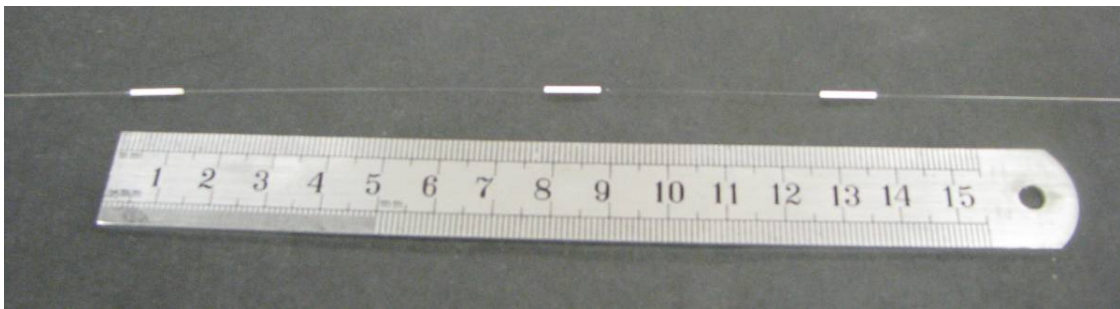


Figure 3-7: Picture of the three-sensor sapphire fiber sensing link

3.2.3 Measurement after fabrication

Using the white light signal demodulation algorithm, the OPDs of the three sensors at ambient temperature were measured to be approximately 95 μm , 145 μm and 47 μm , respectively. The spectra with and without the three sensors are illustrated in Figure 3-8 while the corresponding Fast-Fourier-Transform (FFT) results are plotted in Figure 3-9.

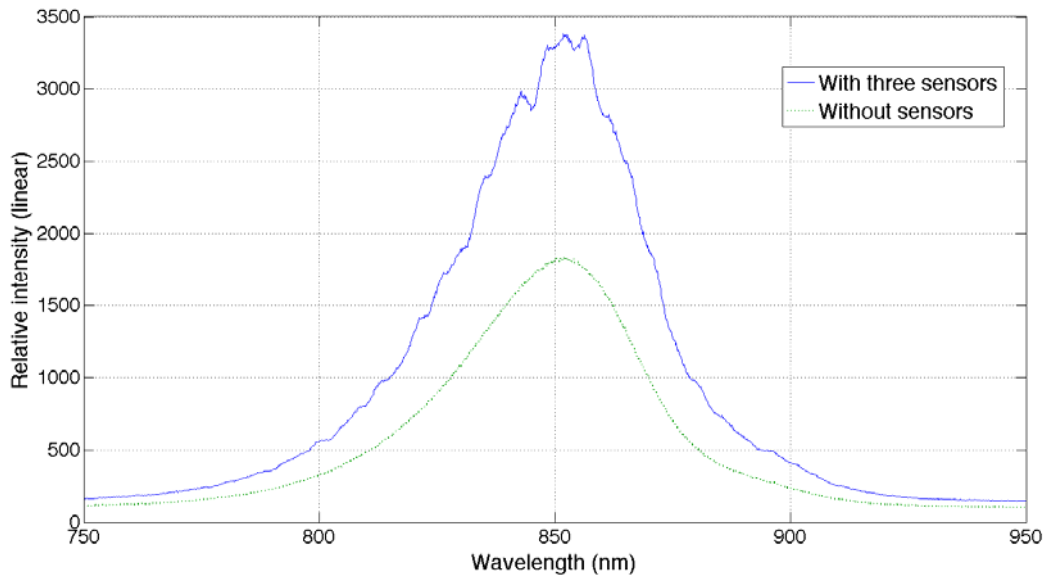


Figure 3-8: Reflection spectra of the three-sensor link

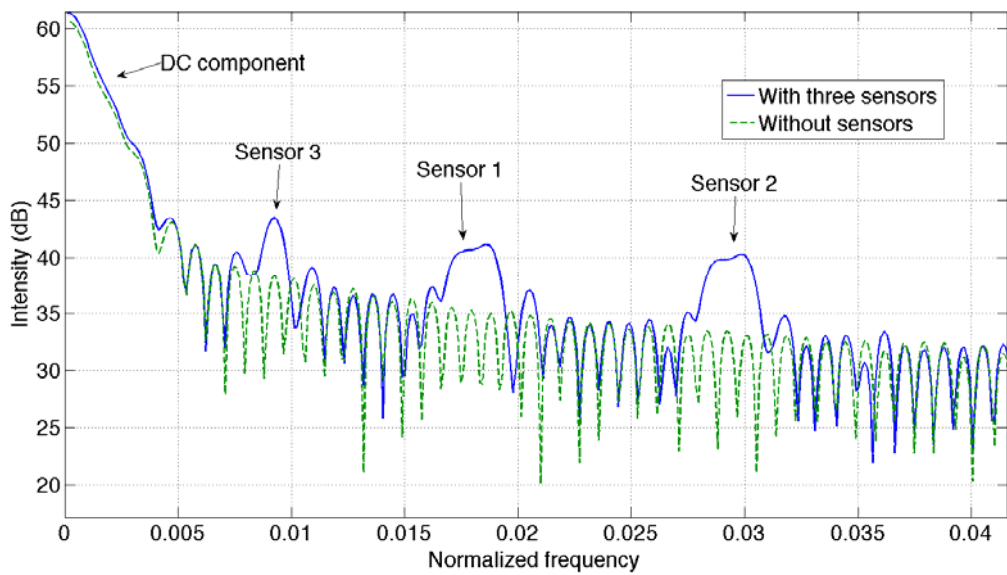


Figure 3-9: FFT result of the reflection spectra of the three-sensor link

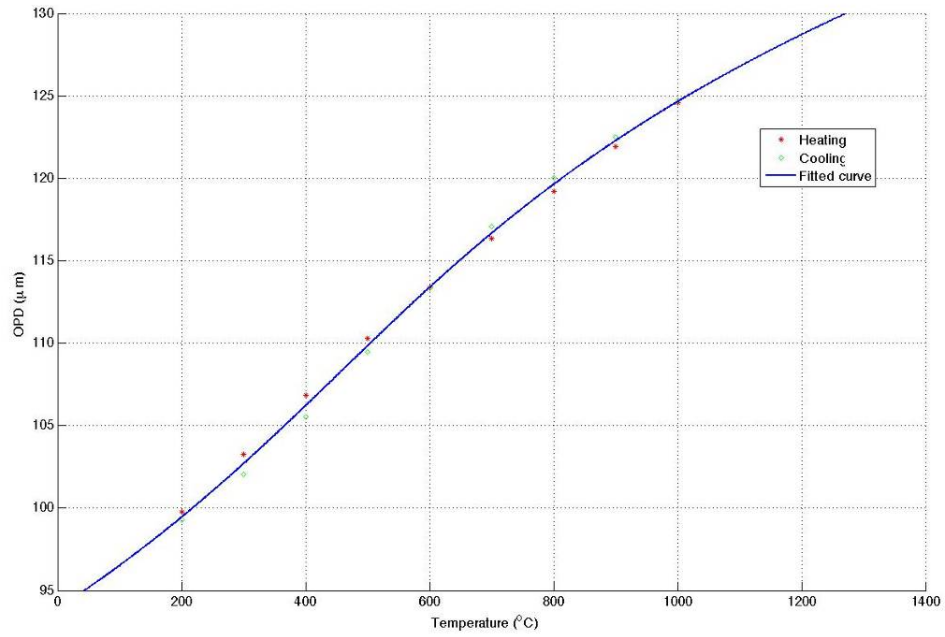
To demodulate the signal from each sensor, we performed FFT on the spectrum and created a band-pass filter to select one sensor at a time. Inverse FFT, phase unwrapping, and linear regression were then used to determine the OPD of the selected sensor.

Repeating this process with different band-pass filters, the OPDs of all the three sensors were estimated. Unlike the peak-tracking method [67], this signal demodulation algorithm uses the whole spectrum, instead of one peak or valley, to estimate the OPD and thus has very high accuracy for sensors with large OPD values. Details of this method are discussed in Ref. [66] and thus are not elaborated here.

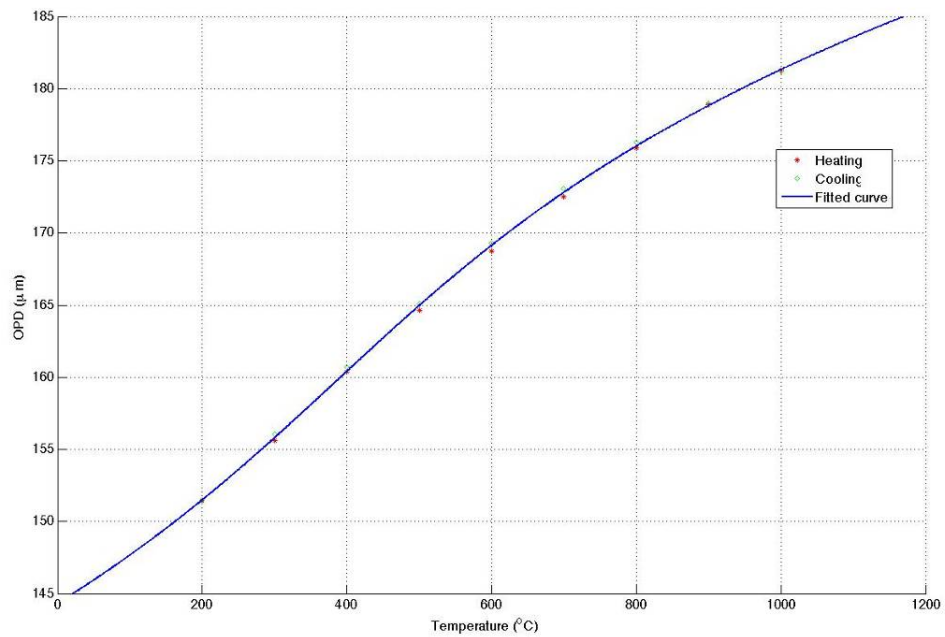
3.3 Calibration and analysis

3.3.1 Calibration

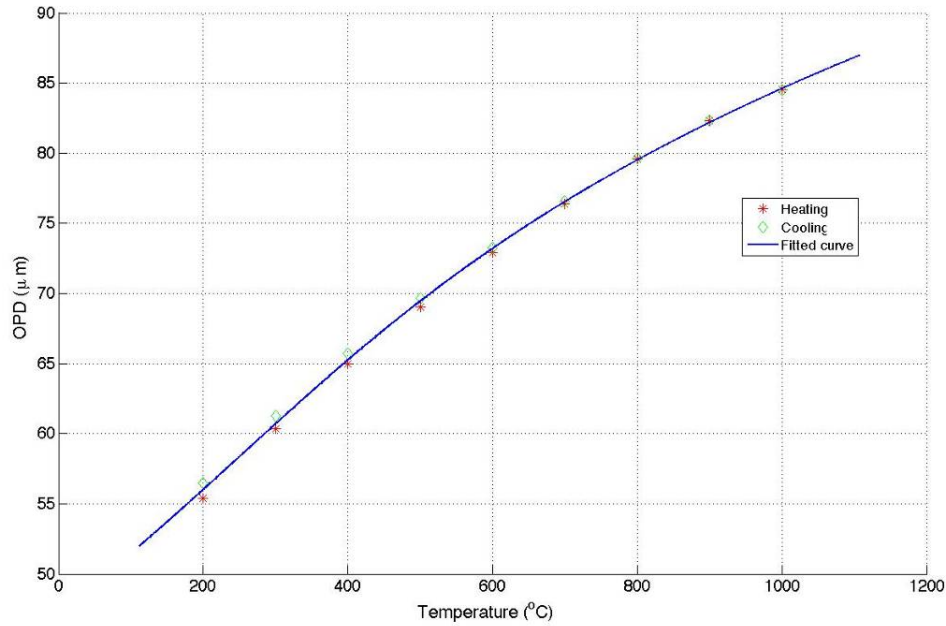
Before the calibration was attempted, the sensors were cycled from room temperature to 1150 °C for three times to fully cure the high temperature ceramic glue that was used to bond the sensors. The sensing link was then placed in a testing furnace (Thermolyne 48000) and a standard B-type thermal couple (Omega) was used to calibrate the sensors. During the calibration, the internal temperature of the furnace was programmed to rise from 200 °C to 1000 °C and then to drop to 200 °C, with a ramp rate of 3 °C/min. A developed software program was used to record sensors' OPD values during the entire calibration process. Figure 3-10 gives calibration curves for all the three sensors.



(a) Calibration curve of sensor 1



(b) Calibration curve of sensor 2



(c) Calibration curve for sensor 3

Figure 3-10: Calibration curves for the air-gap sensors

Hysteresis, observed as a difference between heating and cooling measurements from the sensor calibration in Figure 3-10, is mainly attributed to the effects of the ceramic glue used to bond the sensors.

3.3.2 Sensitivity

Figure 3-10 shows that the air gap sensors have very good sensitivity. From room temperature to 1000 °C, OPDs of the sensors increase at least 30 μm. Sensitivity decreases as temperature increases, due to smaller thermal expansion difference between the zirconia tube and the sapphire fiber at higher temperatures. The measured sensitivity around 1050 °C was still more than 20 nm/°C, much larger than that of a previously-reported wafer-based sapphire temperature sensor [62].

3.3.3 Consistency

Since the three sensors have different OPD values, in order to compare the calibration curves among sensors, each sensor's calibration curve was normalized to its

OPD value at 600 °C. The normalized calibration curves are then plotted together in Figure 3-11.

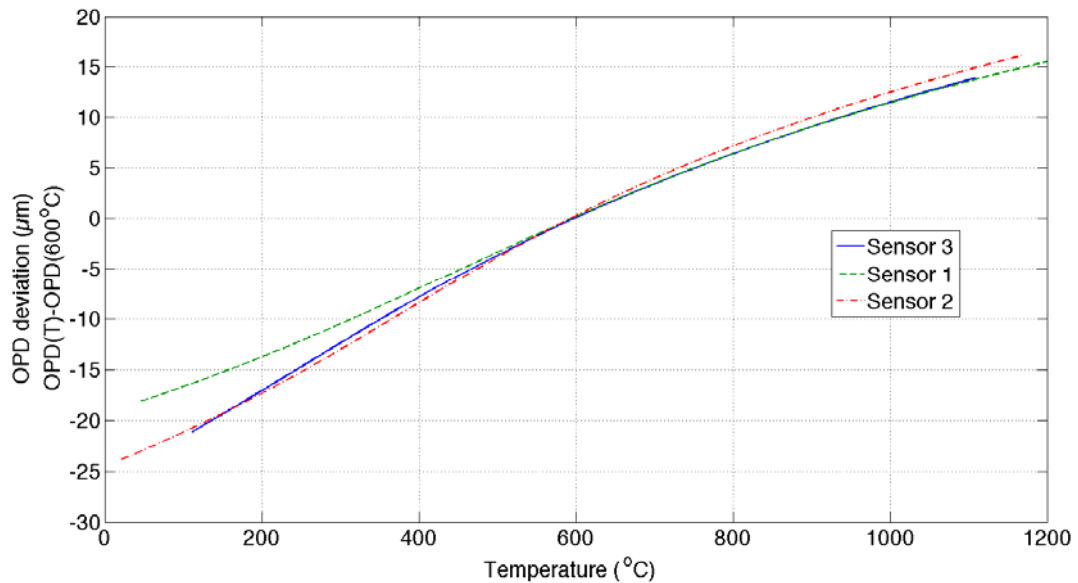


Figure 3-11: Normalized calibration curves for all the sensors

It is quite clear that all the sensors showed a similar calibration curve, which is theoretically governed by the differential thermal expansion between the zirconia tube and the sapphire fiber. The minor difference is due mainly to two factors. The first one is the difference in the effective sensor length L_{eff} , as given in Equation 3-2. The difference in the effective sensor length would change the effective sensitivity of the sensors. For example, Figure 3-11 shows sensor 2 has larger sensitivity than the other two sensors. That suggests that the sensor 2 may have a larger effective sensor length than the others do. The second factor is the temperature difference among the sensors when calibrating. During the calibration, all the sensors were loaded into the furnace, temperature reading from the furnace was taken as the temperature for all the three sensors. However, there was certain gradient inside the furnace that leads to a scaling effect of the calibration curve along the temperature axis, which also changes the sensitivity.

3.3.4 Temperature resolution

The inherent high sensitivity of the air gap sensors leads to a high temperature resolution. To demonstrate this, sensor 2 was tested at both ambient temperature and 1050 °C, each for 10 minutes. About 100 samples were obtained from each test and the deviations of the OPD readings from the mean values are plotted in Figure 3-12. The standard deviations were 2.8 nm, 2.9 nm for ambient temperature and 1050 °C, respectively. Given the sensor's sensitivity is around 20 nm/°C at 1050 °C, the temperature resolution is calculated to be 0.3 °C (2σ) at 1050 °C.

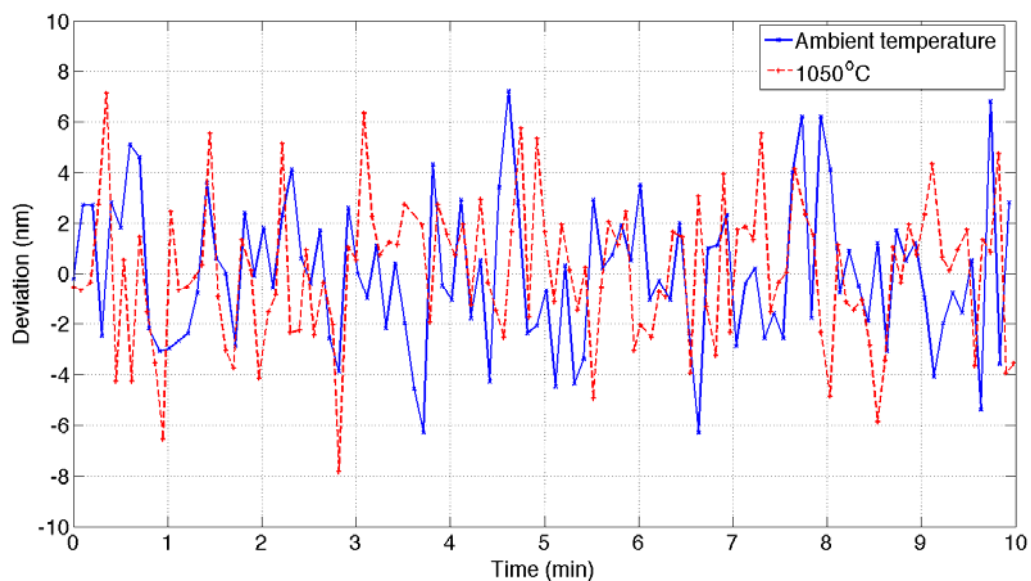


Figure 3-12: Fluctuation of the OPD output of sensor 2 at different temperatures

As a summary, we have demonstrated that the sapphire air-gap sensors can be readily fabricated by controlling the fiber parallelism and the clearance of the zirconia tube. Multiplexed air-gap sensors with different OPDs were fabricated into a single sapphire fiber link to demonstrate the feasibility of the multiplexed sapphire sensing. The multiplexed sensing system is a great improvement upon any single point sensing in some critical application where temperature profile is desired. The air-gap sensors also have high temperature sensitivity that may find separate applications to resolve very small temperature variation.

Chapter 4 Multiplexed sensing system by spatial-multiplexing

In the previous chapter, frequency-multiplexed sensing using sensors of different OPDs were introduced and good experimental results were shown. In the frequency-multiplexing system, each sensor must have unique OPD value in order to be discriminated by the demultiplexing system. Otherwise one sensor is entangled with other sensors and potential serious cross-talk would affect the system performance. In this chapter, a new multiplexing/demultiplexing system that allows each sensor having identical OPD value is studied. The new sensing system applies Optical Frequency Domain Reflectometry (OFDR) concept into the sapphire fiber sensing to accommodate and differentiate sensors with identical OPD value. Since the OFDR method uses the sensor location to differentiate the identical sensors, this method is named as *spatial-multiplexing*.

OFDR was firstly proposed in 1980s [78] to improve the capability of Optical Time Domain Reflectometry (OTDR). The basic concept is to continuously tune the wavelength of a laser while recording the reflected light from the Fiber Under Test (FUT). Compared with the OTDR, where wavelength of the laser is fixed, OFDR introduces additional freedom by tuning the wavelength of the laser. This extra freedom enables frequency-domain response measurement, in addition to the time-domain response measurement from the OTDR. Even more, the OFDR also features very high spatial resolution (up to tens of microns) in the time-domain measurement. In the past decade, the OFDR has been used in chromatic dispersion [79, 80] and polarization mode dispersion measurement [81, 82], optical components characterizations [83], optical network fault detection [84], and optical imaging [85]. OFDR technology is also reported for distributed sensing purposes [16]. While most of the work was done in single mode fiber, some is reported on multi-mode fibers [18, 86] in recent years.

In this chapter, OFDR for multiplexed high temperature sapphire sensing is studied. Identical sapphire wafer sensors with a same OPD value are fabricated into a sensing link. Advantages of the sapphire wafer in sensor fabrication and the OFDR in signal demodulation are taken to build an alternative sensing system that potentially has larger multiplexing capacity since the loss of the sapphire wafer sensors is smaller than that of the air-gap sensors.

4.1 Sensing principle

A schematic diagram of the OFDR sensing system is illustrated in Figure 4-1. Optical light from a tunable light source (TLS), whose wavelength is continuously tuned, is launched through an optical coupler into a reference reflection arm and a sensing arm that has all the sensors down the link. The reflected light, from both the reference arm and the sensing arm, passes through the coupler again and goes into a photodetector. The data from the photodetector are sampled into a computer for further analysis.

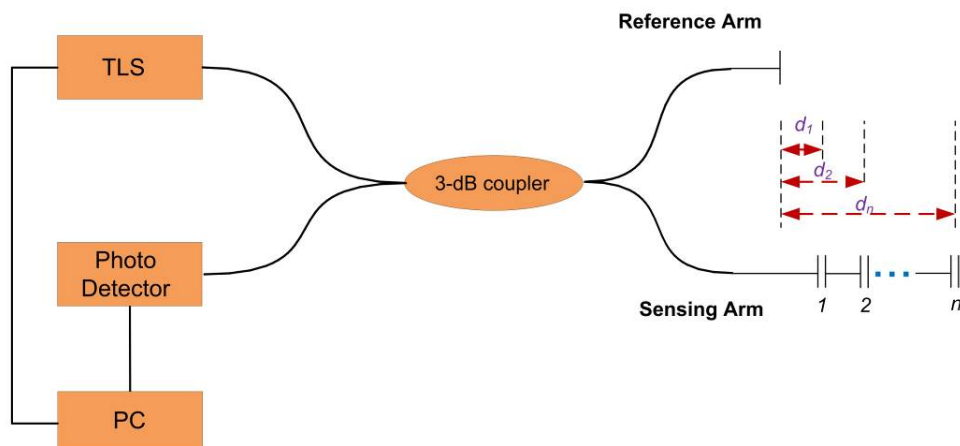


Figure 4-1: Diagram of the OFDR sensing system

First of all, we simply assume light from the TLS has enough coherent length to cover the span of all the sensors. Further for simplicity we assume each sensor is an identical sapphire wafer sensor. Reflection from each sensor in the sensing arm would interfere with that from the reference arm and those from other sensors. The total intensity of the optical light received by the photodetector can be expressed by,

$$I_t(\lambda) = |r_0 E_0(\lambda) \cos\left(\frac{2\pi ct}{\lambda} + \varphi_0\right) + \sum_{j=1}^n \left\{ r_{j,1} E_0(\lambda) \cos\left(\frac{2\pi ct}{\lambda} + \varphi_0 + \frac{4\pi n d_j}{\lambda} + \pi\right) + r_{j,2} E_0(\lambda) \cos\left(\frac{2\pi ct}{\lambda} + \varphi_0 + \frac{4\pi n d_j + 2\pi OPD_j}{\lambda}\right) \right\}|^2$$

Equation 4-1

where $I_t(\lambda)$ is the total intensity of the light detected at a given wavelength λ ; $E_0(\lambda)$ is the intensity of the electric field from the tunable laser at that wavelength; r_0 is the reflection coefficient for the electric field at the reference arm while $r_{j,1}$ and $r_{j,2}$ are those at the two fibers ends forming the j^{th} sensor. It is also assumed that the reflection coefficients are independent of wavelength λ . d_j is the separation of j^{th} sensor to the reference reflection while the OPD_j is the OPD value of the j^{th} sensor; n is the reflective index of the fiber connecting the sensors.

Since each sensor has different physical separation from the reference reflection, the interference of each sensor and the reference reflection would have different frequencies. Performing FFT to the data from the photodetector, one can identify separate peaks corresponding to different sensors. From the FFT result one can calculate the exact separation of any particular sensor and the reference reflection. Using a band-pass filter to choose a particular sensor and then performing inverse Fast Fourier Transform (iFFT), one can recover spectrum from the selected sensor, even each sensor has identical OPD value.

For simplicity, the system with only one sensor is taken as the first example. Assume the two reflections from the sensor cavity are identical ($r_{j,1} = r_{j,2} = r$), Equation 4-1 is rewritten as,

$$I_t(\lambda) = I_{DC}(\lambda) + rr_0 |E_0(\lambda)|^2 \left\{ \underbrace{\cos\left(\frac{4\pi n d_j}{\lambda} + \pi\right)}_1 + \underbrace{\cos\left(\frac{4\pi n d_j + 2\pi OPD_j}{\lambda}\right)}_2 + \underbrace{\cos\left(\frac{2\pi OPD_j}{\lambda} - \pi\right)}_3 \right\}$$

Equation 4-2

Equation 4-2 shows the detector data have two components, a DC value and an AC value from the interference of the reflections. The AC value has three contributing components, as marked in Equation 4-2. The first one comes from the interference of the reference reflection and the first reflection from the sensor cavity; the second one comes from the interference of the reference reflection and the second reflection from the sensor cavity; the last one comes from the interference between the two reflections from the sensor cavity. In real applications, the sensors typically have an OPD value in the order of 100 μm and physical a separation d_j in the order of centimeters. So, it is a solid assumption to say $d_j \gg \text{OPD}_j$. Given this, it is obvious that the first and the second terms in the AC component have very close frequency, primarily governed by d_j .

The AC component of $I_t(\lambda)$ around the frequency governed by d_j is expressed by Equation 4-3.

$$\tilde{I}_t(\lambda) = rr_0 |E_0(\lambda)|^2 \left\{ \cos\left(\frac{4\pi nd_j}{\lambda} + \pi\right) + \cos\left(\frac{4\pi nd_j + 2\pi \text{OPD}_j}{\lambda}\right) \right\} \quad \text{Equation 4-3}$$

Using the trigonometric identity, Equation 4-3 can be rewritten as,

$$\begin{aligned} \tilde{I}_t(\lambda) &= 2rr_0 |E_0(\lambda)|^2 \cos\left(\frac{4\pi nd_j}{\lambda} + \frac{\pi \text{OPD}_j}{\lambda} + \frac{\pi}{2}\right) \cos\left(\frac{\pi}{2} - \frac{\pi \text{OPD}_j}{\lambda}\right) \\ &\approx 2rr_0 |E_0(\lambda)|^2 \cos\left(\frac{4\pi nd_j}{\lambda} + \frac{\pi}{2}\right) \sin\left(\frac{\pi \text{OPD}_j}{\lambda}\right) \end{aligned} \quad \text{Equation 4-4}$$

Equation 4-4 mathematically explains the principle of the OFDR. The sensor's OPD (OPD_j) is modulated to another frequency decided by the physical separation d_j . Even though each sensor has identical OPD down the sensing link, they will be modulated to different frequencies because the physical separation of each sensor to the reference reflection is different. It is also noticed that the *sin* term in Equation 4-4 has half the interferometric frequency of the sensor. To recover the original spectrum of the sensor, one must double the frequency of the signal. Certain signal processing technique must be used to achieve so.

For signal demodulation, the following steps are taken to recover the spectrum of each sensor,

- Perform FFT on the data from the photodetector, each sensor will show up at different central frequencies;
- Select a sensor to analyze, apply band-pass filter around its frequency to choose that particular sensor only;
- Take the square of the filtered signal from the last step, use a low-pass filter to get the envelope of the squared signal. Squaring is taken here because the sensor's OPD is cut half in frequency by modulation, as can be found by comparing Equation 4-4 to the third AC component in Equation 4-2. The squaring doubles the frequency back to what it shall be.

By performing the above procedures, spectrum of a sensor may be successfully recovered, as if only the sensor were connected to the optical system. Repeating the above process by selecting different sensors in step 2, we can have spectrum of each sensor and thus resolve changes in the spectra.

The interferences between sensors also need to be considered carefully. As the reference reflection can interfere with each sensor, the reflection from one sensor can also interfere with that from another sensor. The inter-sensor interferences have frequencies governed by the differential physical separation Δd_j , which may have similar frequency to the interference of the reflection from the sensor and the reference reflection. In experiment, to avoid the ghost signal from the inter-sensor interferences, the separation of each sensor has to be carefully arranged to position the frequencies of the inter-sensor interferences away from those of the reference reflection and the sensor reflection.

In order to further explain how this OFDR system works, an numeric simulation example where three sensors with almost identical OPD values are cascaded in a sensing link is offered to illustrate how to recovery each sensor's spectrum step-by-step. The example is set in a single mode fiber (SMF) case with three sapphire wafer sensors cascaded in the sensing arm whose OPD values are 200 μm , 200.1 μm , and 200.2 μm . Each wafer sensor

has two reflections from the air-sapphire interfaces. Separations of the three sensors to the reference arm are 8 cm, 9 cm and 10 cm, respectively. Wavelength from the tunable laser is linearly tuned from 1520 nm to 1570 nm. The OPD values are so close to each other that the frequency-multiplexing method as the one described in Chapter 3 is not able to differentiate them. However, the OFDR method is able to recover the spectrum for each individual sensor, as can be seen from the following steps.

When the wavelength is tuned, the photodetector data during a complete wavelength scan is plotted in Figure 4-2.

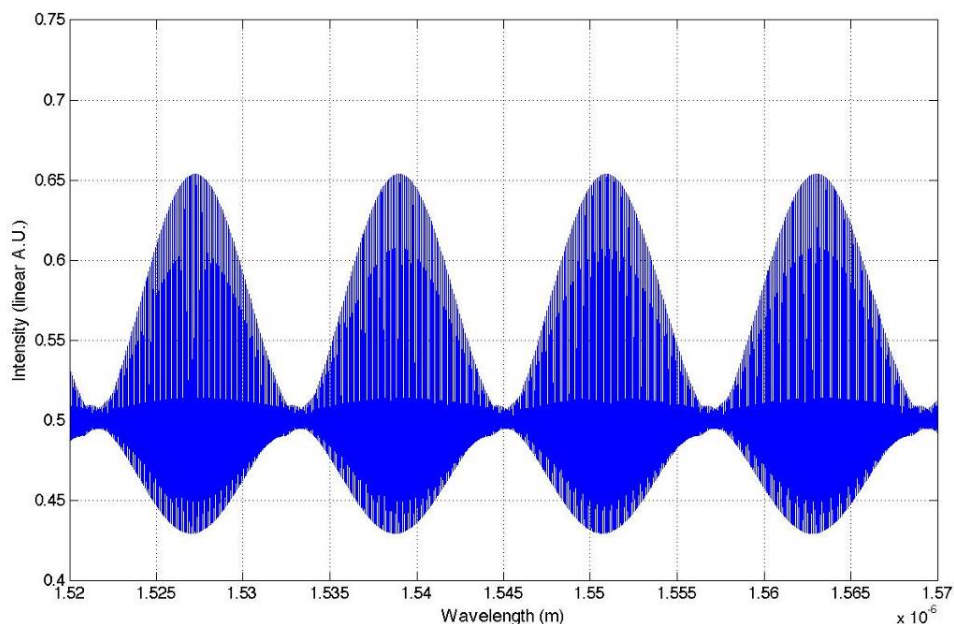


Figure 4-2: Photodetector readings during a wavelength scan

As can be seen from Figure 4-2, the photodetector data has an envelope that corresponds to the interference between adjacent reflections (two reflections from each sensor) and high frequency oscillations that are resulted from the interference between reflections that are far away, namely the interference between the reference reflection and each sensor's reflection, as well as the inter-sensor interferences. The next step is to convert the above data from the wavelength domain to the wave-number domain and perform FFT. The FFT results are shown in Figure 4-3.

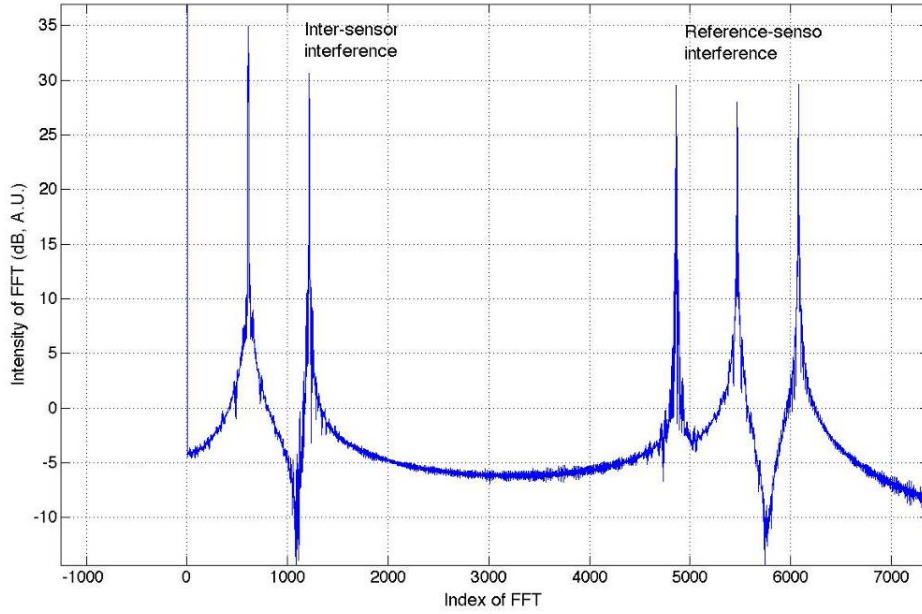


Figure 4-3: FFT result of the photodetector data

Since the data from the photodetector is recorded in the wavelength domain, FFT result of that is in the spatial domain. Thus the x-axis of Figure 4-3 can be converted into spatial length. As is pointed out in Ref. [16], each data point in the FFT result corresponds to a length increment of (spatial resolution),

$$L_{res} = \frac{\lambda_1 \lambda_2}{4n\Delta\lambda} \quad \text{Equation 4-5}$$

where λ_1 and λ_2 are the starting and the stopping wavelengths during a complete wavelength scan. n is the refractive index of the fiber and $\Delta\lambda$ is half of the scanning range. Plugging the numbers in this case into Equation 4-5, spatial resolution in the example is calculated to be

$$L_{res} = \frac{\lambda_1 \lambda_2}{4n\Delta\lambda} = \frac{1520 \times 1570}{4 \times 1.45 \times 25} \text{ nm} = 16.46 \mu\text{m} \quad \text{Equation 4-6}$$

Now Figure 4-3 can be reprinted as Figure 4-4, with the x-axis changed to the spatial length.

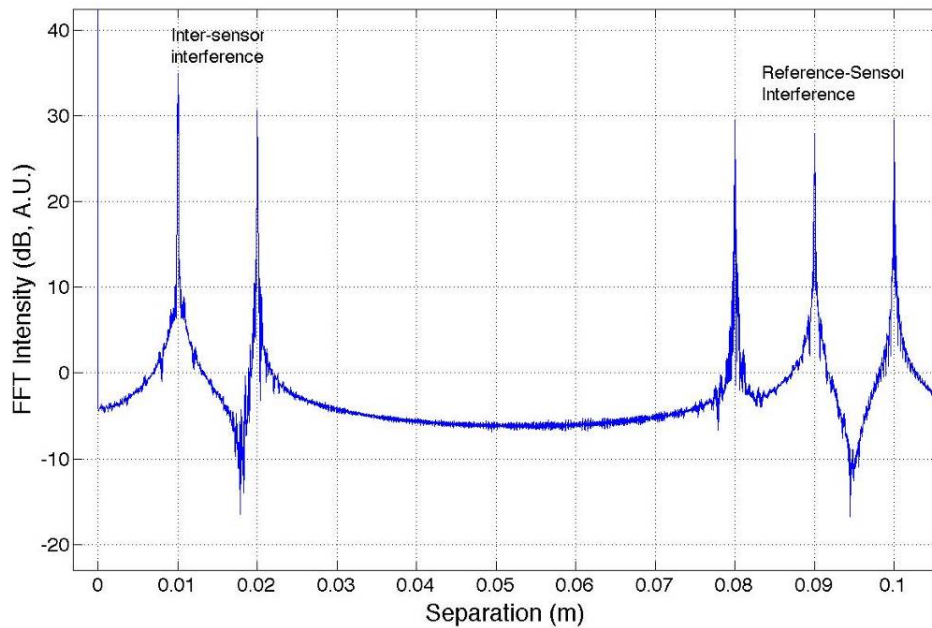


Figure 4-4: FFT result shown in spatial domain

From Figure 4-4, it is clearly found where the sensors locate in relevance to the reference reflection. Three peaks are located at 8 cm, 9 cm and 10 cm. Also the inter-sensor interferences are located at 1 cm and 2 cm. The numbers agree with the geometry separation described in prior to the data processing.

After the sensors are identified in the FFT results, a band-pass filter is used to select one sensor at a time and convert the filtered data back into the wavelength domain to recover the spectrum from that sensor. Figure 4-5 shows the recovered spectrum from the sensor that is located 8 cm from the reference reflection. As seen from Figure 4-5, the recovered spectrum (blue) has a nice sinusoidal curve whose frequency is the one from a real sensor (green). The spectrum on the longer wavelength edge suffers distortion, because of the digital filtering. Since the photodetector data are first converted into the wave-number domain and filtered by the band-pass filter. The digital filtering would unavoidably contaminate the first number of data points (the length of affected data points is dependent on the order of the filter as well as the filter type). The affected data points are small in wave-number and thus are large in wavelength, as shown in Figure 4-5. For

further data processing, the recovered spectrum can be truncated to avoid carrying error to later analysis. Also the recovered spectrum is seen to be somewhat shifted from where it is supposed to be. The shifting is also caused by the digital filtering process, because the filter would generate certain “phase” delay to the original signal. Once the central frequency, the filter type, and the order of the filter are decided, the shifting length can be calculated and then compensated.

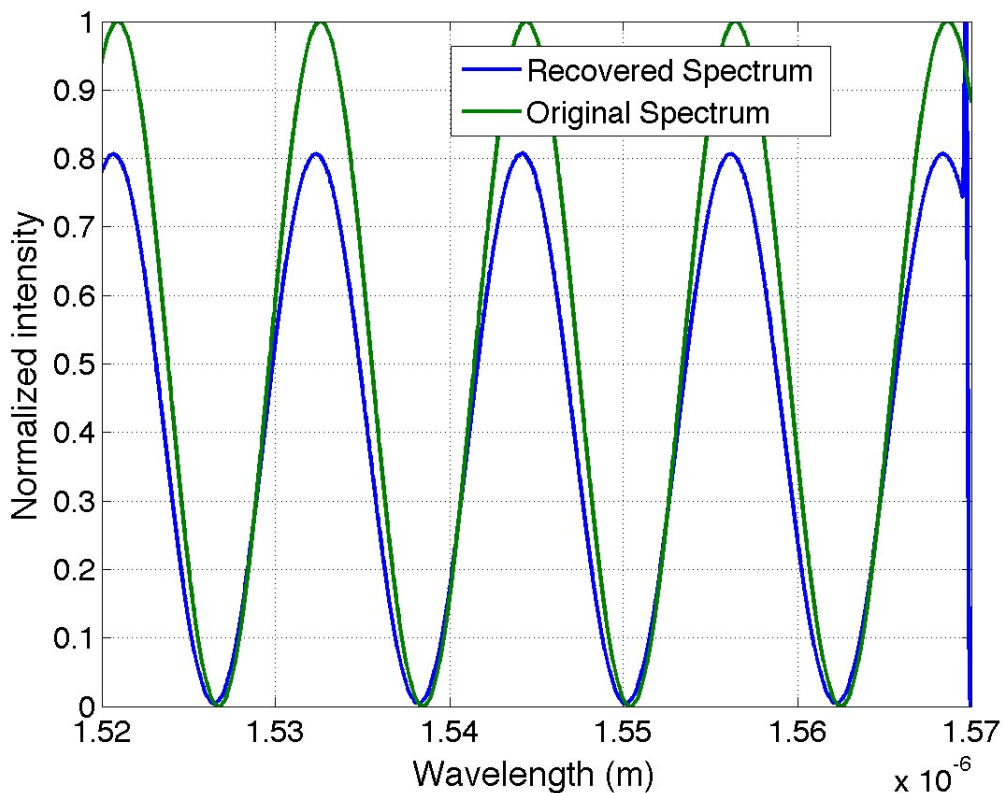


Figure 4-5: Recovered spectrum for one of the sensors

Repeating the above process for all the sensors, spectrum for each individual sensor can be recovered, as shown in Figure 4-6. The recovered spectrum of a sensor with larger OPD appears toward the longer wavelength. That agrees with theoretical predictions. Also it is pointed out that the spectra shown in Figure 4-6 have been truncated to eliminate the distortion in the long wavelength region.

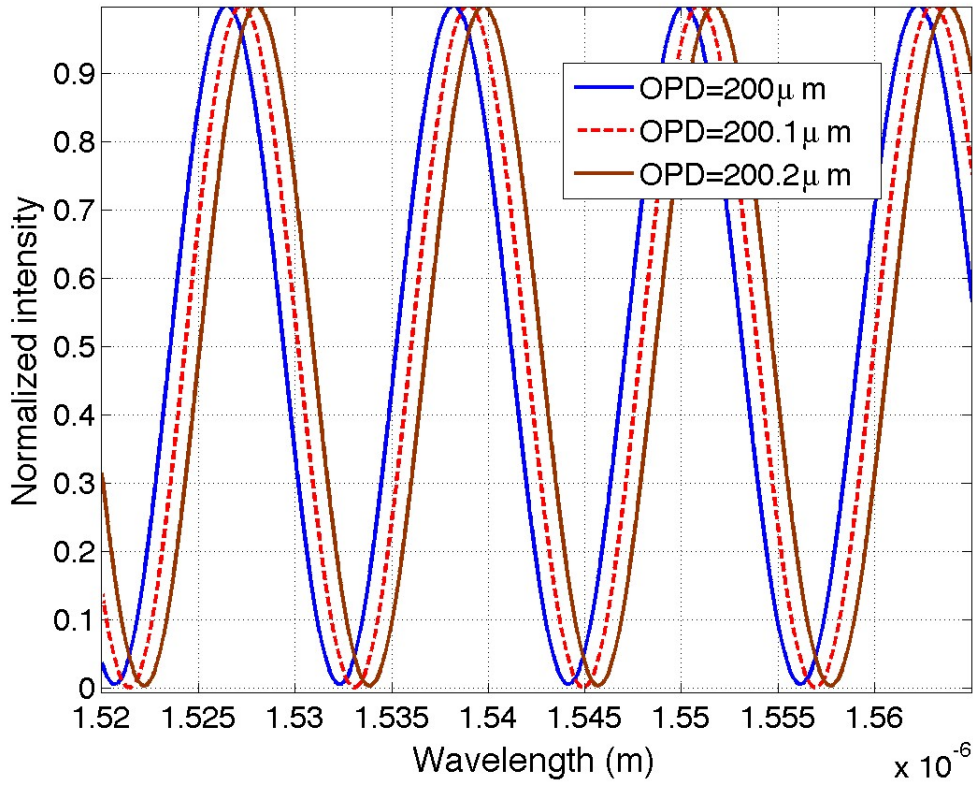


Figure 4-6: Recovered spectra for all three sensors

Up to this step, spectrum has been recovered for the three sensors whose OPD values are so close in a way that the regular frequency-multiplexing method is not able to achieve so. If a sensor's OPD changes due to the temperature variation, it is not difficult to imagine that the change will be reflected in the recovered spectrum and thus is measured.

4.2 Experiments for feasibility study

The previous section shows the principle of the OFDR and provides a numeric simulation example to illustrate the flow chart of the OFDR method. In this section, experiments are carried out to confirm such feasibility. The first experiment was carried out in a case of a single mode fiber with two sensors, then the second one was done in a highly multi-moded sapphire fiber with a sapphire wafer sensor. In both experiments, Component Test System (CTS, Micron Optics Inc.) was used as the tunable light source.

4.2.1 Single mode fiber with two sensors

In this experiment, two air-gap sensors were fabricated in a single silica fiber link with a separation of around 2 cm. A reference reflection was matched in the middle of the two sensors, as shown in Figure 4-7. Light was emitted from the CTS, launched toward the reference and the sensing arm, reflected back into the photodetector inside CTS. The CTS has a built-in wavelength calibration module, from which the exact wavelength is known during a scan. Thus the data is auto-calibrated in the wavelength domain even if the wavelength scan is not perfectly linear.

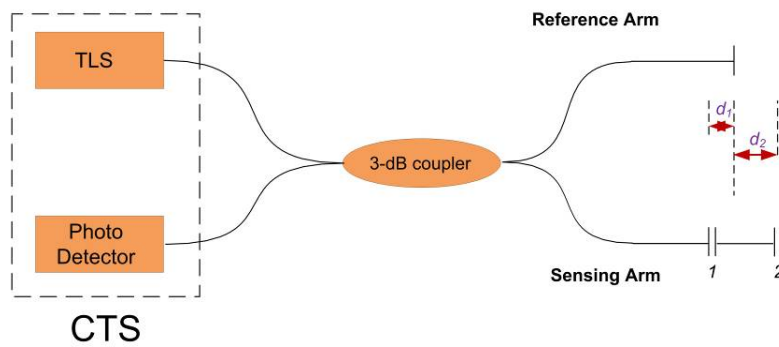


Figure 4-7: System schema for the two-sensor SMF experiment

The measured reflection spectrum from the photodetector of the CTS during a scan is shown in Figure 4-8.

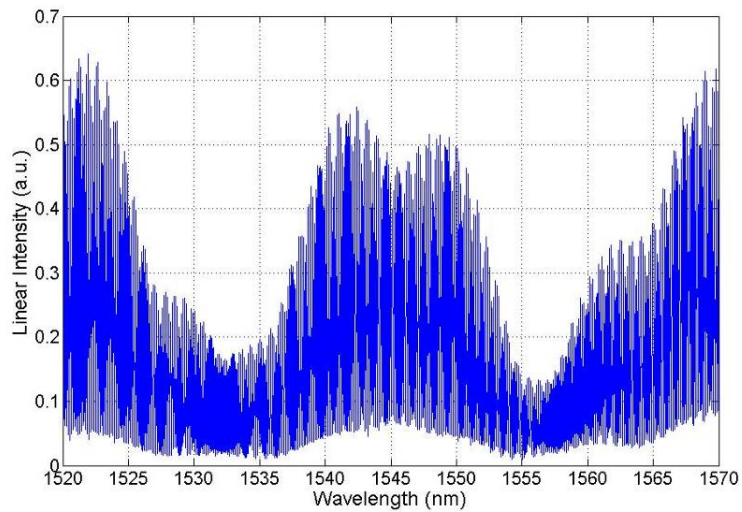


Figure 4-8: A reflection spectrum measured by the CTS

Performing FFT to the above waveform, spatial-domain reflection was obtained. Three peaks are seen from the FFT result, as shown in Figure 4-9. The peaks have decent signal to noise ratios (SNRs), at least 15 dB for all the peaks. The first peak is located at 0.6 cm away from the reference reflection point, which is caused by the interference of the reference reflection and those from the first sensor. The second peak is located at 1.3 cm away from the reference reflection point, which is introduced by the interference of the reference reflection and those from the second sensor. The last peak shown in Figure 4-9 is from the interference between the two sensors, whose location is the summation of the first two, as the geometry of sensors shown in Figure 4-7.

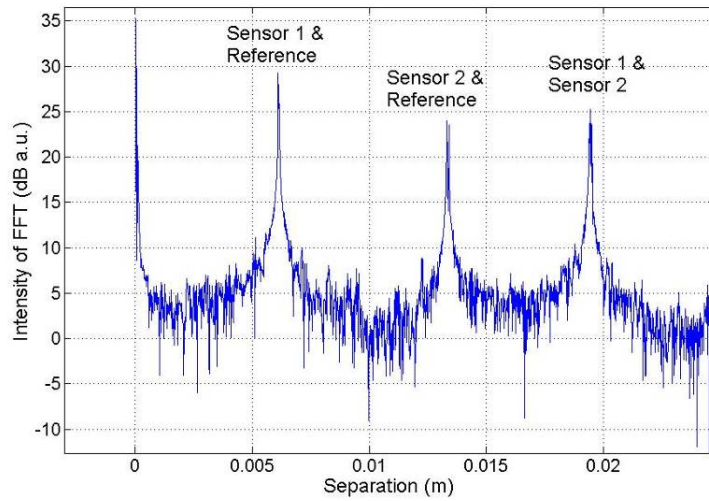


Figure 4-9: FFT of the reflection spectrum measured by the CTS

Once the FFT result is obtained, the filtering method is applied to interrogate one sensor at a time. Then spectrum can be recovered from the filtered data, following the steps described in the previous sections. Figure 4-10 and Figure 4-11 show the recovered spectra for sensor 1 and sensor 2, respectively.

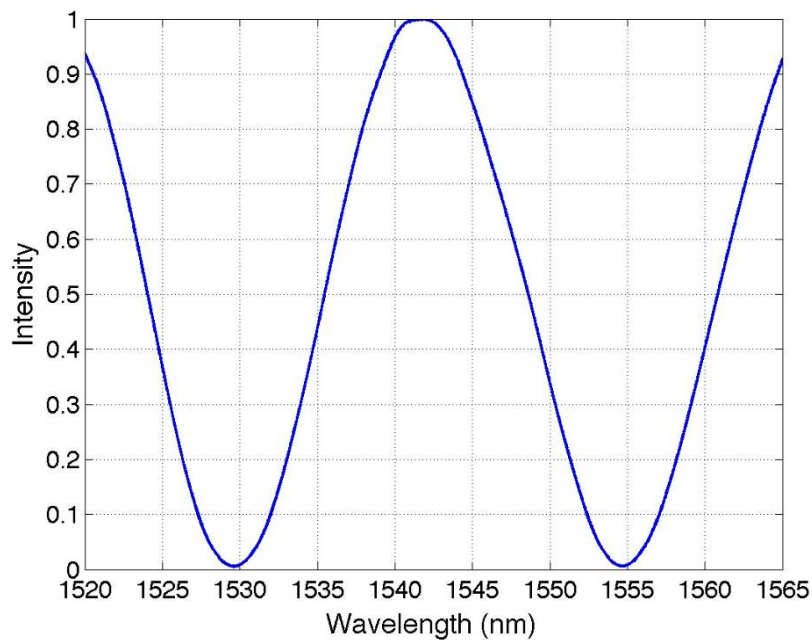


Figure 4-10: Recovered spectrum for sensor 1

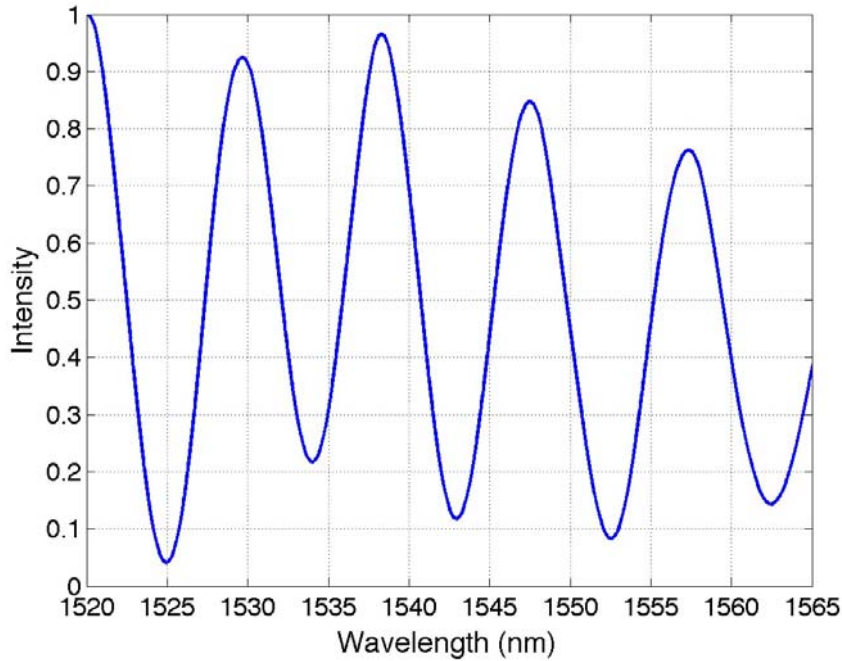


Figure 4-11: Recovered spectrum for sensor 2

Comparing Figure 4-10 and Figure 4-11, it is observed that sensor 1's spectrum is beautifully recovered while sensor 2's spectrum has some amplitude variation. This is due to the signal noise ratio (SNR) of the FFT peak seen in Figure 4-9. The better the SNR in Figure 4-9, better fidelity of the spectrum recovery has. If a sensor is farther away from the reference point, the interference becomes less efficient. In reality, it is wise to locate the sensor not far away from the reference reflection to achieve best possible SNR and consequent recovered spectrum.

From the spectrum in Figure 4-8, it is impossible to know the reflection spectrum of each individual sensor because they are superposed on each other. Using the OFDR method, spectrum was successfully recovered for both sensors. Although the two sensors have different OPD values in this case, the OFDR method in principle is able to handle sensors with even identical OPD values.

4.2.2 Sapphire fiber with a single sensor

Switching from the single mode fiber to the multi-moded sapphire fiber sees additional challenges. One of them is from the mode excitation condition, which means the set of modes excited in the sapphire fiber can be different at different wavelengths. Interference of the different sets of modes may change a lot from one wavelength to the next during the wavelength scanning. This introduces noise into the spectrum recovery as we will see from the experimental results. A second challenge is the modal dispersion in the sapphire fiber, which also changes the interference of two distant reflections. Both effects degrade the interference in multi-mode fibers and lead to broaden peaks in the FFT result of the photodetector data. The broadened peak further leads to less SNR in the sensor signal, thus presents great challenges to recover the sensor's spectrum accurately.

This experiment involves only one sapphire wafer sensor at the end of a 10 cm sapphire fiber. The reference arm is a multi-mode 105/125 μm silica fiber that is cleaved about 2.5 cm away from the tip of the sapphire wafer sensor. The optical system configuration is shown in Figure 4-12.

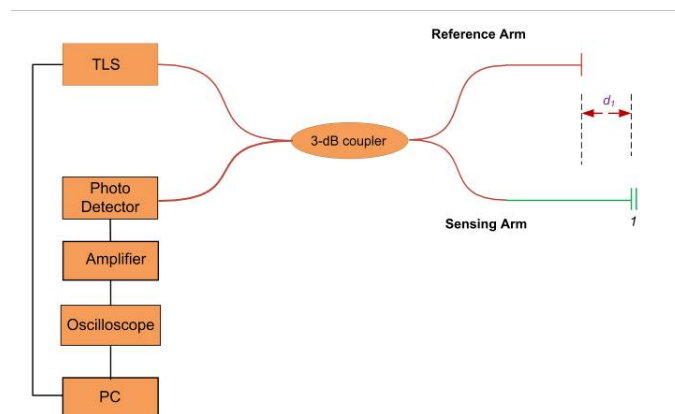


Figure 4-12: System diagram for the OFDR one sapphire sensor experiment

Since the sapphire fiber is multi-moded, an external detector was used to measure the reflected light. Figure 4-13 shows the waveform measured from the external photodetector after amplified electronically. As can be seen, the detected data has a slow envelope change due to the wafer sensor. However, the envelope is not a perfect

sinusoidal shape. On top of the slow changing sinusoidal alike envelope, there are lots of ripples. It is believed that the ripples come from both the modal excitation from the SMF to the sapphire fiber and the dispersion in the sapphire fiber. Also high frequency oscillations are seen in the measured data, which is due to the interference between the reflections from the sapphire wafer sensor and the reference reflection.

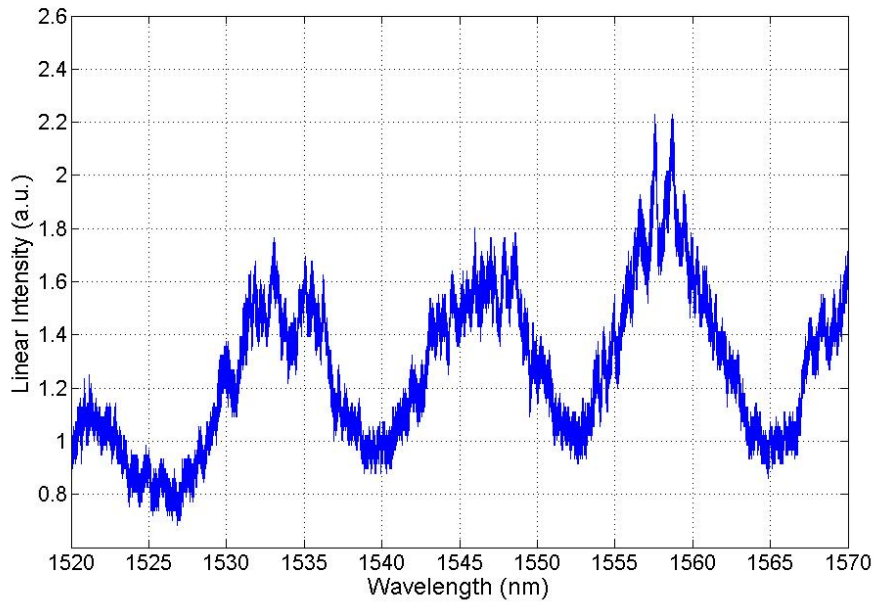


Figure 4-13: Waveform detected by the photodetector

Performing FFT on the above data, one can identify a peak in the obtained result, as shown in Figure 4-14.

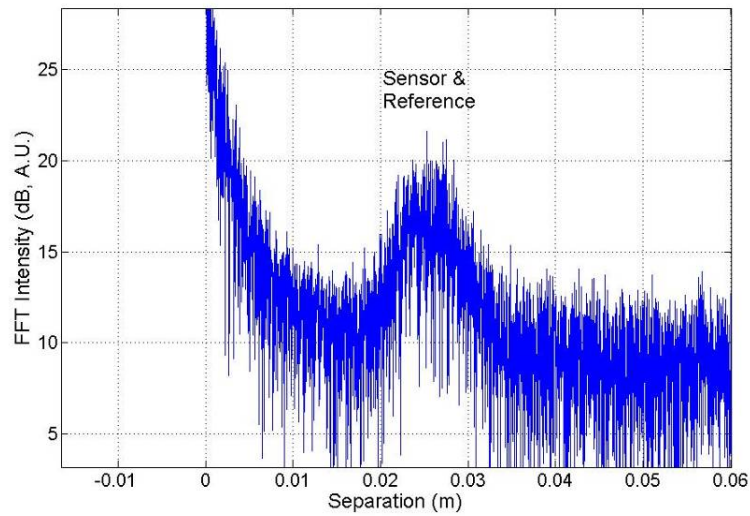


Figure 4-14: FFT of the photodetector data

The central location of the peak is around 2.5 cm, which agrees with the described sensor location. From the FFT result, we can see that FFT peak is much broader than the one in the SMF case. Also the SNR of the FFT peak in the sapphire fiber case is much worse than that in the single mode fiber case, due mainly to the modal excitation and the dispersion.

Using the same filtering technique, a band pass filter (but much broader in bandwidth) was used to select the peak in the FFT result and then iFFT was used to recover the sensor's spectrum. Recovered spectrum is shown in Figure 4-15, in which it is compared to the intensity trace of the detected data from the photodetector.

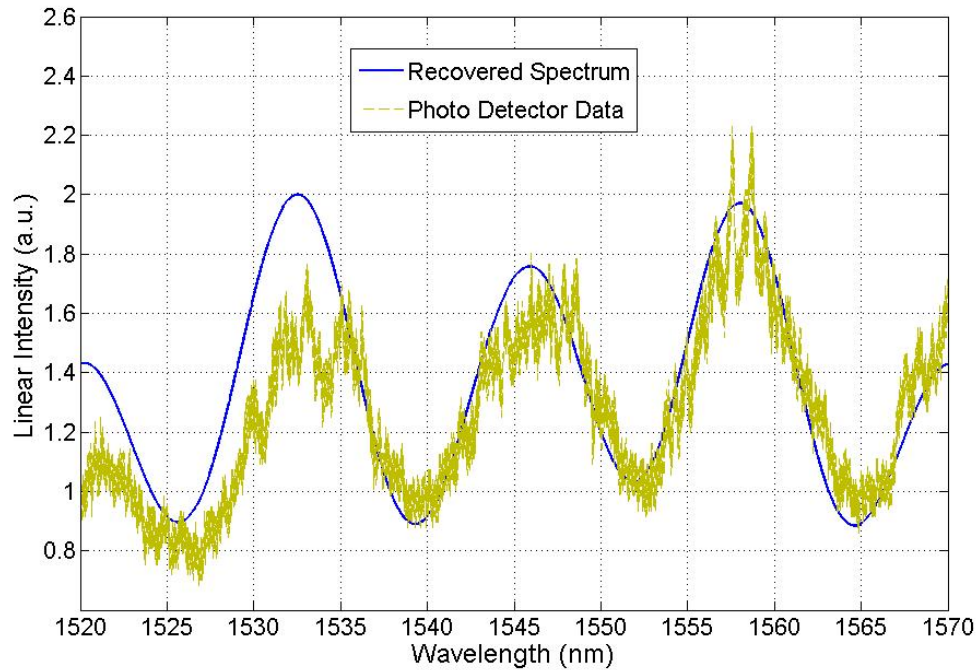


Figure 4-15: Recovered spectrum compared to the original data

It is seen from Figure 4-15 that the recovered spectrum reflects the trend of the original data very well, although not identical. The above process in the multi-mode case, as can be understood in an intuitive picture, is to recover the spectrum induced by the lower modes in sapphire fiber while filtering out those from higher modes. Thus, the recovered spectrum is a relatively smooth curve that resembles the envelope change in the detected data. Still, the broadened peak presents a great challenge to recover the original spectrum faithfully, and limits the application for this method as will be discussed later on.

To show the repeatability of the spectrum recovery, a series of recovered spectra with stable sensor condition are plotted together in Figure 4-16.

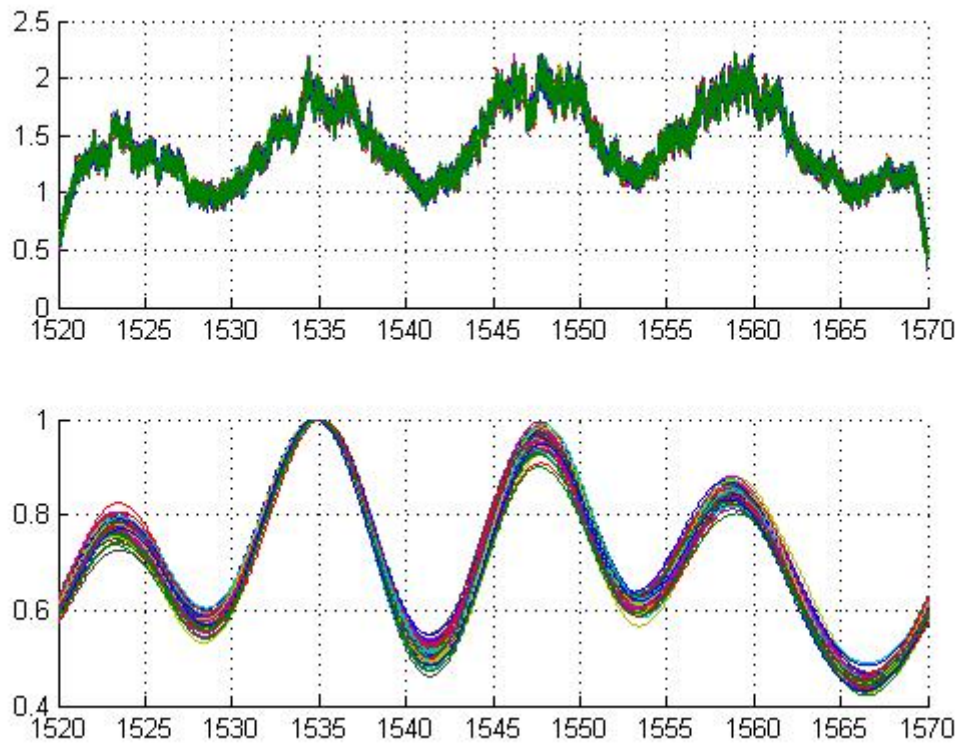


Figure 4-16: 100 consecutive recovered spectra in 5 minutes

The recovered spectra have some jittering effect caused by the multi-mode broadened sensor signal in the FFT result. This effect eventually determines the accuracy and the resolution of the OFDR based spatial-multiplexing method. The peak around 1547 nm was identified in each recovered spectrum and the peak wavelengths were plotted in Figure 4-17 to show the potential resolution of such a sensor when interrogated by the OFDR method.

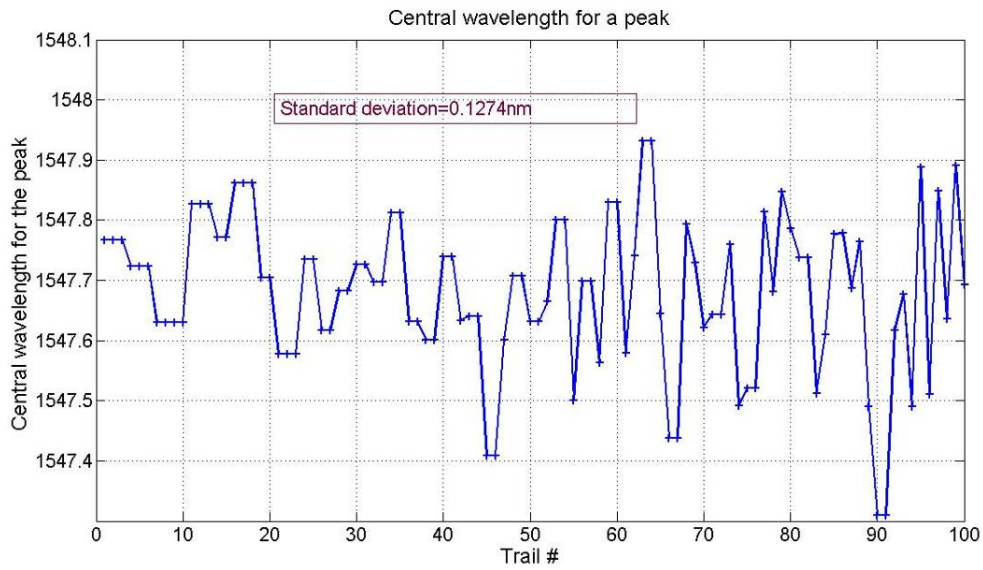


Figure 4-17: Central wavelength position changes during spectra recovery

As is shown in Figure 4-17, the standard deviation of the peak positions is about 0.127 nm. Given the peak shifts around 3 nm/100°C for the sapphire wafer sensor [62], the potential resolution (2σ) is calculated to be 8 °C.

As the temperature of the wafer sensor changes, the recovered spectrum shifts. Figure 5-18 gives an example of the data measured in experiments.

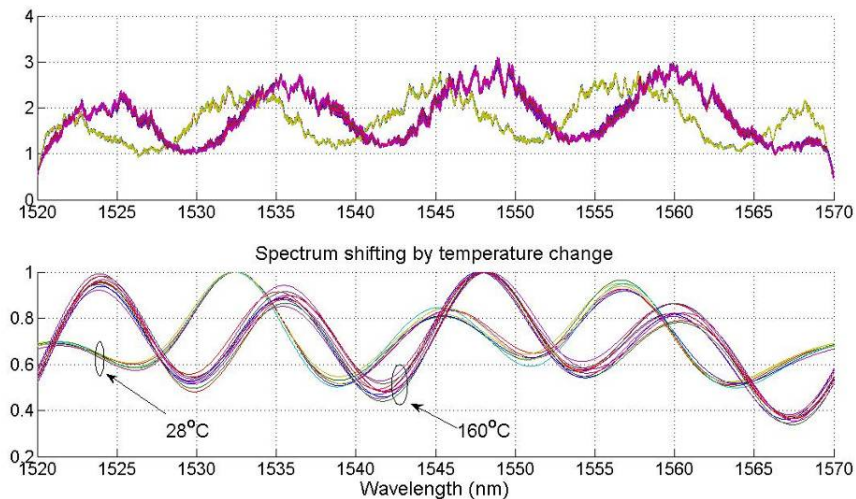


Figure 4-18: Recovered spectra shift as temperature varies

Continuously monitoring the shifting of the recovered spectrum, one can calculate the corresponding change in temperature, given the temperature sensitivity of the sapphire wafer is known.

4.3 Multiplexed sapphire sensing system

In the last section, it is demonstrated theoretically and experimentally the principle of the OFDR method for the multiplexed sensing in both single mode silica fiber and multi-mode sapphire fiber cases. In this section the OFDR based multiplexing system is to be studied in a sensing link with three identical sapphire wafer sensors. The identical sensors were made of sapphire wafers from one polishing batch. The OFDR method mentioned in the previous sections were used to demodulate signal from the last sapphire wafer sensor to demonstrate the feasibility of multiplexed sensing. However, to implement a system with good resolution and accuracy, the following aspects need to be taken care of.

- Highly repeatable and stable wavelength tuning are required for the TLS; otherwise temperature resolution would be poor;
- Non-linear wavelength tuning in the TLS needs to be corrected. Non-linear wavelength tuning (chirping) would generate distortion in the detected signal and dampen the temperature induced change;
- High detection sensitivity and large dynamic range are needed from the photodetector; otherwise it is hard to achieve large multiplexing capacity.

With the above concerns, we first improved the OFDR system to correct the wavelength tuning and to improve the photodetector's sensitivity and dynamic range. Then with the improved OFDR system, we tried to interrogate the last sapphire wafer sensor in a sensing link with three identical sapphire wafer sensors.

4.3.1 Characterization and selection of the tunable light source

As an ideal tunable light source, the wavelength shall be tuned exactly linearly (or at least in a very predictable way) while the intensity remains a constant. However, no such perfect tunable light source is available in reality. Thus, the first step is to characterize the tunable light sources on hand to select the best for later experiments. Several candidates were available in lab during this work, CTS HR-SLI by Micron Inc., tunable laser Velocity 6300 by New Focus Inc. and TUNICS-BT by Photonetics. The lasers are compared mainly for their wavelength tuning linearity and intensity variation during the wavelength tuning, with some attention paid to the coherent length of the lasers.

If the wavelength of the TLS is not linearly tuned but is supposed so, the detected signal from the photodetector will not be correctly separated in wave-number domain and eventually results in chirping error in the FFT data processing. A numerical simulation is presented here in order to show how seriously a non-linear wavelength tuning can affect the final result. All the parameters are set to be the same as the ones found from the simulation whose results are in Figure 4-2, except that the wavelength is tuned with a quadratic term rather than perfectly linearly. The quadratic term is set to be small, as shown in Figure 4-19.

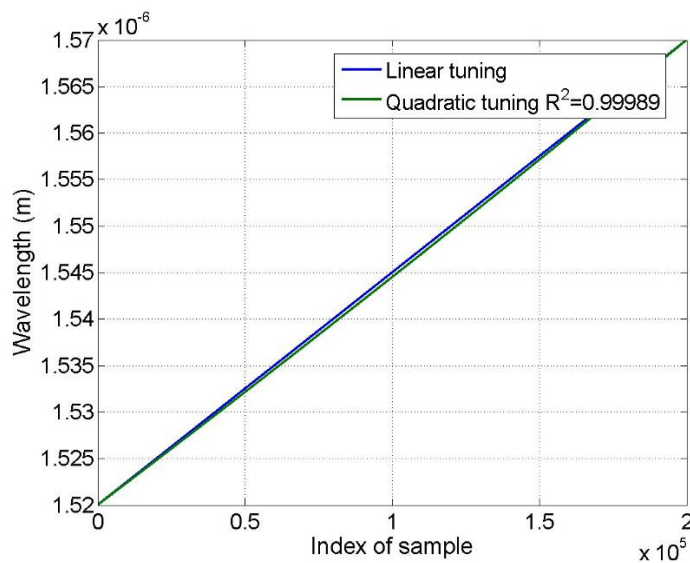


Figure 4-19: Non-linear wavelength tuning curve

In order to quantify the non-linear wavelength tuning, we applied linear curve fitting to calculate the adjusted R-square, which was found to be 0.99989 for the results shown in Figure 4-19. If the wavelength were tuned with such a quadratic term, the FFT in OFDR signal processing would have the following results seen from Figure 4-20.

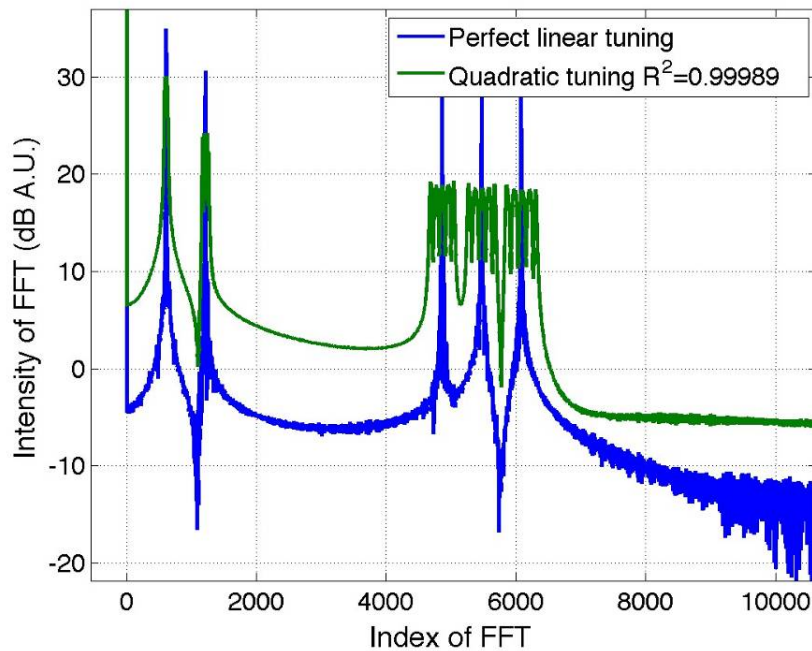


Figure 4-20: FFT of the photodetector data with a non-linear wavelength tuning

As can be seen directly from Figure 4-20, the noise floor of the FFT results is lifted up and the peaks are broadened because of the non-linear wavelength tuning. The peak broadening effect is more serious at higher frequencies than at lower frequencies. Furthermore, the non-linear wavelength tuning blurred the peaks and introduced cross-talk into sensors. The recovered spectrum without compensating such a tuning non-linearity is shown in Figure 4-21. Compared recovered spectrum from a perfect linear wavelength tuning (blue), the one from a non-linear wavelength tuning (red) has an intensity modulation that causes distortions in the recovered spectrum. Furthermore, it also changes the peak/valley separation and will lead to error in temperature measurement because it artificially shifts the peak and valley wavelengths. This distortion can not be compensated unless the non-linear wavelength tuning is characterized and compensated accordingly before the spectrum recovery.

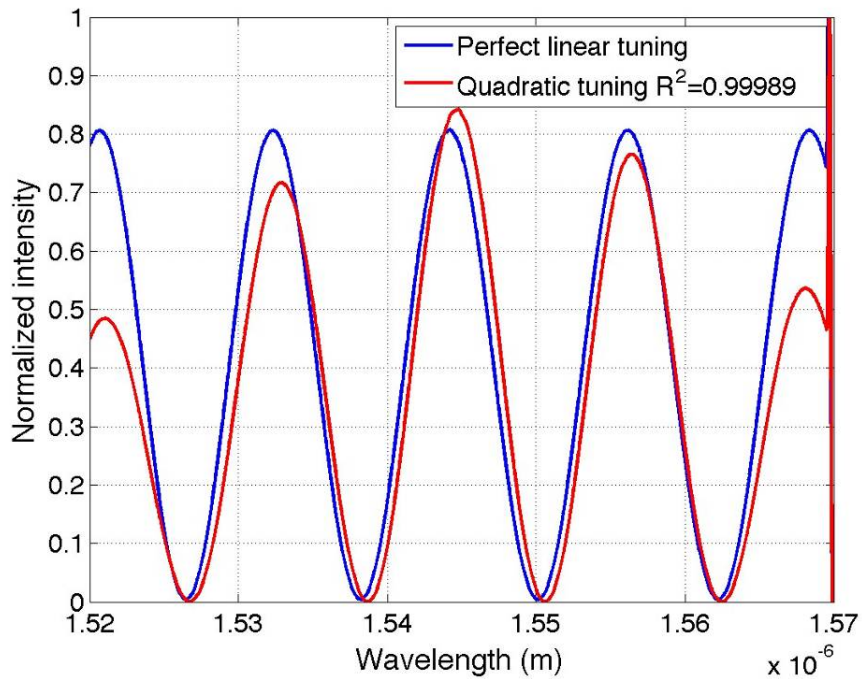


Figure 4-21: Recovered spectrum with non-linear wavelength tuning

The commercial tunable light sources are mostly designed to tune around 1550 nm in wavelength, thus a hydrogen cyanide gas cell was used for characterization and compensation of the non-linear wavelength tuning. The gas cell has absorption lines from 1528 nm to 1562 nm, which makes such a gas cell good for the wavelength range of interest. Figure 4-22 is a picture of the gas cell used in experiments.



Figure 4-22: HCN gas cell for calibration of the wavelength tuning

Figure 4-23 gives calibration curves of the wavelength tuning of the CTS as measured by the HCN gas cell. The intrinsic wavelength tuning is not quite linear from the CTS, however the problem can be addressed nicely by using a cubic curve fitting. The fitted curve for wavelength tuning had a R-square of six nines, which shall be sufficient for the OFDR system whose measurement span is within several centimeters.

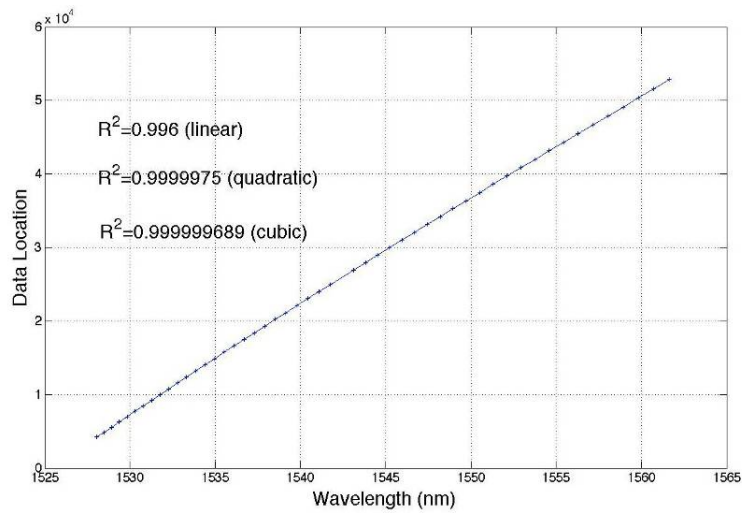


Figure 4-23: Calibration of wavelength tuning for CTS

The New Focus tunable laser Velocity 6300 has a better intrinsic wavelength tuning linearity, as shown Figure 4-24. When the tuning speed is set to be 10 nm/s, the laser had a wavelength tuning linearity whose R-square had five nines without compensation.

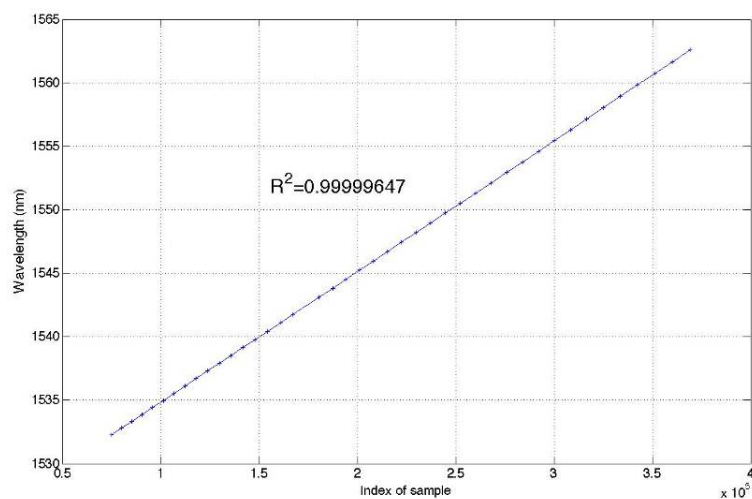


Figure 4-24: Calibration of wavelength tuning for Velocity 6300

A similar result is seen from the Photonetics TUNICS-BT tunable laser, whose wavelength tuning also had five nines in the R-square even without compensation.

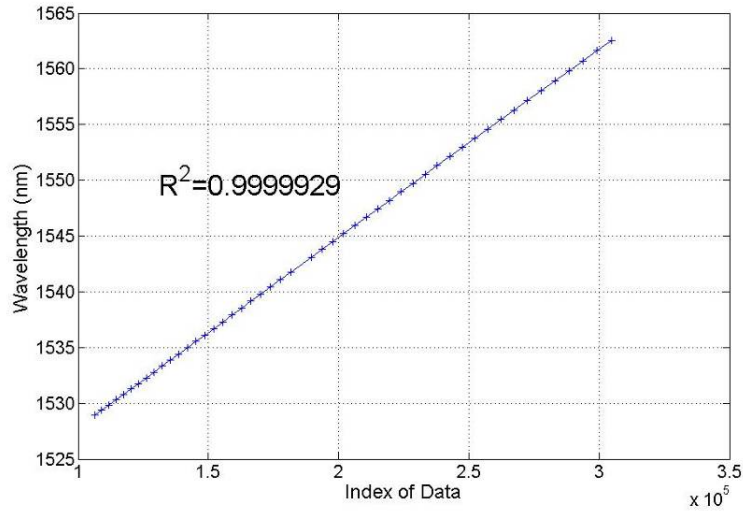


Figure 4-25: Calibration of wavelength tuning for TUNICS-BT

Another important factor of the tunable light source is the coherent length. The coherent length of the CTS was measured to be around 8 cm, while those of the New Focus and the Photonetics laser were found to be in the order of meters.

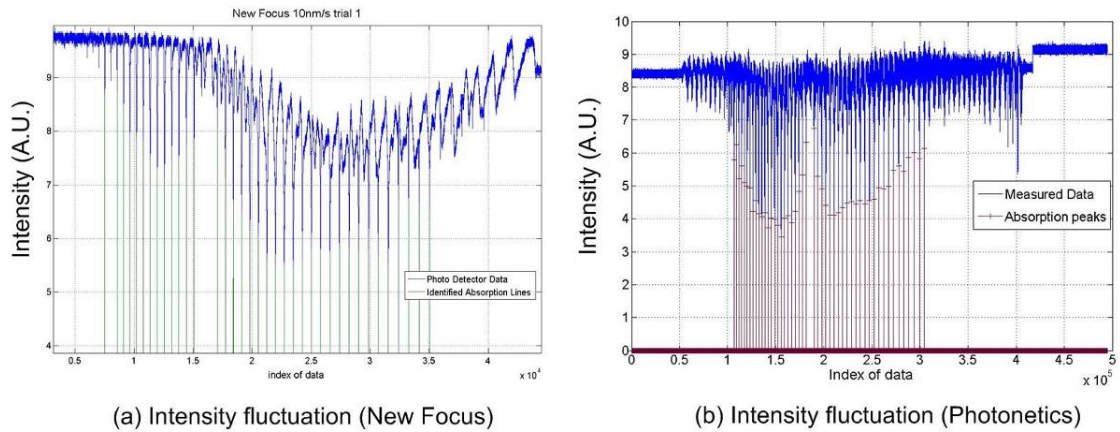


Figure 4-26: Intensity fluctuation of tunable lasers during wavelength tuning

However, the New Focus and the Photonetics tunable lasers both presented serious intensity fluctuation during the wavelength tuning, as is seen from Figure 4-26. The intensity variation was about the same in frequency as the sensor's spectrum. Thus the

intensity noise will be regarded as the sensor's spectrum. It may result in serious error in recovering the sensor's spectrum. Unfortunately the intensity fluctuation was not repeatable and thus impossible to be compensated. In contrast, the intensity fluctuation of the CTS during the wavelength tuning (Figure 4-27) is much smaller and the frequency of the intensity noise is away from the frequency of the sensor's spectrum. This intensity noise may be suppressed later by digital filtering since the frequency of intensity noise is much larger than that of the sensor's spectrum.

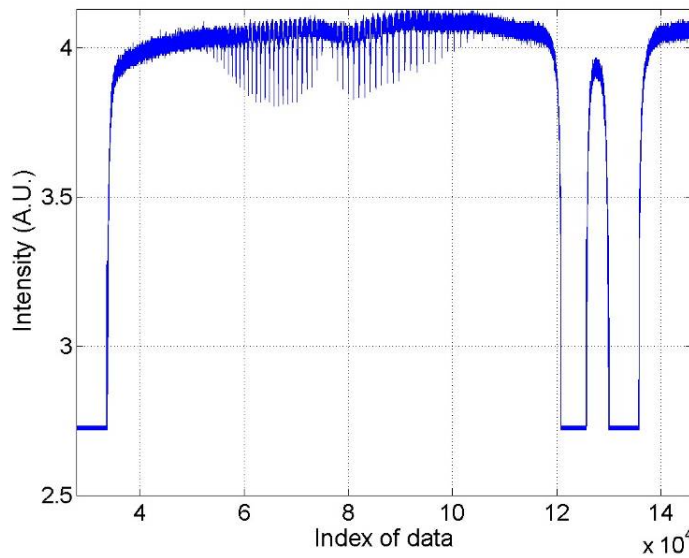


Figure 4-27: Intensity fluctuation of the CTS during a wavelength tuning

Table 4-1: Comparison of different tunable light sources

	Tuning linearity	Coherent length	Intensity fluctuation
CTS	Good, addressable	~8cm	Small, high frequency
Velocity 6300	Excellent	>1m	Large, same as sensor spectrum
TUNICS-BT	Excellent	>1m	Large, same as sensor spectrum

Table 4-1 summarizes the comparison of the aforementioned tunable light sources. Velocity 6300 and TUNICS-BT tunable lasers are good in both tuning linearity and coherent length, but the intensity fluctuation during the wavelength tuning disqualifies them from being a good tunable light source for the OFDR application. CTS, although is very limited in the coherent length, is good in intensity fluctuation. The tuning linearity of the CTS is not excellent intrinsically, but can be readily addressed by the HCN gas absorption cell. The penalty of using the CTS is also significant. Since the coherent length is only 8 cm, we can only detect one or two sensors at a time. Reference arms with different lengths and an optical switch are needed to simultaneously interrogate more than two sensors.

4.3.2 Optical detection and data acquisition system

As more and more sensors are cascaded into the single sapphire fiber link, the last sensor would inevitably experience accumulated optical loss that prohibits its reflections being effectively detected by the photodetector.

Since the reflections on each individual sensor interfere with the reference reflection, this challenge can be partially solved by introducing a very strong reference reflection. As can be found from Equation 4-4, the detected signal from a sensor is proportional to the square root of the reference reflection multiplied by the sensor's reflection.

$$\tilde{I}_t(\lambda) \propto \sqrt{I_r(\lambda)I_s(\lambda)} \quad \text{Equation 4-7}$$

A strong reference reflection gives two benefits. First, the square root is an amplifier that allows detection of small reflections from the sensors. Second, it virtually enhances the dynamic range of the photodetector by a factor of 2 because of the square root. For example, $I_s(\lambda)$ increases 20 dB only results 10 dB increase in the interferometric intensity due to the square root effect.

In experiment, we used a silver coated fiber as the reference reflection. The reflection coefficient was almost 100% with the silver coating. In order to avoid saturation in the photodetector by the strong reflection, a balanced detector was introduced to remove the

DC component in the detected signal. New Focus Model 2117 balanced detector (Figure 4-28) was used to do so and its key parameters are listed in Table 4-2.



(a) FC cable input panel (b) Output and setting panel

Figure 4-28: Picture of the New Focus 2117 balanced detector

Table 4-2: Key parameters for the Model 2117 balanced detector

Wavelength range	800-1700 nm	Bandwidth (-3 dB)	10 MHz
Maximum Gain	18.8×10^6 V/A	Responsivity	1.0 A/W
NEP	0.4 pW/ $\sqrt{\text{Hz}}$	Common Mode Rejection	25 dB

To go with the balanced detector, a variable optical attenuator (VOA, JDSU, HA9) was used to find the best DC operating point. Figure 4-29 gives a picture of the VOA.



Figure 4-29: Variable optical attenuator for balanced detection

In the previous experiments, an oscilloscope (LeCroy) with a 10-bit A/D converter was used. In order to further improve the SNR of the sensor signal, a 3 MB/s 16-bit A/D conversion card (Spectrum, M2i.4650) was used for later experiments.

Provided with the discussions in the first part of this section, a modified OFDR system diagram is shown in Figure 4-30. Compared with the one in Figure 4-1, key changes are the HCN gas cell for calibration of the wavelength tuning and the balanced detector for DC signal cancellation.

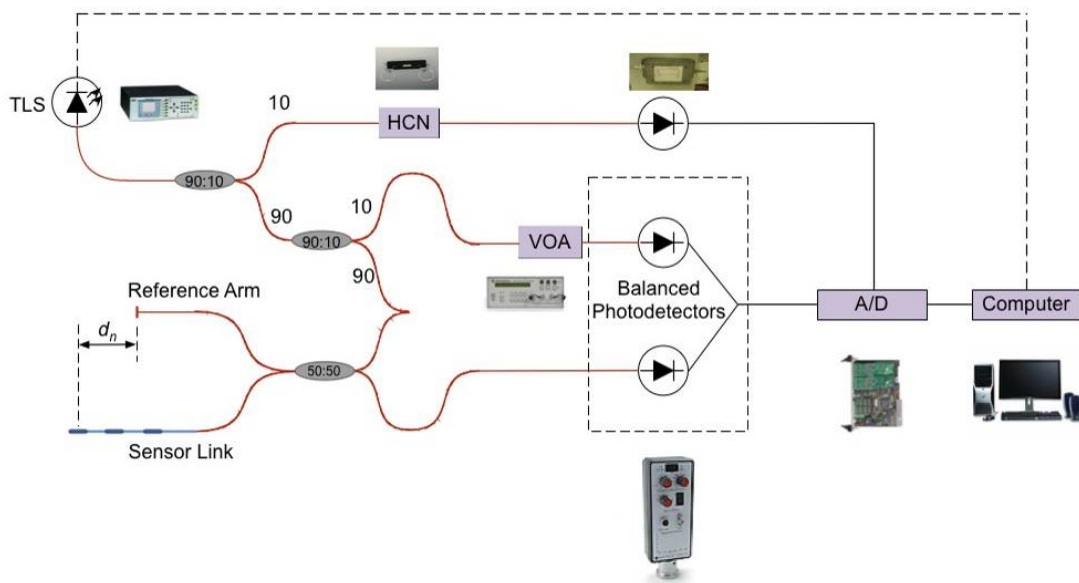


Figure 4-30: System diagram of the modified OFDR system

4.3.3 Experimental results

Three pieces of sapphire wafers with almost identical OPD values were chosen to fabricate three sapphire wafer sensors. The first two sensors were named in-line sensors and the last one was named end-sensor.

The in-line sensors were fabricated by opening a slit inside a ZrO_2 tube, as illustrated in Figure 4-31. Dicing blade whose thickness is about $50\ \mu\text{m}$ (FSN1703011, Semicon Tools Inc.) was used to cut a slit in the 1mm OD, $80\ \mu\text{m}$ ID ZrO_2 tube (Swiss Jewel Inc.). The diced slit had a width around $80\ \mu\text{m}$ and a depth of $700\ \mu\text{m}$ or so in order to fully expose

the inside hole of the tube. A piece of sapphire wafer (Valley Design Corp.) with a thickness around $75\ \mu\text{m}$ was placed into the slit. Two sapphire fibers were inserted from both ends of the tube to contact the sapphire wafer while monitoring the spectrum in real-time. Once good fringes were obtained from the sensor, glue was used to permanently bond the sapphire wafer to the ZrO_2 tube.

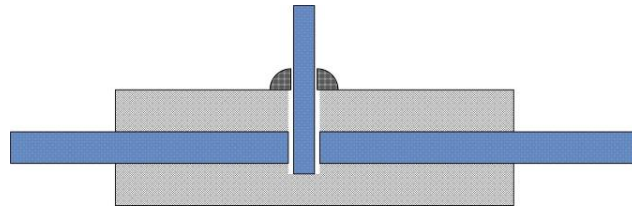
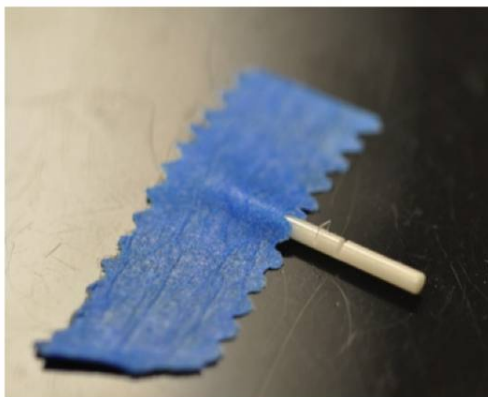
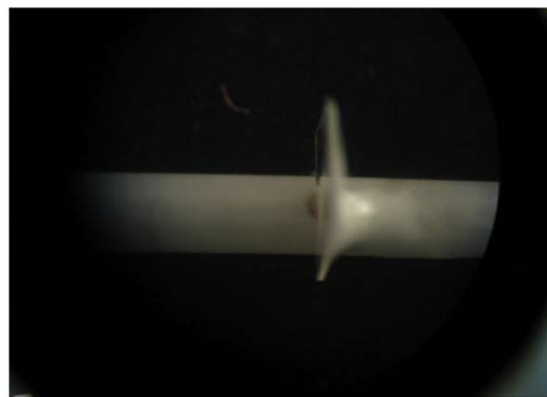


Figure 4-31: Structure of the sapphire wafer in-line sensor



(a) Sapphire wafer in slit



(b) Bonded in-line sensor

Figure 4-32: Picture of the sapphire wafer in-line sensor

The end-sensor was just a sapphire wafer bonded to a sapphire fiber through an alumina tube, as shown in Figure 4-33.

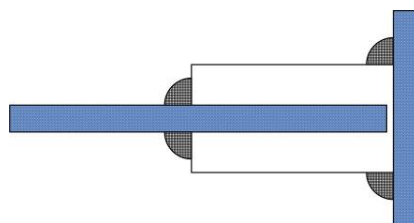


Figure 4-33: Structure of the sapphire wafer end-sensor

After fabrication, the three sapphire wafer sensors were examined by the white light system mentioned in Figure 3-3 individually. Spectrum of each sensor is plotted in Figure 4-34.

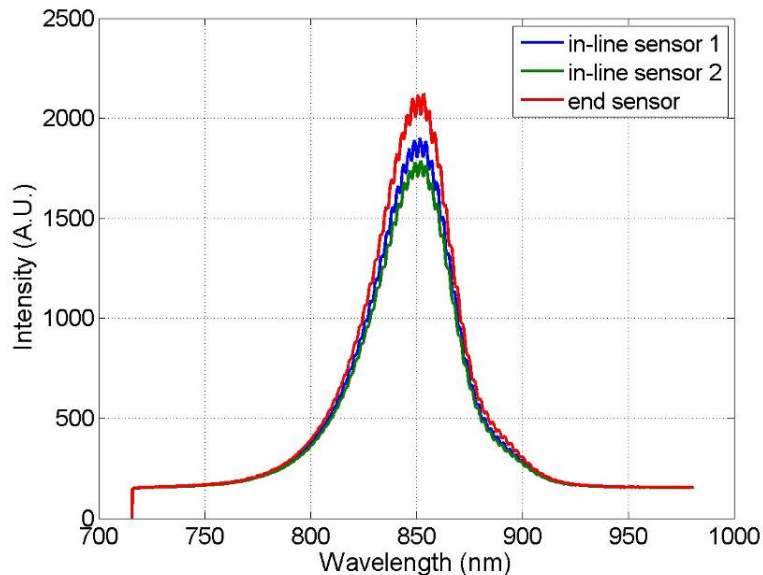


Figure 4-34: Spectra of the three sapphire wafer sensors by the white light system

The OPD of each sensor was founded to be 269.438 μm , 274.624 μm , and 276.764 μm , respectively. Since the in-line sensors were desired to have low optical transmission loss, they were measured in the optical transmission loss. The losses were found to be 1.4 dB and 2.2 dB, which are low enough to be used in the OFDR system with enhanced dynamic range. In the end, three sapphire wafer sensors were cascaded into a single fiber link as shown in Figure 4-35. The separations of the sensors were measured to be 4 cm and 10 cm. The lead-in sapphire fiber had a length of 5.6 cm.



Figure 4-35: Picture of the fiber link with three identical wafer sensors

Since the total span of the sapphire fiber sensors was beyond the coherent length of the CTS, only the third sensor was analyzed by the OFDR system. The third sensor was chosen because it had the worst SNR in the reflected spectrum.

During experiments, the reference reflection point was aligned to be about 2 cm away from the last sapphire wafer sensor. A series of the photodetector data is shown in Figure 4-36.

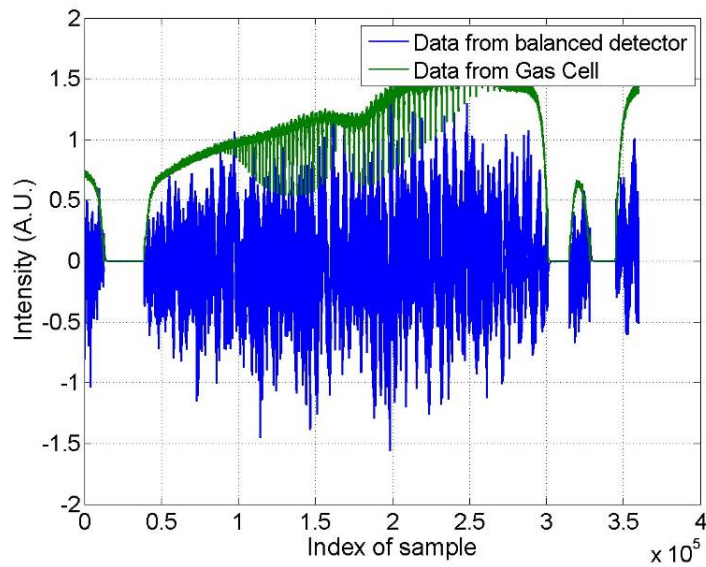


Figure 4-36: Photodetector data from the new OFDR system

The FFT result of the previous data revealed two peaks. The first one is the interference between the reference reflection and those from the sapphire end-sensor, the other one is the interference of in-line sensor 1 and sensor 2.

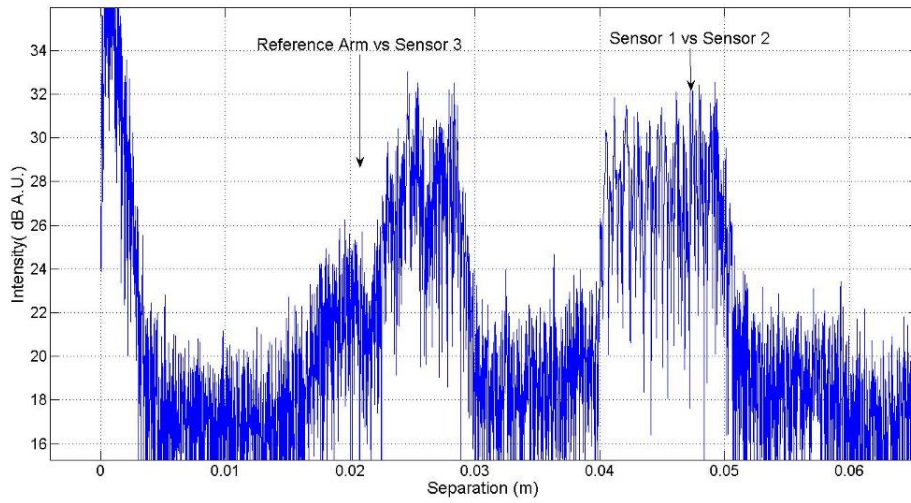


Figure 4-37: FFT result of the photodetector data

Applying the OFDR signal demodulation method toward the first peak in Figure 4-37, the following recovered spectra were obtained at different temperatures.

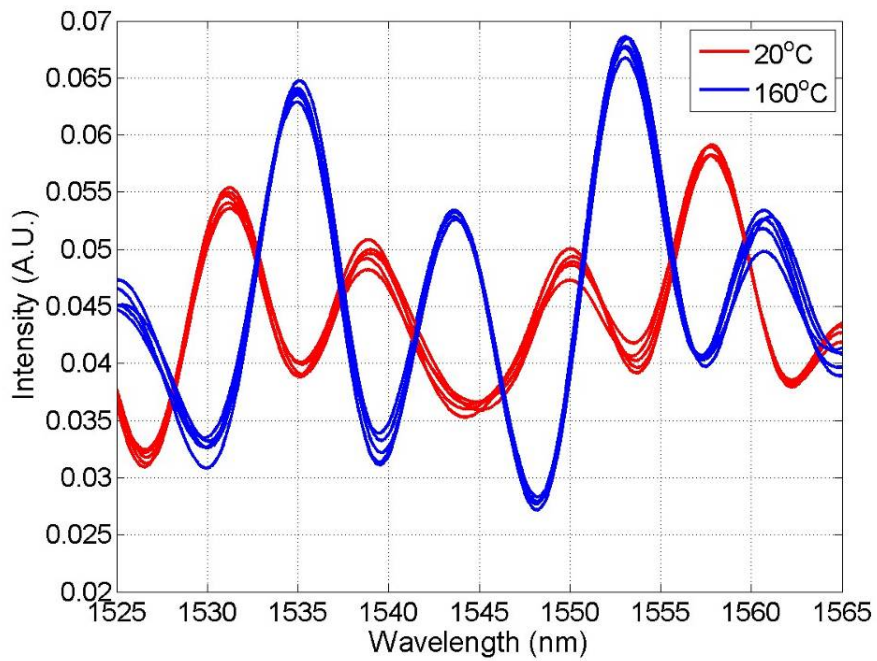


Figure 4-38: Recovered spectra at different temperatures

As what was demonstrated through the single sapphire sensor case in Figure 4-18, the recovered spectra shift toward longer wavelength when temperature increases. However, due to reduced SNR on the last sensor, the peak positions fluctuate within a range of ± 0.3 nm. Given the sensitivity of sapphire wafer over temperature, the equivalent temperature range is estimated to be ± 10 °C. The two in-line sensors are expected to have better resolution because of higher SNR than the end-sensor's.

As a summary, the feasibility of the OFDR based multiplexed sensing is demonstrated on the sapphire fiber through a link with three identical sensors. However, due to the highly multi-moded nature of the sapphire fiber, the recovered spectra suffer great distortion, from which no absolute OPD can be calculated. Temperature measurement is achieved by tracking the spectrum change continuously. Not being able to calculate the sensor's OPD value from the recovered spectrum makes this method a relative measurement.

Chapter 5 Conclusion and future work

In this dissertation, we have proposed and studied sensing solutions for ultra-miniaturized temperature and multiplexed high temperature sensing, to enhance the capability of the sapphire fiber based sensing technology.

First of all, we have studied the optical thin film coating on the sapphire fiber tip as a temperature sensor for non-invasive embedded sensing applications. This method intrinsically generates two parallel optical surfaces by the thin film to construct an FPI cavity that leads to a high fringe contrast. Also the sensor fabrication method is batch fabrication oriented and thus has a potential to be used for mass production. To demonstrate the high temperature sensing of the thin film sensors, Ta_2O_5 , TiO_2 , and ZrO_2 have been studied as the thin film material. In the lab we have demonstrated sensors that work up to 1200 °C with a film thickness around 700 nm and showed a potential of the ZrO_2 thin film sensors to function up to 1500 °C. Based on the existing equipment and signal processing method, the thin film sensors had a temperature resolution (2σ) of about 12.6 °C. This sensor fabrication method has provided a new area of research, which combines the material science background and the optical thin film coating technology into the optical sensor fabrication, to provide a sensor that can be easily produced with a relatively low fabrication cost. Future research can be focused on finding new materials that can work with sapphire fiber for sensing up to 2000 °C, which is close to the melting point of the sapphire fiber. Once such a material is found, one needs to choose the deposition method to get the best possible film quality. The current optical interrogation method is based on a halogen light source and a low-resolution spectrometer. The low-density halogen light source makes the sensor vulnerable to the intensity noises such as one from the blackbody radiation. In the future, a broad-band supercontinuum light source can be used to replace the halogen light to greatly enhance the sensor's immunity to intensity noises. If using a spectrometer of higher wavelength resolution, the thin film sensor is expected to have better temperature resolution.

On the other hand, this dissertation has also demonstrated sapphire fiber based multiplexed sensing methods for high temperature applications, an effort that was not reported to date to the knowledge of the author. Frequency- and spatial-multiplexing methods have been studied with good results. The frequency-multiplexing was made possible by the improvements in the air-gap sensor fabrication. Three sapphire air-gap sensors with different OPD values were fabricated in a single sapphire link to demonstrate the multiplexed sapphire sensing with a high sensitivity. The frequency-multiplexing method is approved to be an absolute measurement method but has limited multiplexing capability due to the optical loss at the air-gap sensors. In contrast, the spatial-multiplexing method can potentially accommodate more sensors but is not an absolute measurement method due to the spectrum recovery from the interferences in the multi-moded sapphire fiber. However there is room for future research to further improve the sensor fabrication and signal processing method to attempt an absolute measurement using the spatial-multiplexing method. Although temperature measurement was used to illustrate the multiplexing feasibility, the principle shall be applicable to any other sensing purposes.

This dissertation also enabled other sapphire fiber based sensing possibilities in multiple ways. First of all, the single-layer thin film on the sapphire fiber has been demonstrated to be a temperature sensor. Similar to the principle of fiber Bragg gratings, stacking layers with alternating films of different refractive indices can have a wavelength-dependent reflection/transmission spectrum, which can be used as a wavelength filter. In principle, the spectrum is dependent on the optical thickness of each thin film layer and the stacking film structure may be used as a temperature sensor as well. Secondly, the air-gap sensor fabrication technique has also enabled the possibility to fabricate sapphire sensors for other parameters, such as pressure. One possible solution for the sapphire fiber based pressure sensing is to have the air-gap sensor hermetically sealed by lasers. The external pressure change shall be reflected on the OPD change of the air-gap sensor since the zirconia tube would deform in presence of the external pressure. Last but not least, as a step further than the multiplexed sapphire sensing discussed in this dissertation, fully distributed sapphire sensing still awaits a solution. One possible method to attempt

this is to use some method to fabricate some discontinuities in the sapphire fiber to generate random reflections that can be used for fully distributed sensing. The OFDR method, due to its advantage of high spatial resolution, may be used to interrogate the machined sapphire fiber for fully distributed sensing.

Bibliography

- [1] C. Lee, *et al.*, "Performance of a fiber-optic temperature sensor from -200 to 1050°C," *Opt. Lett.*, vol. 13, pp. 1038-1040, Nov 1 1988.
- [2] S. J. Saggese, *et al.*, "Hollow sapphire waveguides for remote radiometric temperature measurements," *Electronics Letters*, vol. 27, pp. 707-709, 1991.
- [3] X. FANG, *et al.*, "A Fiber optic High-temperature Sensor," *Sensors and Actuators A-physical*, vol. 44, pp. 19-24, 1994.
- [4] L. Tong, *et al.*, "A zirconia single-crystal fibre-optic sensor for contact measurement of temperatures above ...," *Meas. Sci. Technol*, Jan 1 1999.
- [5] Y. Zhang, *et al.*, "BPDI based optical sensor for real-time high temperature measurements for the coal gasification process," in *Proceedings*, 2002, pp. 9-15.
- [6] D. Grobnic, *et al.*, "Sapphire fiber Bragg grating sensor made using femtosecond laser radiation for ultrahigh temperature applications," *Photonics Technology Letters, IEEE*, vol. 16, pp. 2505-2507, 2004.
- [7] Z. Huang, *et al.*, "Sapphire temperature sensor coal gasifier field test," in *Proceedings*, 2004, pp. 27-36.
- [8] F. B. Shen, *et al.*, "UV-induced intrinsic Fabry-Perot interferometric sensors and their multiplexing for temperature and strain sensing," *Proceedings*, vol. 6174, p. 61740D, 2006.
- [9] Y. Zhang, *et al.*, "Single-crystal sapphire based optical polarimetric sensor for high temperature measurement," *SENSORS*, vol. 6, pp. 823-834, 2006.
- [10] Z. Wang, *et al.*, "Ultra-short fiber Bragg grating intrinsic Fabry-Perot interferometric sensors for quasi-distributed strain and temperature sensing," *Sensors and Smart Structures Technologies for Civil, Mechanical, and Aerospace Systems 2007, Pts 1 and 2*, vol. 6529, pp. U968-U976, 2007.
- [11] A. Zaitsev, *et al.*, "Temperature and Chemical Sensors Based on FIB-Written Carbon Nanowires," vol. 8, pp. 849-856, Jun 1 2008.
- [12] C. Mou, *et al.*, "Fiber Laser Incorporating an Intracavity Microchannel for Refractive Index and Temperature Sensing," *Photonics Technology Letters, IEEE*, vol. 21, pp. 1559-1561, 2009.
- [13] H. Xia, *et al.*, "Edge technique for direct detection of strain and temperature based on optical time domain reflectometry," *Appl. Opt.*, vol. 48, pp. 189-197, 2009.
- [14] Y. Wang, *et al.*, "High-Temperature Sensing Using Miniaturized Fiber In-Line Mach-Zehnder Interferometer," *Photonics Technology Letters, IEEE*, vol. 22, pp. 39-41, 2010.
- [15] G. WANG, *et al.*, "2-MODE FABRY-PEROT OPTICAL FIBER SENSORS FOR STRAIN AND TEMPERATURE-MEASUREMENT," *Electronics Letters*, vol. 27, pp. 1843-1845, 1991.
- [16] M. E. Froggatt and J. Moore, "High-Spatial-Resolution Distributed Strain Measurement in Optical Fiber with Rayleigh Scatter," *Appl. Opt.*, vol. 37, pp. 1735-1740, Apr 1 1998.
- [17] Z. Huang, *et al.*, "Intrinsic Fabry-Perot fiber sensor for temperature and strain measurements," *Ieee Photonics Technology Letters*, vol. 17, pp. 2403-2405, 2005.

- [18] S. T. Kreger, *et al.*, "High Resolution Distributed Strain or Temperature Measurements in Single- and Multi-Mode Fiber Using Swept-Wavelength Interferometry," *Optical Fiber Sensors*, p. ThE42, Oct 23 2006.
- [19] O. Frazao, *et al.*, "Fabry-Perot Cavity Based on a Suspended-Core Fiber for Strain and Temperature Measurement," *Photonics Technology Letters, IEEE*, vol. 21, pp. 1229-1231, 2009.
- [20] H. Jung, *et al.*, "Bending and Strain Sensitivities in a Helicoidal Long-Period Fiber Gratings," *Photonics Technology Letters, IEEE*, vol. 21, pp. 1232-1234, 2009.
- [21] M. Müller, *et al.*, "Analytical solution of four-mode coupling in shear strain loaded fiber Bragg grating sensors," *Opt. Lett.*, vol. 34, pp. 2622-2624, Sep 1 2009.
- [22] M. A. Soto, *et al.*, "Enhanced Simultaneous Distributed Strain and Temperature Fiber Sensor Employing Spontaneous Brillouin Scattering and Optical Pulse Coding," *Photonics Technology Letters, IEEE*, vol. 21, pp. 450-452, Apr 1 2009.
- [23] Q. Wu, *et al.*, "Use of a single-multiple-single-mode fiber filter for interrogating fiber Bragg grating strain sensors with dynamic temperature compensation," *Appl. Opt.*, vol. 48, pp. 5451-5458, Oct 10 2009.
- [24] D.-P. Zhou, *et al.*, "Simultaneous Strain and Temperature Measurement With Fiber Bragg Grating and Multimode Fibers Using an Intensity-Based Interrogation Method," *Photonics Technology Letters, IEEE*, vol. 21, pp. 468-470, Apr 1 2009.
- [25] W. Zou, *et al.*, "Complete discrimination of strain and temperature using Brillouin frequency shift and birefringence in a polarization-maintaining fiber," *Opt. Express*, vol. 17, pp. 1248-1255, 2009.
- [26] A. WANG, *et al.*, "OPTICAL FIBER PRESSURE SENSOR BASED ON PHOTOELASTICITY AND ITS APPLICATION," *Lightwave Technology*, vol. 10, pp. 1466-1472, 1992.
- [27] A. Wang, *et al.*, "Split-spectrum intensity-based optical fiber sensors for measurement of microdisplacement, strain, and pressure," *Appl. Opt.*, vol. 35, pp. 2595-2601, 1996.
- [28] R. May, *et al.*, "SCIIB pressure sensors for oil extraction applications," in *Proceedings*, 1999, pp. 29-35.
- [29] W. J. Pulliam, *et al.*, "Micromachined SiC fiber optic pressure sensors for high-temperature aerospace applications," 2000, pp. 21-30.
- [30] W. Peng, *et al.*, "Cubic zirconia-based fiber optic pressure sensor for high temperature environment," in *Proceedings*, 2003, pp. 216-222.
- [31] X. Wang, "Optical Fiber Tip Pressure Sensor," *Dissertations and Theses*, pp. 1-63, Nov 9 2004.
- [32] J. Xu, *et al.*, "Epoxy-free high temperature fiber optic pressure sensors for gas turbine engine applications," in *Proceedings*, 2004, pp. 1-10.
- [33] Y. Zhu, *et al.*, "Miniature fiber-optic pressure sensor for turbine engine," in *Proceedings*, 2004, pp. 11-18.
- [34] W. Peng, *et al.*, "High-temperature fiber optic cubic-zirconia pressure sensor," *Optical Engineering*, vol. 44, 2005.

- [35] F. Shen, *et al.*, "Measurement of the frequency response of a diaphragm-based pressure sensor by use of a pulsed excimer laser," *Opt. Lett.*, vol. 30, pp. 1935-1937, 2005.
- [36] X. Wang, *et al.*, "An Optical Fiber Tip Pressure Sensor for Medical Applications," in *Conference on Lasers and Electro-Optics/Quantum Electronics and Laser Science and Photonic Applications Systems Technologies*, 2005, p. JTuC46.
- [37] J. Xu, *et al.*, "Miniature all-silica fiber optic pressure and acoustic sensors," *Opt. Lett.*, vol. 30, pp. 3269-3271, 2005.
- [38] Y. Zhu and A. Wang, "Miniature fiber-optic pressure sensor," *Ieee Photonics Technology Letters*, vol. 17, pp. 447-449, 2005.
- [39] X. Wang, *et al.*, "All-fused-silica miniature optical fiber tip pressure sensor," *Opt. Lett.*, vol. 31, pp. 885-887, 2006.
- [40] Y. Z. Zhu, *et al.*, "High-temperature fiber-tip pressure sensor," *J. Lightwave Technol.*, vol. 24, pp. 861-869, 2006.
- [41] Y. Ge, *et al.*, "Optical MEMS pressure sensor based on a mesa-diaphragm structure," *Opt. Express*, vol. 16, pp. 21746-21752, 2008.
- [42] E. Cibula, *et al.*, "Miniature all-glass robust pressure sensor," *Opt. Express*, vol. 17, pp. 5098-5106, 2009.
- [43] W. Wang, *et al.*, "Optical pressure/acoustic sensor with precise Fabry-Perot cavity length control using angle polished fiber," *Opt. Express*, vol. 17, pp. 16613-16618, Sep 14 2009.
- [44] X. Zhang, *et al.*, "Phase modulation with micromachined resonant mirrors for low-coherence fiber-tip pressure sensors," *Opt. Express*, vol. 17, pp. 23965-23974, Dec 21 2009.
- [45] A. Roberts, *et al.*, "High-temperature optical fiber instrumentation for gas flow monitoring in gas turbine engines," in *Proceedings*, 2001, pp. 210-219.
- [46] G. Pickrell, *et al.*, "Microstructural analysis of random hole optical fibers," *Ieee Photonics Technology Letters*, vol. 16, pp. 491-493, 2004.
- [47] G. Pickrell, *et al.*, "Random-hole optical fiber evanescent-wave gas sensing," *Opt. Lett.*, vol. 29, pp. 1476-1478, 2004.
- [48] T. Jalkanen, *et al.*, "Optical gas sensing properties of thermally hydrocarbonized porous silicon Bragg reflectors," *Opt. Express*, vol. 17, pp. 5446-5456, 2009.
- [49] J. Liu, *et al.*, "Highly versatile fiber-based optical Fabry-Perot gas sensor," *Opt. Express*, vol. 17, pp. 2731-2738, 2009.
- [50] R. M. Wynne, *et al.*, "Sub-Minute Response Time of a Hollow-Core Photonic Bandgap Fiber Gas Sensor," *J. Lightwave Technol.*, vol. 27, pp. 1590-1596, Jun 1 2009.
- [51] F. Ye, *et al.*, "Multipoint Chemical Gas Sensing Using Frequency-Shifted Interferometry," *Lightwave Technology, Journal of*, vol. 27, pp. 5356-5364, 2009.
- [52] K. Oh, *et al.*, "Fiber-optic extrinsic Fabry-Perot dc magnetic field sensor," *Opt. Lett.*, vol. 29, pp. 2115-2117, 2004.
- [53] Z. Wang, *et al.*, "Optical high DC voltage sensor based on white-light interferometry," *Ieee Photonics Technology Letters*, vol. 18, pp. 2002-2004, 2006.

- [54] F. Arregui, *et al.*, "Optical fiber humidity sensor using a nano Fabry-Perot cavity formed by the ionic self-assembly method," *Sensors and Actuators B: Chemical*, vol. 59, pp. 54-59, Oct 5 1999.
- [55] D. Iannuzzi, *et al.*, "A fiber-top cantilever for hydrogen detection," *Sensors & Actuators: B. Chemical*, vol. 121, pp. 706-708, 2007.
- [56] A. Avdic, *et al.*, "Focused ion beam generated antimony nanowires for microscale pH sensors," *Appl. Phys. Lett.*, vol. 95, pp. 223106-3, Nov 30 2009.
- [57] A. WANG, *et al.*, "SAPPHIRE-FIBER-BASED INTRINSIC FABRY-PEROT-INTERFEROMETER," *Opt. Lett.*, vol. 17, pp. 1021-1023, 1992.
- [58] A. Wang, *et al.*, "Advances in sapphire-fiber-based intrinsic interferometric sensors," *Opt. Lett.*, vol. 17, p. 1544, 1992.
- [59] A. WANG, *et al.*, "Birefringence-balanced Polarimetric Optical Fiber Sensor For High-temperature Measurements," *Opt. Lett.*, vol. 17, pp. 1391-1393, 1992.
- [60] J. Kennedy and N. Djeu, "Operation of Yb:YAG fiber-optic temperature sensor up to 1600 °C," *Sensors and Actuators A: Physical*, vol. 100, pp. 187-191, Sep 1 2002.
- [61] G. Merberg and G. Harrington, "Optical and mechanical properties of single-crystal sapphire optical fibers," *Appl. Opt.*, vol. 32, pp. 3201-3209, 1993.
- [62] Y. Zhu, *et al.*, "Sapphire-fiber-based white-light interferometric sensor for high-temperature measurements," *Opt. Lett.*, vol. 30, pp. 711-713, 2005.
- [63] H. Xiao, *et al.*, "Single-Crystal Sapphire Fiber-Based Strain Sensor for High-Temperature Applications," *J. Lightwave Technol.*, vol. 21, p. 2276, 2003.
- [64] Y. Zhu, *et al.*, "Fiber-optic high-temperature sensing system and its field application," 2007, p. 675704.
- [65] Y. Zhu and A. Wang, "Surface-mount sapphire interferometric temperature sensor," *Appl. Opt.*, vol. 45, pp. 6071-6076, 2006.
- [66] F. Shen and A. Wang, "Frequency-estimation-based signal-processing algorithm for white-light optical fiber Fabry-Perot interferometers," *Appl. Opt.*, vol. 44, pp. 5206-5214, 2005.
- [67] B. Qi, *et al.*, "Novel data processing techniques for dispersive white light interferometer," *Optical Engineering*, vol. 42, pp. 3165-3171, 2003.
- [68] D. Grobncic, *et al.*, "Single and low order mode interrogation of a multimode sapphire fibre Bragg grating sensor with tapered fibres," *Measurement Science and Technology*, vol. 17, pp. 980-984, 2006.
- [69] M. Han, "Theoretical and Experimental Study of Low-Finesse Extrinsic Fabry-Perot Interferometric Fiber Optic Sensors," PhD, Electrical & Computer Engineering, Virginia Technic Institute and State University, Blacksburg, 2006.
- [70] K. J. Lesker. (2010, July, 22). *Material Deposition Table* [Online]. Available: http://www.lesker.com/newweb/menu_depositionmaterials.cfm?section=MDtable&init=skip
- [71] Y. S. Touloukian, *Thermal expansion--nonmetallic solids* vol. 13: New York : IFI/Plenum, 1977.
- [72] M. A. Clevinger, *Phase diagrams for ceramists. Bibliographic update through January 1, 1989 and cumulative indexes for volumes I-VIII* American Ceramic Society, 1990.

- [73] X. Chen, *et al.*, "Micro-air-gap based intrinsic Fabry-Perot interferometric fiber-optic sensor," *Appl. Opt.*, vol. 45, pp. 7760-7766, 2006.
- [74] K. A. Murphy, *et al.*, "Extrinsic Fabry-Perot Optical Fiber Sensor," in *Optical Fiber Sensors*, 1992, p. P30.
- [75] R. E. Wagner and C. R. Sandahl, "Interference effects in optical fiber connections," *Appl. Opt.*, vol. 21, pp. 1381-1385, 1982.
- [76] M. Han and A. Wang, "Exact Analysis of Low-Finesse Multimode Fiber Extrinsic Fabry-Perot Interferometers," *Appl. Opt.*, vol. 43, pp. 4659-4666, 2004.
- [77] J. Wang, *et al.*, "Multiplexed high temperature sensing with sapphire fiber air gap-based extrinsic Fabry-Perot interferometers," *Opt. Lett.*, vol. 35, pp. 619-621, 2010.
- [78] F. P. Kapron, *et al.*, "Aspects of Optical Frequency-Domain Reflectometry," presented at the Technical Digest, Third International Conference on Integrated Optics and Optical Fiber Communication, Washington DC, 1981.
- [79] T.-J. Ahn, *et al.*, "Chromatic Dispersion Measurement for a Few-Mode Fiber Using Optical Frequency-Domain Reflectometer," in *Conference on Lasers and Electro-Optics/Quantum Electronics and Laser Science and Photonic Applications Systems Technologies*, 2006, p. JTuD69.
- [80] T.-J. Ahn and D. Kim, "High-resolution differential mode delay measurement for a multimode optical fiber using a modified optical frequency domain reflectometer," *Opt. Express*, vol. 13, pp. 8256-8262, 2005.
- [81] M. Yoshida, *et al.*, "Novel PMD measurement method based on OFDR using a frequency-shifted feedback fiber laser," *Opt. Express*, vol. 9, pp. 207-211, 2001.
- [82] X. Fan, *et al.*, "Full polarimetric phase-noise-compensated optical-frequency-domain reflectometry for distributed measurement of high-PMD fibers," *Opt. Lett.*, vol. 35, pp. 25-27, 2010.
- [83] B. J. Soller, *et al.*, "High resolution optical frequency domain reflectometry for characterization of components and assemblies," *Opt. Express*, vol. 13, pp. 666-674, 2005.
- [84] N. Zou, *et al.*, "Fault Location for Branched Optical Fiber Networks Based on OFDR Technique Using FSF Laser as Light Source," in *National Fiber Optic Engineers Conference*, 2007, p. NWC2.
- [85] S. Moon and D. Y. Kim, "Normalization detection scheme for high-speed optical frequency-domain imaging and reflectometry," *Opt. Express*, vol. 15, pp. 15129-15146, 2007.
- [86] S. Kreger, *et al.*, "Distributed strain and temperature sensing in plastic optical fiber using Rayleigh scatter," *Proceedings of SPIE*, Jan 1 2009.